Doping Induced Effects on Tungsten Based Oxides Nanostructures and Their Characteristics

PhD Thesis

By

Faisal Mehmood
(20-FBAS/PHDPHY/S13)

Supervised by:

Dr. Javed Iqbal Saggu

Department of Physics,

Quaid-i-Azam University, Islamabad, Pakistan

Department of Physics
Faculty of Basic and Applied Sciences
International Islamic University, Islamabad
(2019)

Certificate

This is to certify that the work contained in this thesis entitled: **"Doping Induced Effects on Tungsten Based Oxides Nanostructures and Their Characteristics"** has been carried out by **Mr. Faisal Mehmood** in Laboratory of Nanoscience and Technology (LNT) under my supervision. In my opinion, this is fully adequate in scope and quality for the thesis of **PhD** Physics.

Supervisor
Dr. Javed Iqbal Saggu
Associate Professor
Department of Physics
Quaid-i-Azam University,
Islamabad, Pakistan

Doping Induced Effects on Tungsten Based Oxides Nanostructures and Their Characteristics

PhD Thesis

By

Faisal Mehmood
(20-FBAS/PHDPHY/S13)

A thesis submitted to

Department of Physics, International Islamic University,

Islamabad

For the award of the degree of

PhD Physics

Signature: _____

(Chairman, Department of Physics, IIUI)

Signature: _____

(Dean, FBAS, IIUI)

International Islamic University, Islamabad

Faculty of Basic and Applied Sciences

Department of Physics

Dated: 27th December, 2019

Final Approval

This is to certify that the work in this dissertation entitled **"Doping induced effects on tungsten based oxides nanostructures and their characteristics"** has been carried out by **Mr**. **Faisal Mehmood,** Registration No**. 20-FBAS/PHDPHY/S13** and completed in Laboratory of Nanoscience and Technology, Department of Physics, Faculty of Basic and Applied Sciences, International Islamic University, Islamabad is of sufficient standard in scope and quality for the award of degree of **PhD Physics**.

Committee

External Examiner 1

Dr. Zafar Iqbal, Professor / HOD, ----------
Department of Physics,
Riphah International University,
I-14, Islamabad.

External Examiner 2

Dr. Muhammad Atif, ----------
Associate Professor / Chair,
Department of Physics,
Air University, Islamabad

Internal Examiner

Dr. Kashif Nadeem, Associate Professor, ----------
Department of Physics,
International Islamic University,
Islamabad

Supervisor

Dr. Javed Iqbal Saggu, Associate Professor, ----------
Department of Physics, Quaid-i-Azam University,
Islamabad

This work is submitted as a dissertation in partial fulfillment of the requirement for the

degree of

***PhD** in PHYSICS*

at

Department of Physics

International Islamic University, Islamabad.

Declaration

It is declared that I have completed this thesis entirely on the basis of my personal effort, made under the sincere guidance of my supervisor. If any part of this report is proven to be copied or found to be a reproduction of some other, I shall stand by the consequences. The chapters 4, 5, 6, 7, 8 and 9 are based on my own publications in SCI journals as listed. No portion of the work presented in this report has been submitted in support of an application for other degree or qualification of this or any other university or institute of learning. The plagiarism test is carried out via **ID: 1240355609** using Turnitin software recommended by HEC, Pakistan and similarity index is in permissible range.

Faisal Mehmood

(20-FBAS/PHDPHY/S13)

Dedicated to

My Parents, Wife and Children Hassan, Ahsan and Zunaira

Acknowledgment

All praise to ALLAH, the most beneficent and merciful, who gave me strength to achieve what I wanted to be and blessed me all the ways. I would like to express my sincere gratitude to my research supervisor Dr. Javed Iqbal Saggu for their continuous support, outstanding scientific guidance and tremendous cooperation. I would also like to thank Chairman Department of Physics and Dean Faculty of Basic and Applied Sciences, IIUI for their cooperation during my research work.

I am thankful to Dr. Muhammad Ismail and Mr. Qaisar Mansoor, Institute of Biomedical and Genetic Engineering Islamabad (IBGEI), for providing me the opportunity to do part of biological experimental work in their laboratory. My special thanks also go to my all friends especially, Dr. Waqqar Ahmad (COMSATS) for supporting me whenever I need them.

At last but not the least, I owe my deepest gratitude to my wife, children, and whole family including my parents, sisters and brothers for their encouragement and prayers which enabled me to complete this project.

Faisal Mehmood

List of Publications

This thesis is based on the following publications:

1: F. Mehmood, J. Iqbal, T. Jan, W. Ahmed, W. Ahmed, A. Arshad, Q. Mansoor, S. Z. Ilyas, M. Ismail, I. Ahmad **"*Effect of Sn doping on the structural, optical, electrical and anticancer properties of WO_3 nanoplates*"** Ceramics International 42 **(2016)** 14334 -14341. **(I.F 2.95)**

2: F. Mehmood, J. Iqbal, A. Gul, W. Ahmed, M. Ismail **"*Facile synthesis of 2-D Cu doped WO_3 nanoplates with structural, optical and differential anticancer characteristics*"** Physica E 88 **(2017)** 188–193. **(I.F 2.20)**

3: F. Mehmood, J. Iqbal, T. Jan, Q. Mansoor **"*Structural, Raman and photoluminescence properties of Fe doped WO_3 nanoplates with anticancer and visible light driven photocatalytic activities"*** Journal of Alloys and Compounds 728 **(2017)** 1329-1337. **(I.F= 3.13)**

4: F. Mehmood, J. Iqbal, T. Jan, A. Gul, Q. Mansoor, R. Faryal **"*Structural, photoluminescence, electrical, anticancer and visible light driven photocatalytic characteristics of Co doped WO_3 nanoplates*"** Vibrational Spectroscopy 93 **(2017)** 78–89. **(I.F 1.92)**

5: F. Mehmood, J. Iqbal, M. Ismail, Arshad Mehmood **"*Ni doped WO_3 nanoplates: An excellent photocatalyst and novel nanomaterial for enhanced anticancer activities"*** Journal of Alloys and Compounds 746 **(2018)** 729-738. **(I.F 3.1)**

Other Publication

6: A. Arshad, J. Iqbal, M. Siddiq, Q. Mansoor, M. Ismail, **F. Mehmood**, M. Ajmal, and Z. Abid **"*Graphene nanoplatelets induced tailoring in photocatalytic activity and antibacterial characteristics of MgO/graphene nanoplatelets nanocomposites*"** Journal of Applies Physics 121 **(2017)** 024901. **(I.F 2.1)**

Abstract

The tungsten oxide (WO_3) nanostructures possess particular importance due to their significant physical, chemical and biological characteristics which allow them to be used in many highly efficient applications like photocatalysis, electrochromic, nanomedicine, sensing and electronic devices. This thesis focuses on the synthesis, characterizations and specific applications of undoped and metal (Fe, Cu, Sn, Co and Ni) doped tungsten oxide nanostructures. The thesis highlights the development of novel synthesis technique which is rapid, consumes less energy and time, is more economical and is easily reproducible. The synthesized nanomaterials were thoroughly characterized using various structural, electrical and optical characterization techniques. The other aspect of the thesis is to use the synthesized nanomaterials for several important novel applications such as visible light driven photocatalysis and anticancer activities. The thesis is divided into several chapters, the detail of which is given below.

Chapter 1 gives a brief introduction of the metal based oxide semiconductors. In addition to this, a short review on the targeted applications, such as photocatalytic and anticancer properties with detailed mechanism is presented. Finally, the chapter describes the objectives, importance and problem statement of the thesis.

Chapter 2 presents the review of physical and biological properties of WO_3 such as crystal structure, morphology, vibrational bands, compositions, band gap, photoluminescence, dielectric, photocatalytic and anticancerous properties.

Chapter 3 includes the synthesis details of undoped and metal (Fe, Cu, Sn, Co and Ni) doped WO_3 nanostructure, visible light driven photocatalytic and anticancerous (cytotoxicity) procedures and the characterization techniques which have been used in this thesis are discussed.

Chapter 4 describes the synthesis, characterizations, photocatalytic and anticancer activity of Fe doped WO_3 nanostructures. Herein, a series of Fe doped WO_3 nanoplates have been synthesized using a facile co-precipitation method. The XRD, SEM, EDX, XPS, FTIR, Raman, LCR, DRS and PL spectroscopy have been used to investigate the Fe doped WO_3 nanoplates. This study provides a facile and effective method to prepared Fe doped WO_3 nanoplates with enhanced (up to 94 %) visible light driven photocatalytic degradation of methyl red. Most importantly, this is one of the initial reports that Fe doped WO_3 nanoplates are an excellent candidate for anticancer applications. The Fe doped WO_3 nanoplates have shown highly efficient anticancer activities against human liver (Hep-2) and breast (MCF-7) cancer cells. The percent cell viability of both cancer cells lines is significantly decreased (up to 50%) with Fe doping.

Chapter 5 presents the synthesis of Sn doped WO_3 nanoplates. Various characterization tools have been employed to study the effect of Sn doping on the structural, optical and dielectric properties of WO_3 nanoplates. The visible light driven photodegradation activity of WO_3 nanoplates is enhanced up to 83%. Furthermore, the anticancer activity of WO_3 nanoplates against MCF-7 cancer cells is also increased with Sn doping which is attributed to several factors such as particle size, defects density and reactive oxygen species (ROS) production.

Chapter 6 describes the effect of Cu doping on structural, optical and biocompatible anticancer properties of WO_3 nanoplates. The photocatalytic activity is increased up to 80% with Cu doping. Moreover, the differential (biocompatible) anticancer activities of Cu doped WO_3 nanoplates against MCF-7 cancer cells and liver (Hep-2) cancer cells are also observed.

In chapter 7, the substitution of Co^{2+} ions on the sites of W^{6+} ions has been confirmed through X-ray photoelectron spectroscopy (XPS) analysis. The Co doping has been found to be very effective in enhancing the visible light driven photodegradation activity of WO_3 nanoplates

up to 90% which is attributed to trapping of photogenerated electrons by defects. Furthermore, Co doped WO_3 nanoplates have also shown good anticancer activities against human breast (MSF-7) and lever (Hep-2) cancer cells.

In chapter 8, the effects of Ni doping on the structural, optical, photocatalytic and anticancer activities of WO_3 nanoplates were studied. The mineralization degree of organic dye using Ni doped WO_3 photocatalyst was determined by total organic carbon analysis (TOC), reaching percentages of mineralization up to 96 % of methyl red in just 2 hour under illumination of visible light. Interestingly, it was also observed that the percent cells viability of human breast (MCF-7) and liver (Hep-2) cancers cells were decreased remarkably up to 30% and 35% respectively with Ni ions doping.

Table of Contents

List of Figures

List of Tables

CHAPTER 1

INTRODUCTION

1.1 Introduction

Nanotechnology is an emerging field, which contributes enormously in various modern day technologies. Nanotechnology plays vital role to replace the existing technologies with the new innovative methods and technologies to achieve high performance products that consume less energy and have small destruction effect to the environment. The physical, chemical and biological characteristics of materials change significantly at nanoscale. In future, the society and economy is likely to get more benefits using nanotechnology. The rapid advancement in nanotechnology assures breakthroughs in various areas like material fabrications, agriculture, biotechnology, health care, environment, nano-electronics, energy, information technology and defense related industries [1].

Nanotechnology based applications provide variety of solutions to the prevailing environmental issues and also offer precautionary measure to environmental hazards. The people associated with environmental regulations authorities and common public have shown biggest apprehensions regarding large scale use of dyes, herbicides, pesticides and solvents in agriculture, textile and paper printing industries. These organic pollutants harmfully influence the environment and are a key source of aesthetic pollution, eutrophication and ecological disturbance in water life owing to their toxicity. Therefore it is essential to detoxify these harmful organic pollutants to safeguard our environment. Previously, various wastewater treatment techniques have been proposed. However, photocatalytic oxidation procedure is

considered as one of the best facile option for the photodegradation of several toxic textile industries dyes and hazardous pollutants using nanomaterials [2-4].

Figure 1.1 Toxic dyes containing textile industries untreated water

Cancer is another serious health care problem which affects the human life on large scale around the world. Cancer is happens when the normal cell proliferation controls are vanished and it is considered as a complex and heterogeneous disease. Nanotechnology also symbolizes an innovative platform that assures to offer a wide variety of novel technologies for biological and biomedical applications. It has been interestingly observed that the size of naturally occurring proteins and biomolecules in the cells are comparable to the size of ultra small nanostructures.

For example in human, the cells have typical diameter of about ~ 7 μm [5]. At nanoscale, frequent changes in material's structural, morphological, magnetic, electrical and chemical properties are achieved which encourage their cooperation within cell biomolecules in extraordinary ways and furthermore empower the penetration activities within the cells structures. In general, the high surface reactivity generated at nanoscale is due to the presence of larger proportion of atoms at the materials surface [6]. This can enhance their capability to be attached with therapeutic agents and their transport to the target cells. These nanomaterials have capabilities to penetrate through physiological barriers and infiltrate intensely into selective types of target cells with appropriate engineering design.

There are several therapy techniques like chemotherapy, radio treatment, and immune treatment that have been used for this tumor treatment, yet the result rates stay immaterial because of the drug resistance or their inability to separate viably amongst harmful and typical cells [7, 8]. Along these lines, there is a pressing need to grow new class of nanomaterials as anticancer agent through novel methods which target selectively the disease cells while saving healthy cells with less toxicity [9, 10]. Presently, the metal oxide semiconductors are the most examined nanomaterials that have a potential as a anticancer agents and as photocatalyst [11, 12].

1.2 Metal oxide semiconductors

In recent times, the researchers paid attention towards the use of metal oxide (MO) based semiconductor nanomaterials. These can be prepared with minimal effort and low cost to meet the broad demand of various industries [13]. They include transition metals like TiO_2, WO_3, ZnO, SnO_2 etc and are highly investigated for their use in diverse applications [14]. Different electrical properties can be obtained using oxide compounds. Oxidic compounds are formed by

making chemical bond between metal elements and oxygen. The electrical behavior of metal oxide relies upon the accessibility of oxygen atoms that are attached to the metals. The significant decrease in metal oxide particle size is observed with the nanostructuring and it bring new characteristics like structural, physicochemical, electronic and magnetic properties to them, which are different as compared to their bulk counterparts [15].

In transition metal oxides, the defects have played a vital role to change the characteristics of these compounds. Therefore, metal oxides semiconductors have becomes more prominent material because of their ability to induce free electron hole pairs under irradiation of light and are therefore utilized for removal of toxic organic pollutants, nanoelectronics and biomedical applications. Metal oxide nanostructures are considered as inevitable materials to treat the ecological problems in environment. These vital catalytic properties of metal oxide nanostructures are due their large active surface area, stability, high surface energy and quantum confinement effects. The metal oxide based photocatalysts have shown higher decoloring efficiency against organic pollutants photodegradation. This feature takes vital part in purification of wastewater effluent for biological applications. Researchers also have revealed that less concentration of metal oxide nanostructures can destroy tumor cells effectively whereas their bigger micrometer sized materials are relatively less harmful [9, 15-20]. Recently, cancer cells have been killed efficiently with metal oxide nanoparticles and less damage have been observed against healthy cells in vitro observations [9, 10]. The Metal oxide nanostructures higher chemical reactivity, large surface energy, enormous photoinduced free charge carriers with high charge carries separation rates and rapid charge transport abilities make them a potential source as a photocatalyst and as an anticancerous agent [21].

1.3 Photocatalytic properties

The photocatalysis process has observed a massive change over the years due to rapid innovation in the field of nanoscience and technology. Now a days, the photocatalysis has becomes an effective techniques due to efficient designing parameters with less energy consumptions for degradation of pollutants. Photocatalysis means, the increase rate of chemical reactions like oxidation and reduction due to the catalyst existence like metal oxide semiconductors in the presence of visible or ultraviolet irradiations [22].

1.3.1 Photocatalyst mechanism

The basic mechanism of photocatalysis during creation of oxidative species has been shown in Figure 1.2. Reactive oxygen species (ROS) were formed during a photocatalytic process and ROS were played extremely vital role in photodegradation activities. When nanostructures (photocatalyst) were permitted to expose under visible light irradiations then it causes free electron hole pairs (free charge carriers) generations. As a consequence, the massive ROS like superoxide ions ($O_2^{-\bullet}$) or hydroxyl radicals ($^{\bullet}OH$) were produced. The organic harmful waste materials can easily oxidize through ROS. The ROS generation occurs when photo induced free charge carriers interact with oxygen and water molecules. The hydroxyl radicals ($^{\bullet}OH$) attack the toxic dyes and after various reactions these toxic dyes are converted into intermediates and finally obtain CO_2 and H_2O [23, 24]. The control over ROS generation is very crucial part in heterogeneous photocatalysis to achieve an optimum level of degradation of organic pollutants.

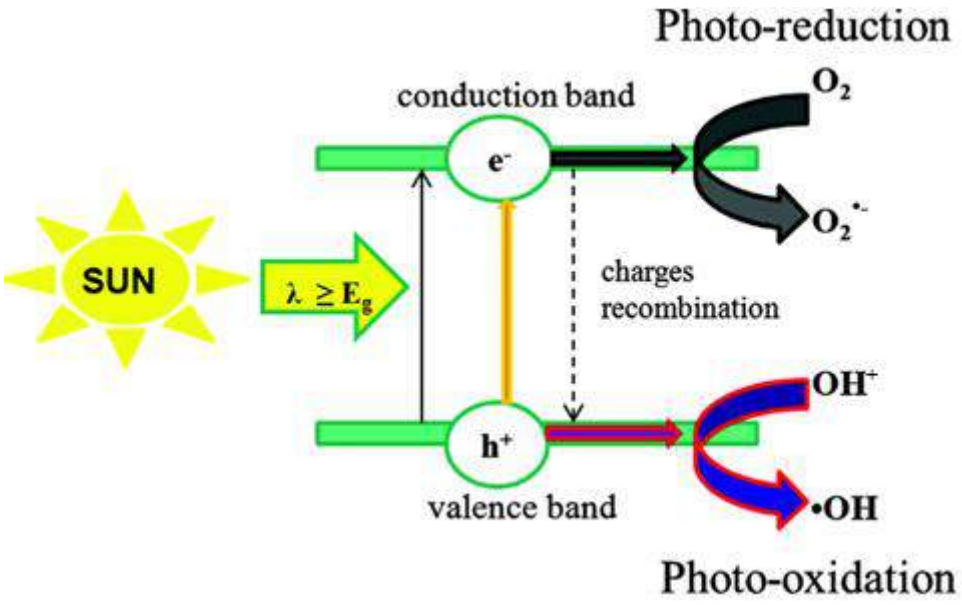

Figure 1.2 Photoactivation reactions at the surface of photocatalyst [25]

1.4 Biological (anticancer) properties

Cancer has become second driving reason for death in the world [15]. Recently, the World Health Organization has anticipated in their report that the overall cancer cases will may turn out to be more than twofold by the year 2030 [26]. In Europe, 421,000 instances of breast tumors (MCF-7) have been appeared just in 2008 and 184,450 new MCF-7 tumor cases have been examined between years 2008-2011 [27, 28]. The liver cancer (HepG2) cells have also been nominated as the major health issue worldwide [6, 29]. Nanotechnology has the ability to propose more effective and well focused techniques which give proficient treatment and cure to cancer patients. Various research groups have shown the ability of metal oxide nanoparticles to kill human cancer cells with low concentrations, whereas their larger micrometer sized counterparts are comparatively non-toxic [15-20]. The current reports depicted that the specific sorts of metal oxide nanoparticles can particularly destroy the tumor cells, with strikingly less harmfulness against healthy cells [9, 10]. For example, tumor cells have been killed using TiO_2

nanoparticles with UV irradiations [30-32]. The cancer cells (HeLa) growth restricted up to 30 days using TiO_2 nanoparticles under UV light whereas no disease cells killing was seen without TiO_2 nanoparticles.

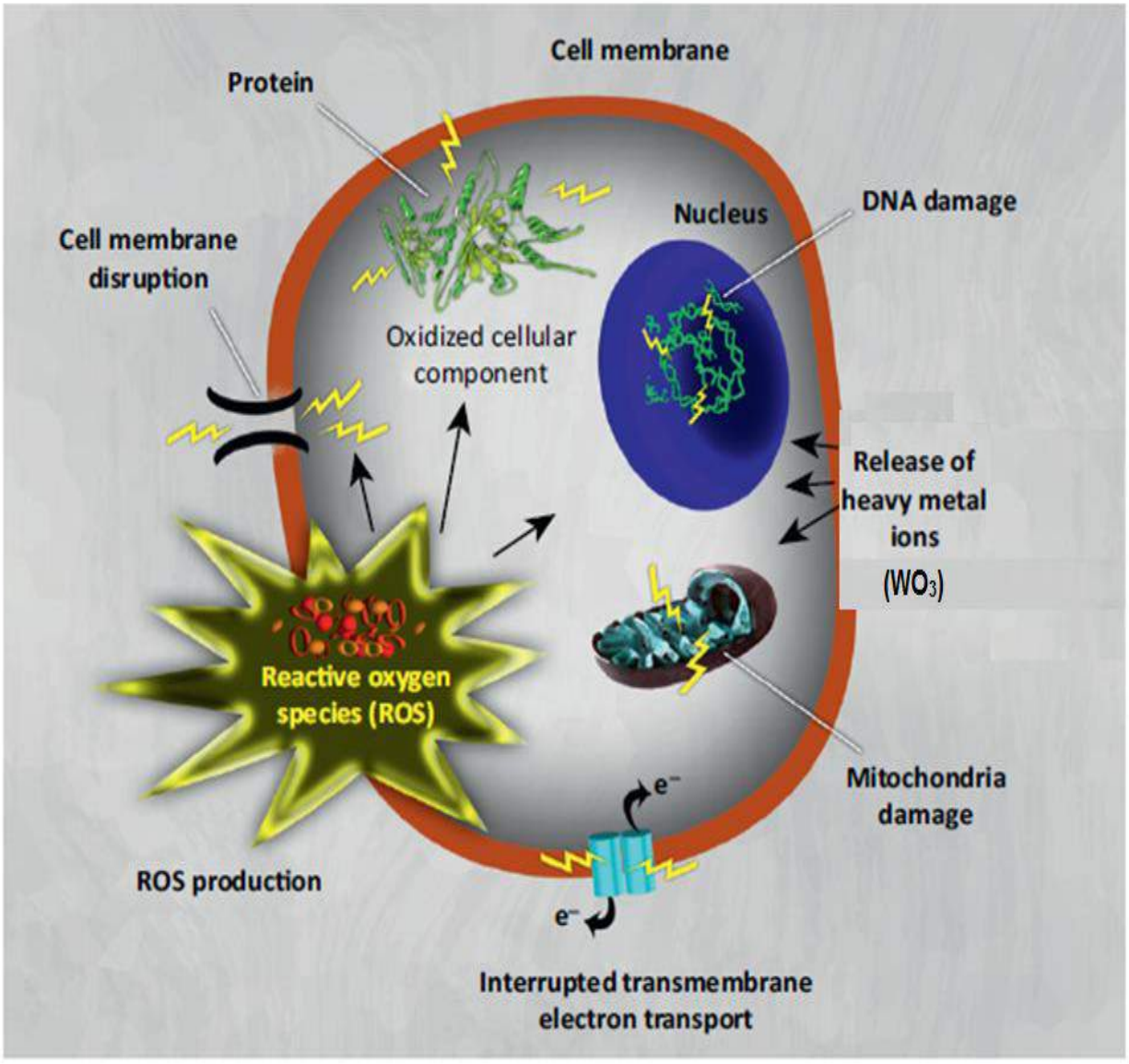

Figure 1.3 Toxicity mechanisms using metal oxide nanostructures.

In spite of several research techniques, cancer based diseases are still persist as a severe health care problem. Presently, acceptable nano-scale anticancer materials for liver (Hep-2) and breast

(MCF-7) cancer cells, which are considered to be the most common and dangerous types of cancers in human, are yet to be explored. Therefore, it opens up more demands for the development of new nanoscale biomaterials to tackle this disease effectively. The exact mechanism of metal oxides nanostructures towards various cancer cells lines is still debatable. However, the mechanisms of nanoparticles interaction with cancer cells have been reported. According to these reports the cytotoxicity of cancer cells using metal oxide nanomaterials have been linked to various factors like electrostatic interactions, oxidative stress, nanoparticle accumulation inside cells. Previous reports described that the electrostatic interactions may lead to the attachment of the ZnO nanoparticles with the outer cell membrane of the cells [28, 33-38]. The mechanism of cancer cells destruction using metal oxides is depicted in Figure 1.3. These nanoparticles may penetrate into the membrane of cancer cell and cause cytotoxicity [28]. Furthermore, the production of excessive ROS on the surfaces of nanoplates can also become a cause death of cancer cells by number of actions like apoptosis, damaging of cell membranes and lipid peroxidation [39-43].

1.5 Statement of problem

It is possible to tailor and have desired properties of tungsten oxide (WO_3) nanostructures through doping of different elements. The doping efficiency in WO_3 nanostructures is much higher than its bulk structure because of the increased surface area. In this proposed work, the goal is to achieve precise control over morphology and particle size of WO_3 nanostructures to meet the fast growing demands of applications in different fields. For this purpose, a simple and cost effective chemical wet route will be optimized to synthesize WO_3 nanostructures with the introduction of dopants into the host lattice matrix of WO_3. The physical properties of WO_3

nanostructures will also be significantly tuned with the substitution of different impurities to explore it for various potential applications.

1.6 Aims and objectives of the thesis

WO_3 has enormous applications in our daily life such as environmental, industrial and medical fields. It is interestingly observed that the WO_3 has shown exceptional physical and chemical properties at nanoscale. In this work, the doping of various impurities into the WO_3 nanostructures matrix will be carried out to alter the morphological, structural, dielectric, and optical properties. A cost effective, low temperature chemical route will be optimized to get the desire morphology (such as nanoplates) and uniform average size distribution of WO_3 nanostructures. Synthesis parameters (like reaction time, temperature, pH level, variation in reactants stoichiometry, etc) will be tuned to obtain ultrafine nanostructures. In order to modify the physical characteristics of WO_3, the different concentrations dopants elements (like Fe, Sn, Cu, Co and Ni) will be used to doped into WO_3 nanostructures. In order to check the required structural, morphological, vibrational, dielectric and optical characteristics of WO_3 nanostructures, the synthesized nanomaterials will be characterized through XRD, SEM, FTIR, Raman, XPS, PL, LCR meter and diffusion reflectance / UV visible spectroscopy, respectively. The prepared nanomaterials will then be tested for their performance in photocatalytic processes for dye removal processes and also for their anticancer properties.

CHAPTER 2

PHYSICAL AND BIOLOGICAL PROPERTIES OF WO_3

2.1 Introduction

In transition metal oxides, WO_3 having bandgap of about 2.4-3.2 eV is consider to be most promising n-type semiconductor with broad range novel functionalities. The WO_3 has an immense interest because of its exceptional, structural, electronic and optical characteristics. The synthesis of WO_3 in bulk form was first time carried out in 17^{th} century [44].

Now a days, the research interests in photocatalysis, electro-chromic, gas sensing and medical applications of WO_3 have flourished rapidly. At nanoscale, the optical, electronic, mechanical, electrical, charge transport and chemical properties of WO_3 have been found to improve significantly. Nanostructuring of any material has revealed promising potential due to their huge surface area to volume ratio, high surface energy, quantum confinement effect and other unique properties that owe to intrinsically small grains size of nanostructures.

2.2 Physical properties of WO_3

WO_3 is a chemical compound which contains a transition metal tungsten and oxygen. The basic characteristics of WO_3 are described in the Table 2.1.

Table 2.1 Basic characteristics of WO_3

Chemical formula	WO_3
Molar mass	231.84 g/mol
Appearance	Canary yellow powder
Density	7.16 g/cm^3
Melting point	1,473 °C (2,683 °F; 1,746 K
Boiling point	1,700 °C (3,090 °F; 1,970 K)
Solubility in water	Insoluble
Solubility	Slightly soluble in HF
Crystal structure	Monoclinic
Coordination geometry	Octahedral (W^{VI}), Trigonal planar (O^{2-})
Main hazards	Irritant
Flash point	Non-flammable

2.2.1 Structural characteristics of WO_3

Figure 2.1 shows the polyhedral illustrations of these six structures [45]. The phase categorization depends on WO_6 octahedra rotation direction and the tilting angles.

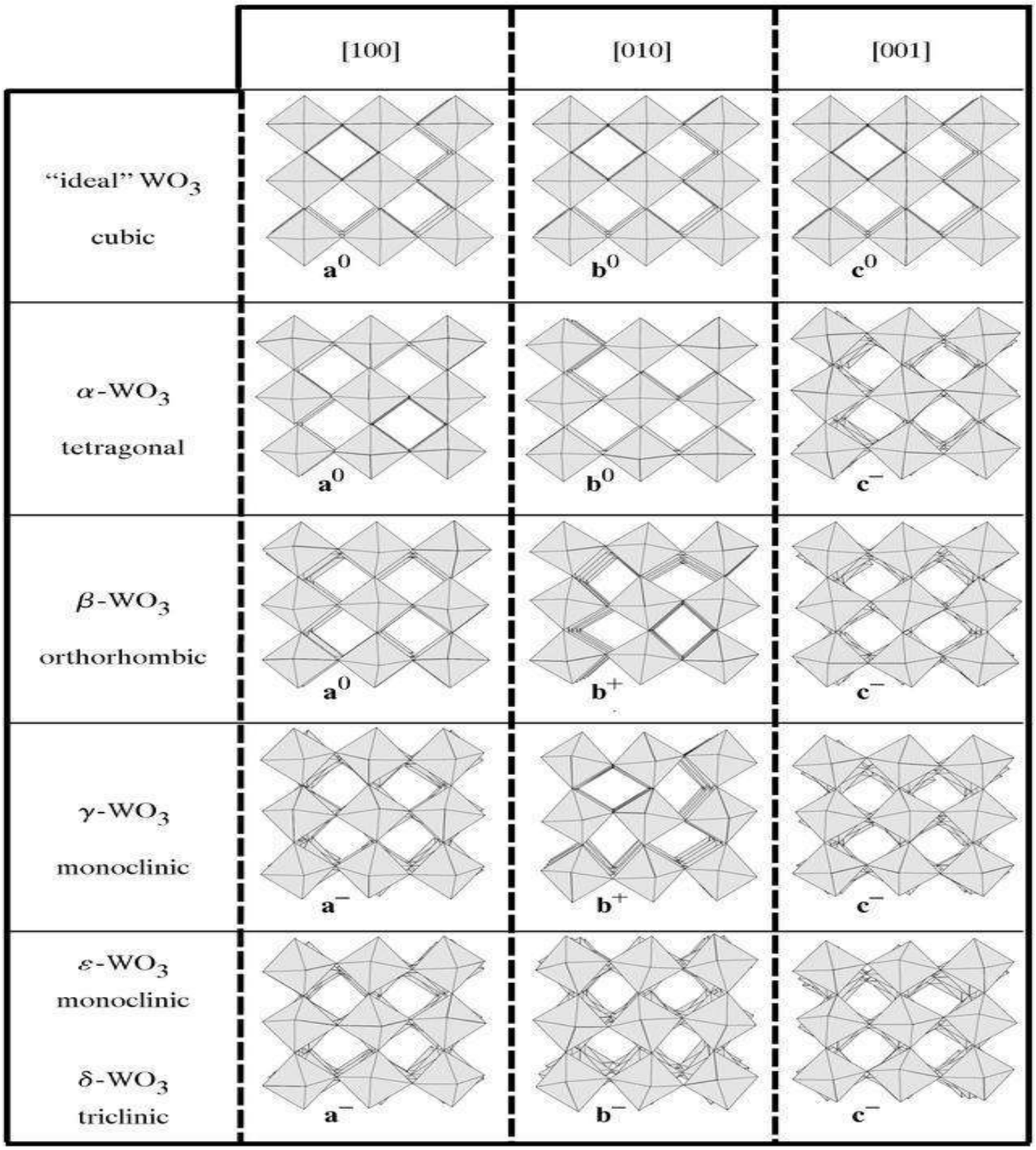

Figure 2.1 Various polymorphs of WO_3 [45]

Table 2.2 Lattice parameters of different crystal phases of WO_3 [46, 47].

lattice constant (Å)	ε-WO_3	δ-WO_3	γ-WO_3	β-WO_3	α-O_3
a	7.378	7.309	7.306	7.384	5.25
b	7.378	7.522	7.540	7.512	N/A
c	7.664	7.686	7.692	3.846	3.91

The phase transitions of WO_3 crystal can occur like other metal oxides through annealing and cooling. Several research reports show that phase transformation of WO_3. The monoclinic I (γ-WO_3) is most stable structure at room temperature. However in few reports stable phase triclinic (δ- WO_3) crystal structures have also been observed. The WO_3 transforms into other crystal phases at elevated temperature. But at room temperature it cannot maintain these alternate phases [48]. The nanostructuring causes the complex phase transition activities in WO_3 based materials due to variable dimensions and morphologies of the material. The Gibbs-Thomson expression told that the high surfaces energy is found with decrease in crystallite size of WO_3 nanomaterials which leads to decrease melting and sublimation temperature [49, 50]. The perovskite units are the basic building block of WO_3 and are eminent for its nonstoichiometric characteristics as shown in Figure 2.2. The WO_3 lattice endures a sizeable quantity of oxygen deficiency due to these nonstoichiometric characteristics [51]. The significant changes have been observed in its electronic band structure due to the occurrence of partial deficiency of oxygen content [52].

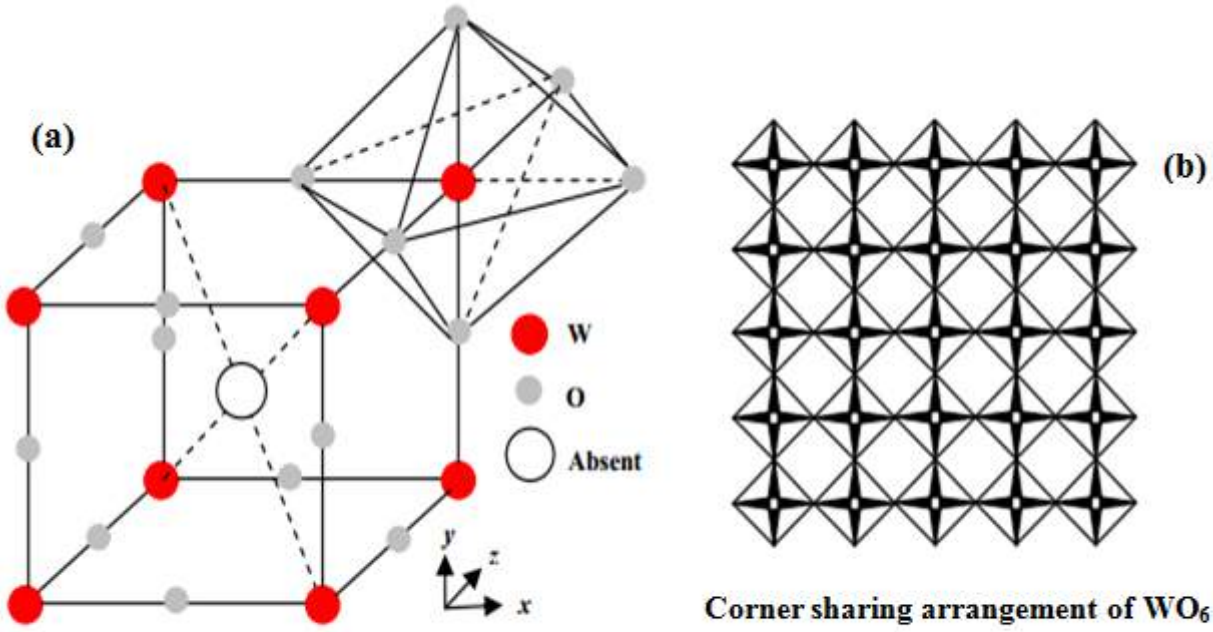

Figure 2.2 (a) Perovskite lattice unit cell (b) Layer of one monoclinic WO_3 structure.

2.2.2 Optical properties of WO_3

WO_3 is a broader bandgap semiconductor and therefore it is a potential material for many photonics and electrical applications [53, 54]. It is well known that the bandgap of WO_3 increases with reduction in its particle size. The Fermi function, *f* (E), has been well utilized to describe the energy bandgap phenomenon in metal oxides by giving the possibility of getting a free electron in a particular energy state. The formula is described as follows [53].

$$\mathbf{f(E)} = \frac{\mathbf{1}}{\frac{\mathbf{(E - E_F)}}{\mathbf{e^{kBT}+1}}} \qquad (2.1)$$

Where k_B is the Boltzmann's constant, T and E_F are the absolute temperature and Fermi energy respectively. The above relation explains that in the Fermi energy is found at the center of the

maximum occupied band. For different materials, i.e. conductors, insulators and semiconductors, the Fermi energy level is described in Figure 2.3.

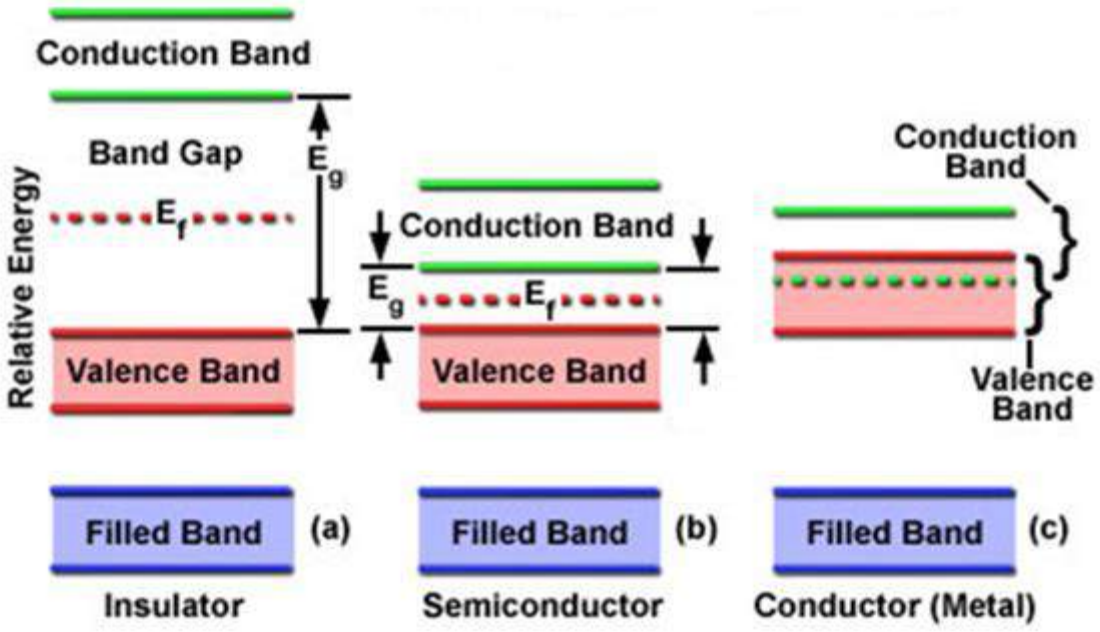

Figure 2.3 Fermi energy level and energy bandgap diagram of conductor, semiconductor and insulator

The rise in temperature provides sufficient energies to electrons and consequently electron jumps from valance band to conduction band. There is no barrier for free electron movement in conductors due to overlapping band structure. However in semiconductors, only few electrons can have the energy equal to their energy bandgap and for insulators, no electron has sufficient energy to overcome the respective energy bandgap. Bulk materials have different energy bandgap levels as compared to nanomaterials [55]. Following relation has been utilized to estimate the light absorption (α) [56].

$$\varepsilon \alpha \propto (\varepsilon - E_g)^{\eta} \qquad (2.2)$$

The η=2 is used for allowed indirect transitions in WO_3 and ε is photon energy. It is broadly recognized that normally blue shift founds in energy bandgap due to the quantum confinement effect (QCE) [57]. It can be split into two types, i.e. strong QCE and weak QCE. Strong QCE is observed when the crystal size is decreased up to 3 nm (Bohr radius) [58]. This effect may produce direct perturbation of the electron wave functions and as a consequence energy bandgap is altered significantly. Alternately, the weak quantum confinement effect occurs in WO_3 nanomaterials when crystal size is bigger than 3 nm [59].

2.2.3 Electrical properties of WO_3

In n-type metal oxide semiconductors, the conduction bands contain large number of free electrons which mainly contributes to electrical conductions. In these materials number of free electrons have direct link with the existence of stoichiometric defects [60]. The range of electrical conductivity of WO_3 is also depends on its stoichiometry [52]. Various parameters like grain size, film thickness, dopant presence have direct effects on the electrical conductivity of material [61]. Therefore, material preparing procedures and synthesis conditions have major role in WO_3 electrical properties. The relatively high electron mobility and carrier concentration (5×10^{19} cm^{-3}) have found for WO_3 films, fabricated at high temperature through thermal evaporation depositions and sputtering [62]. The available free electrons for conduction have been increased with high substrate temperature, which have a tendency to separate oxygen ions under vacuum conditions. The carrier mobility in two dimensional metal oxides crystal structures have been increased with the reduction of scattering effects due to smooth boundaries with confinement of the free charges motion inside well [63]. However, the resistivity in metal oxide has been increased with roughness of the structure. In previous reports, the conductivity of WO_3

has been decreased with its nanostructuring. The large number of grain boundary generations has decreased the conductivity of WO_3 nanomaterials. The larger scattering and trapping of electron hole pairs reduces the electrical conductivity [64]. The grain boundary scattering becomes more effective when crystallites size is smaller than the mean free path of electron. Additionally, some other factors also reduce the conductivity of nanomaterial like lattice strain and crystal distortions or defects which ultimately affect the motion of free charge carriers [65].

2.2.4 Vibrational properties of WO_3

The surface chemistry of synthesized nanomaterials is usually explored through FTIR spectroscopy. In WO_3 nanomaterials, the bands observed between 1400 cm^{-1} and 1700 cm^{-1} are belonged to bending modes of O-H groups and the broad band observed at 3300-3600 cm^{-1} is linked with the stretching modes of O–H groups in H_2O or hydroxyls. The broad band that appears at 550–1050 cm^{-1} is associated with the O–W–O stretching mode [66]. The presence of these WO_3 stretching mode represents the WO_3 monoclinic structure.

Furthermore, The Raman spectroscopy techniques is normally utilized to observe microstructural properties and the possibility of the presence of any secondary phases [67, 68].

2.3 WO_3 nanostructures as photocatalyst

Fujishima and Honda in 1972 discovered for water photolysis on a TiO_2 electrode and it was recognized as a landmark achievement [69]. This achievement opens up new research era on photonic energy conversion by photocatalytic technique. Since then, TiO_2 based photocatalysis has been focused on a large scale to obtain knowledge about fundamental principles and characteristics of photocatalysis [70-72]. TiO_2 has been utilized in many vital applications like

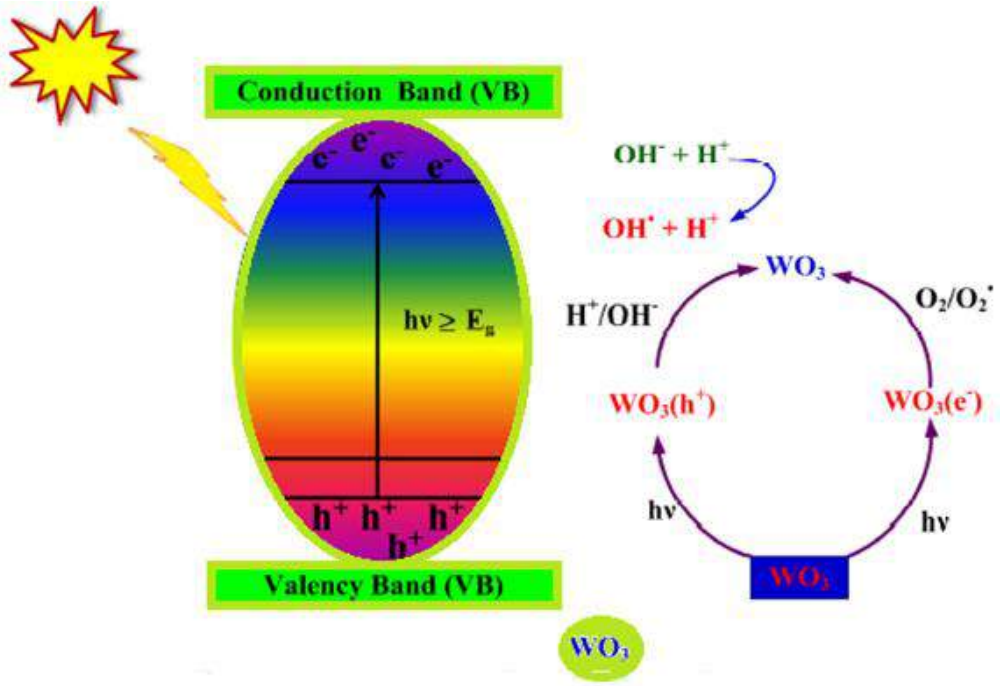

Figure 2.4 Photocatalysis mechanism schematic diagram [73-75].

wastewater treatment devices, generation of hydrogen fuel and solar cell. However, TiO_2 is not suitable for many purposes rather it has drawback with visible light based photocatalysis due to its bandgap. WO_3 as photocatalyst can be considered as an effective alternative to the TiO_2 and shown in Figure 2.4. WO_3 is a multipurpose nanomaterial due to its suitable band gap (2.4- 2.8 eV) and it could utilize large part of the visible solar spectrum. WO_3 possessed larger diffusion length (~150 nm) as compared to TiO_2 or Fe_2O_3 which decreases recombination of charge carriers. As a photocatalyst it attracted more interests due to the strong solar spectrum (≤ 500 nm) adsorption [73-75].

WO_3 also demonstrate less toxicity and excellent chemical stability in water. The photocatalytic ability of WO_3 nanomaterials have been increased efficiently. At nano scale, the surface area of the particles has been increased significantly and as a result enough sites are available for

photochemical reaction [76]. Besides, in bulk material the transport mechanism and separation of charge carriers have different behavior as compared to nanomaterials.

WO_3 is a very effective photo-oxidising agent and it has been used in treatment of textile dyes and removal of bacterial pollutants [77]. WO_3 also has another promising feature that it shows excellent stability in acidic environments. Therefore, it is the most suitable wastewater purification containing organic pollutants [76].

The rapid photoinduced electron-hole pair recombination rates are still a key trouble in photodegradation process. To solve this problem, suitable modification (like doping) process is always needed.

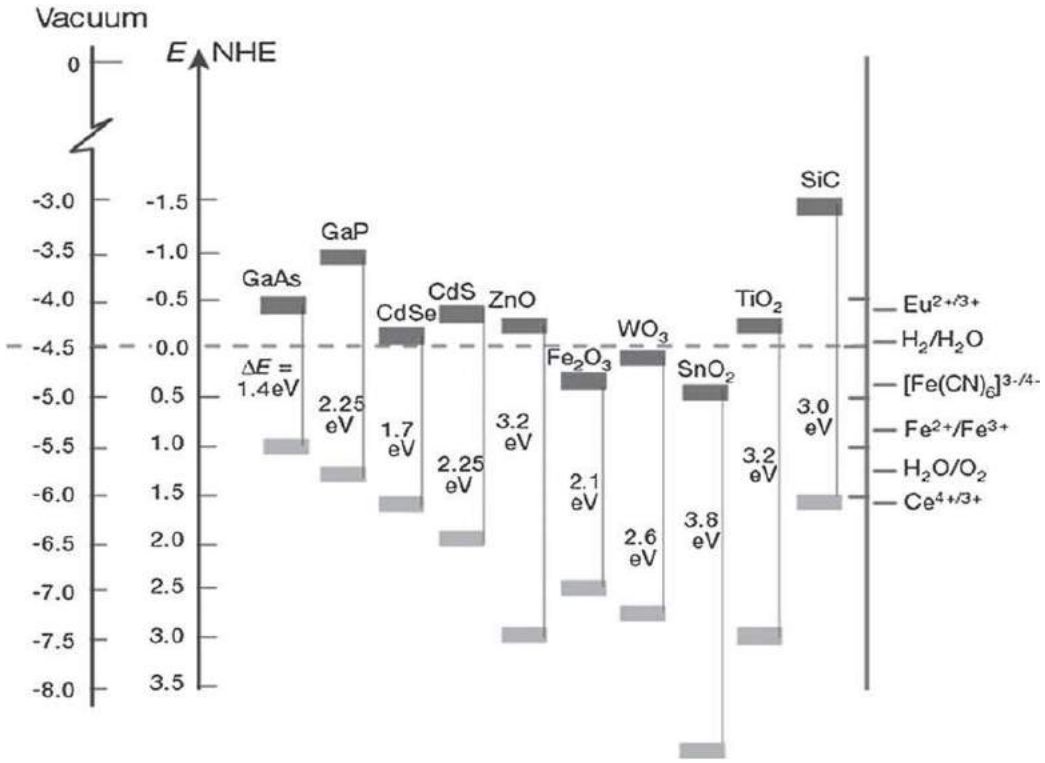

Figure 2.5 Various semiconductors conduction band and valence band energy levels [78].

Uresti et al. applied microwave assisted hydrothermal procedure for the synthesis of WO_3 nanoparticles without any additives. The obtained WO_3 nanoparticles were further calcined at various temperatures to achieve monoclinic and hexagonal WO_3 structures. The photodegradation activities of these nanoparticles under UV-vis light illumination were analyzed against tetracycline hydrochloride (TC) and others dyes. The increased photodegradation was attained at 700^oC. The degradation percentage observed after 96 hours of UV light irradiation was 65% for TC, 65% IC and 95% for RhB [79]. In another report, WO_3 having orthorhombic phase were fabricated using conventional and microwave assisted techniques. These WO_3 nanostructures efficiently degraded the methylene blue under UV irradiation for 5 hours [80]. Gondal et al. reported photocatalytic removal of hazardous dye from water under laser irradiation with monoclinic plate shaped WO_3 nanomaterials [81].

In another study, WO_3 with multi structures were fabricated in presence of metal salts such as $CaCl_2$ and Na_2SO_4 [82]. The photodegradation of methylene blue was achieved with nanomaterials based hierarchical network structures under simulated solar illuminations. These multi nanomaterials shapes were applied for photodegradation of methylene blue and it requires 8 hours to completely photodegrade the pollutants. Although WO_3 is a visible light absorber but individual (undoped WO_3) takes more time for removal of wastewater containments under illumination of light. The fast photodegradation rates can be achieved with the presence of metal ions dopants [83-85].

2.3.1 Doping induced effects on WO_3 photocatalyst

The photocatalytic activity of WO_3 nanomaterials can be further enhanced using different dopants. With the introduction of dopant into WO_3 nanomaterials enhances the free charge carriers, conduction band level and reduction potential is enhanced by generation of defects [86].

The doping of metals ions is quit helpful to acquire optimum properties of nanostructures as compared to bulk material. Furthermore, the dopant elements can be categorized into two types, one is cationic dopants and other is anionic dopants. Generally, the metal ions are substituted with cations dopants and oxygen ions are replaced with anion dopants. In heterogeneous photocatalysis technique, the free charge carriers have been generated on the surface of WO_3 under absorption of light. This is a vital feature of WO_3 for fast photodegradation of pollutants and organic dyes. However, because of its narrow energy band gap structure, the photo induced electron-hole pairs can also have a tendency to recombine easily before degradation of pollutants. The electrons holes pair recombination can be avoided through surface modification to improve photodegradation efficiency. The surface modification occurs through various techniques such as metal or non-metal ions doping.

Moreover, the photocatalytic performance of commonly utilized TiO_2 is slightly higher as compared to undoped WO_3. This is because TiO_2 has lower reduced reduction potential of conduction band. The higher photocatalytic performance of WO_3 can be achieved through metal ions doping due to variations in absorption. The shift in the absorption band depends upon the dopant oxidation state, ionic size and their concentration within the host matrix. The photodegradation activities of WO_3 have been enhanced previously via various metals ions doping such as V^{5+}, Ta^{5+}, Nb^{5+}, Ti^{4+} and Mo^{6+} due to large number of defects generations [87-92]. Augustynski et al. revealed that B-doped WO_3 lower the carrier recombination and enhanced photocatalytic activity about 70% under visible wavelengths at 420 nm [93, 94]. Kovendhan et al. established that the structural alteration from orthorhombic to tetragonal phase and blue-shift of photoemission has been occurred with 5% Li-doping into WO_3 material [95]. Cao et al reported that AgBr loaded WO_3 nanomaterial with addition of H_2O_2 resulted into

efficient trapping of electrons and improved photocatalytic efficiency against methyl orange in 3 hours [96].

2.4 WO_3 as anticancer agent

WO_3 can be considered as a effective anticancer agent due to holding significant photodynamic properties. In literature, only few rare reports are available on anticancer properties of WO_3. Hasan et al. have reported the biosafe anticancer activities using WO_3 nanoparticles against the rat liver cells [97]. Recently, Yassin et al. has also reported the biocompatible nature of WO_3 nanomaterials with enhanced anticancer activities against both cervix and colon cancer cells [98]. In addition to the above mentioned applications, upraising techniques by WO_3 nanomaterials are getting significance for the growth for novel anticancer therapeutics.

2.4.1 Doping induced effects on anticancer properties

There is substantial concern to enhance the anticancer characteristics of nanomaterials by functionalizing them through metallic ions dopants. Fazal et al. reported that Ni dopant can change the cytotoxic activities of metal oxide nanoparticles making them useful for anticancer cells applications [21]. L. Sadeghi et al. reported that the 80% cancer cell viability was found against $HepG_2$ cells using 20μg/ml solution of Fe_3O_4 nanoparticles [99]. K D. Wani et al reported that 86% anticancer activities was observed with 80μg/ml of functionalized Fe_2O_3 nanomaterials [100]. According to density function theory (DFT), the metal ions doping into WO_3 host matrix may generate phase segregation, diffusion of defects to the surfaces, interstitial impurities and optical band gap variation [101]. The formation and diffusion of defects to surface and band gap variations may be vital for cytotoxic activities of WO_3 nanostructures. As surface defects and optical properties of metal oxides nanostructures have been believed to be very important for

ROS production which is lethal for cancer cells. So far, in literature, no report on anticancer properties is available that is based on use of doped WO_3 nanostructures.

CHAPTER 3

SYNTHESIS AND CHARACTERIZATION TECHNIQUES

3.1 Nanoscience and nanotechnology

The new opportunities have been created rapidly in the field of nanoscience and nanotechnology to make human life better and secure. The nanostructuring of the material creates novel characteristics in the nanomaterials such as fast surface chemical reactivity and solubility which make them potential candidate especially for environmental pollutant remediation and for biomedicine. Nanotechnology has been focused to gain knowledge and understanding about them at nanoscale. These nanostructures interactions depend on their dose concentration levels and physiochemical properties such as size, shape, reactivity and material composition [102].

Nanomaterials possess structures with dimensions at the nanoscale. The physical, chemical and biological properties of WO_3 have been significantly changed in contrast to their bulk WO_3 counterparts. Here in this thesis, the chemical aqueous solution techniques have been utilized to optimize structure parameters during the fabrication of WO_3 nanostructures.

3.2 Synthesis techniques

The detail experimental procedural description is the main purpose of this chapter. Previously, different synthesis protocols have been devised to fabricate various WO_3 nanostructures like template base technique, solvothermal, exfoliation and chemical co-precipitation method [103, 104]. Among them, the chemical co-precipitation is the most facile and most effective method to prepare nanostructures with controlled size and morphology. There are two types of nanomaterials synthesis techniques like bottom-up and top-down**.**

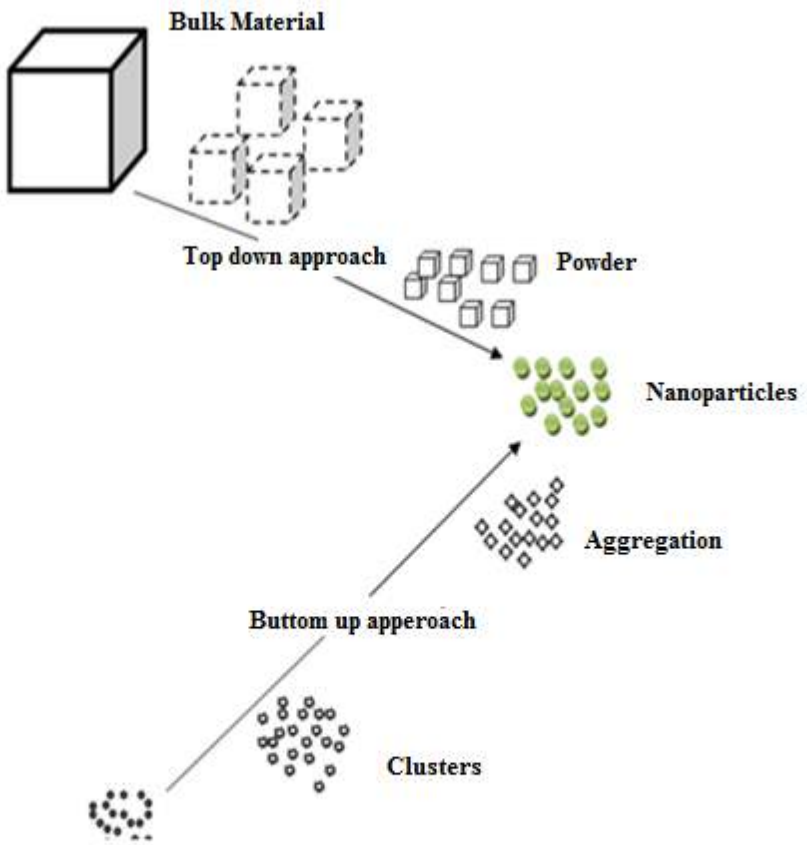

Figure 3.1 Schematic representation of the top down and bottom up approaches

Figure 3.1 illustrate both categories of fabrication procedures**.** The top-down approach is about successive slicing of a bulk sized materials up to nano-sized materials. In top down technique, diverse preparation methods such as erosion, etching, molding, ball milling, printing and lithography, have been used to fabricate nanostructured materials.

The other technique is also represented in Figure 3.1 in which the nanomaterials are formed by combing atoms that are converted into tiny clusters to obtain the desired shape of nanostructures. Various techniques are usually adopted to control the size, morphology. Various types of bottom-up techniques have been shown in Figure 3.2.

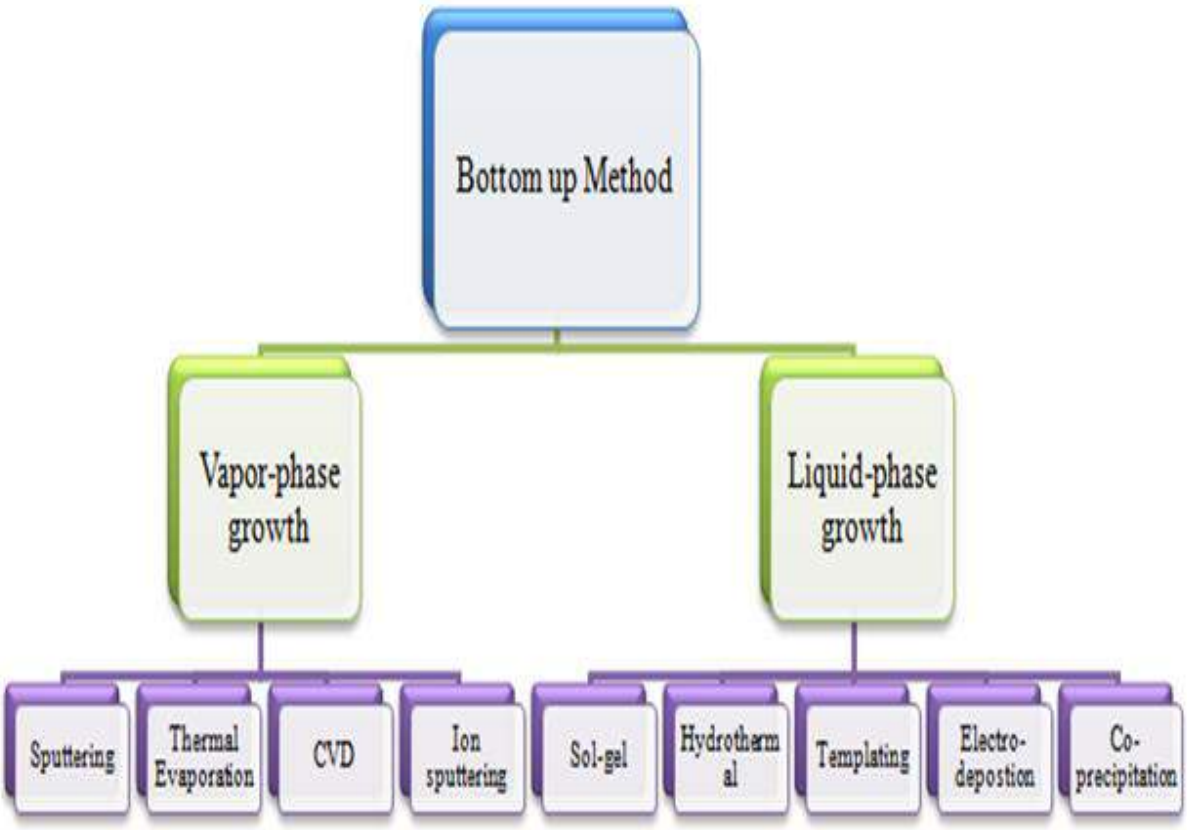

Figure 3.2: Bottom up approaches

The top-down approach has a slight disadvantage in controlling the morphology and uniform particle size due to limited control over particles size and morphology. Moreover, the top-down approach also has a big problem due to generation of imperfections in surface structure with significant damage of crystallographic patterns during nanostructures fabrication process.

3.3 Chemical co-precipitation technique

Co-precipitation process is a solution based chemical route in which the process of precipitation of metal ions takes place. The undoped and metal doped WO_3 nanostructures were prepared through this route. The analytical grade chemicals were used and then utilized for preparation of nanostructures. Co-precipitation has a benefit on all other bottom up methods because it is low cost, simple to deal with, and smooth morphology. Precipitation of material takes place when solution is supersaturated as a result of very high concentration of material in the solution. This unstable solution generates large clusters due to enhanced nucleation. The precise optimization of reaction parameters is quite helpful to get the mono-dispersed desired morphology and crystallinity of nanostructures. This could be attained by tuning the reaction parameters like reactants molarities, pH value of the reaction, reaction time, reaction temperature, stirring rate, adding capping agent or surfactants with different solvents. The more stable nanoparticles are obtained during slow growth mode through Ostwald ripening process. A suitable capping agent is used to control the size distribution, growth and limit the agglomeration Furthermore, the optimization of these parameters in chemical co-precipitation method provides precisely control over the stoichiometric ratio of the WO_3 nanostructures. The high crystallinity of synthesized nanomaterials was gained through annealing the samples at 300^oC. A schematic diagram chemical co-precipitation method is described in Figure 3.3.

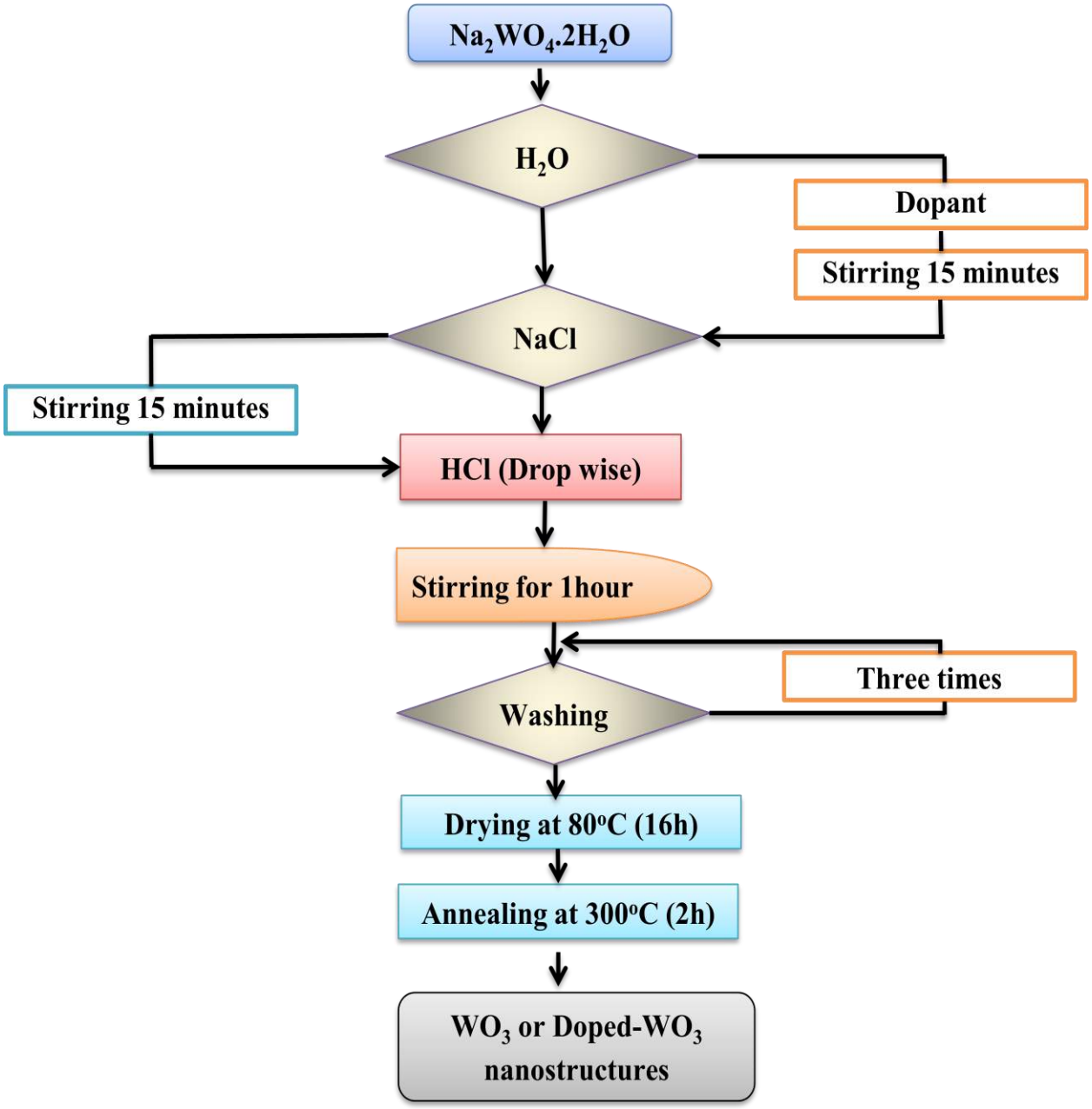

Figure 3.3 Synthesis of WO_3 nanostructures through the co-precipitation technique

3.4 Growth investigations

The solution based synthesis process of WO_3 nanostructures has been well understood [105-107].

In our case, H_2WO_4 was first formed upon the addition of HCl in Na_2WO_4 solution.

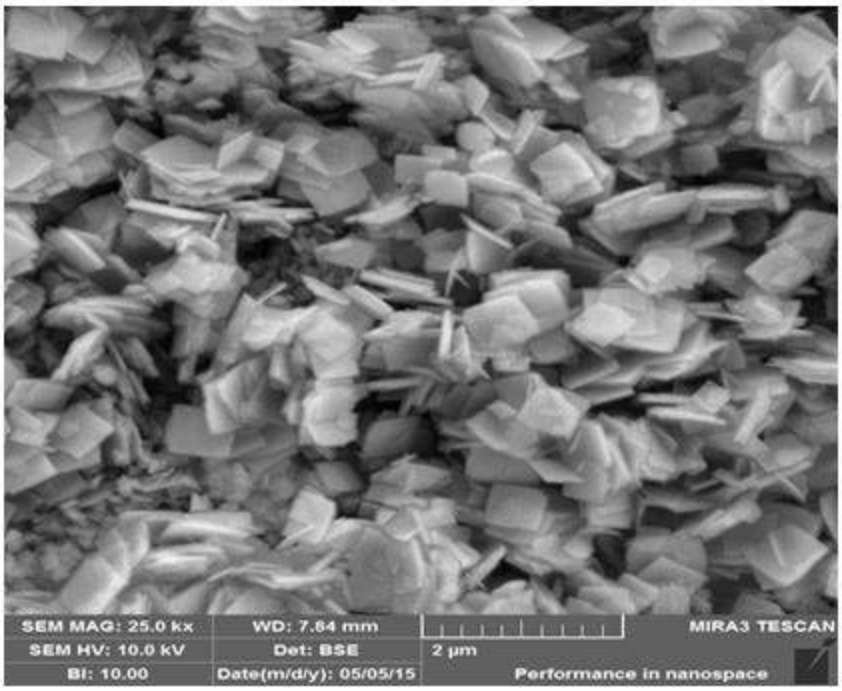

Figure 3.4: Synthesis of WO_3 square nanoplates

The nucleation of WO_3 subsequently started as the reaction temperature surpassed the decomposition temperature of H_2WO_4. The formation process of the WO_3 nanoplates can be described as [108].

$$\mathbf{Na_2WO_4 + 2HCl \rightarrow H_2WO_4 + 2NaCl} \quad (3.1)$$

$$\mathbf{H_2WO_4 \rightarrow WO_3 + H_2O} \quad (3.2)$$

For WO_3, (002) planes have higher energy compared to (020) and (200) planes. This leads to the preferential adsorption of anions to the high energy (002) planes, which inhibits the growth along these planes. Therefore, the nuclei undergo growth along other planes leading to a two-dimensional final morphology like nanoplates as shown in Figure 3.4.

3.5 Parameters optimization of prepared nanostructures

Here in this reports, the particle size, shape and phase purity of undoped and metal doped WO_3 nanoplates were controlled through optimization of reaction parameters. These are discussed briefly below.

3.5.1 Reaction temperature

The optimization of reaction temperature has great importance during WO_3 nanostructures synthesis using chemical co-precipitation techniques.

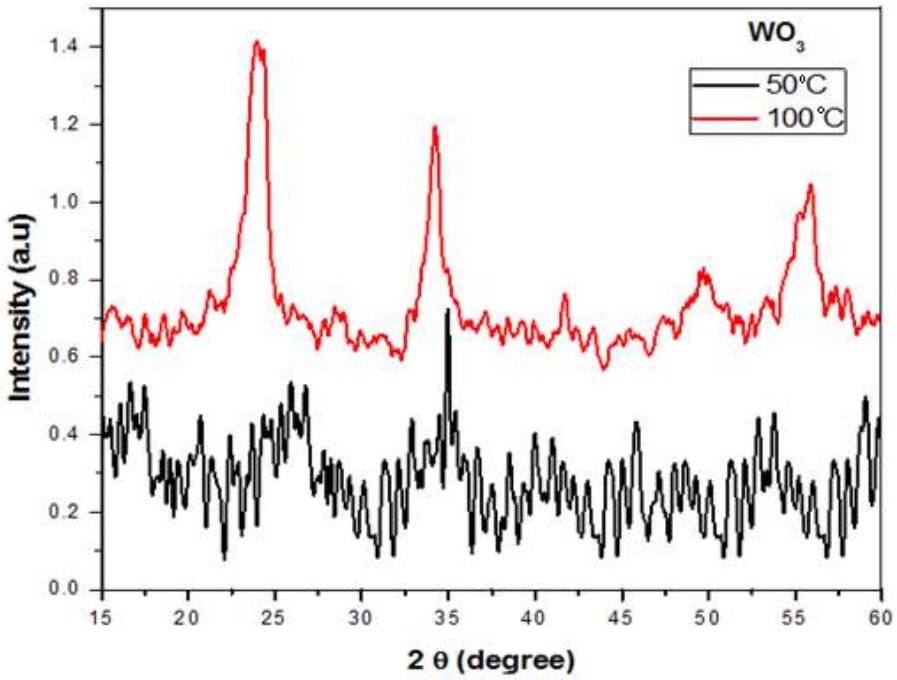

Figure 3.5 XRD behavior of sample prepared at 50 °C and 100 °C

To optimize the reaction temperature, the samples are prepared at two different temperatures and their XRD behavior is shown in Figure 3.5.Amorphous structure is obtained when sample were 50°C, while the sample treated at 100°C possesses the WO_3 monoclinic phase. At 100°C temperature, the better crystalline quality of WO_3 nanostructures is observed.

3.5.2 Role of pH

The reaction conditions, like pH, temperature, time and capping agent play a vital part to achieve the uniform fabrication of crystalline two-dimensional WO_3 nanoplates. The precipitates were not formed at pH 7.9 only with precursor ($Na_2WO_4.2H_2O$) solution without using HCl and NaCl by co precipitation procedure. Subsequently several drops of HCl were used to obtain pH down to 1. The required morphology can be obtained through the addition of precipitating agent (HCl). The SEM images of fabricated square nanoplates have been acquired at pH 1 as shown in Figure 3.4. The growth behavior can be well described by the renowned theory for crystal nucleation and growth [109-111].

3.5.3 Role of NaCl

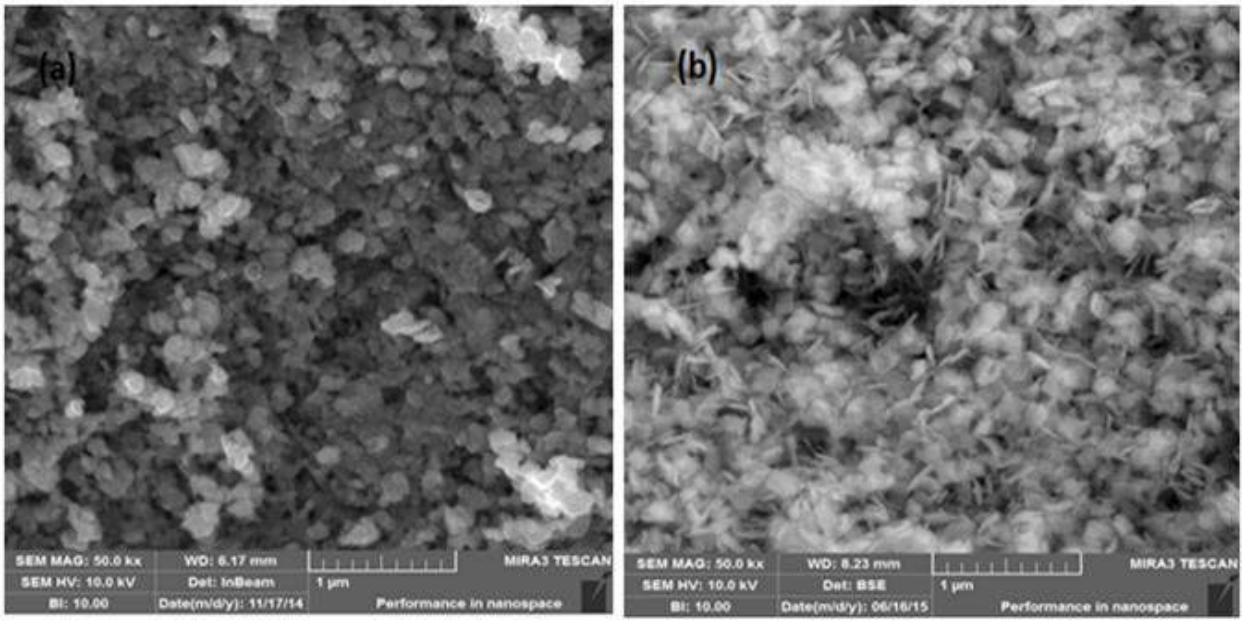

Figure 3.6: SEM images of undoped WO_3 nanostructures grown with (a) 0 gm, (b) 1.161 g NaCl concentration

The morphology and particle size of the WO_3 nanostructures can be modified with the introduction of capping agent in the solutions. Here, 1.160 g sodium chloride (NaCl) has been used as a capping agent to fabricate WO_3 square nanoplates. The generation of Na^+ ions and Cl^- ions were took place with the addition of NaCl into water.

These water based generated ions can attach to the various crystal planes of WO_3 nanoplates which alter the crystal orientation and growth rate. Figure 3.6 (a) represents the morphology of WO_3 when no NaCl was used in the reaction. The agglomerated nanoplates with bigger diameter and without a well defined shape were formed. However, Figure 3.6 (b) depicts the SEM images of square WO_3 nanoplates prepared using definite amount of NaCl. The particle size reduces with addition of NaCl.

3.6 Synthesis procedures

3.6.1 Fabrication of Fe doped WO_3 nanoplates

Synthesis of WO_3 nanoplates with different Fe doping concentrations were achieved via chemical co-precipitation method. HCl as precipitating agent was used during the fabrication of WO_3 nanostructures. Briefly, first, 0.1M aqueous solution of $Na_2WO_4.2H_2O$ was prepared. Subsequently, an appropriate quantity of NaCl was added. In order to maintain a pH of 1, suitable volume of 3M HCl was added in solution drop-wise. The solution was left for one hour under constant stirring, leading to the formation of nanoplates. Afterwards, the solution was centrifuged and washed to collect precipitates. The precipitates then dried at 80℃ over night. In order to synthesize Fe doped nanoplates, various concentrations (1, 3, 5 and 8 mol. %) of $FeCl_3 \cdot 6H_2O$ were also added and rest same procedure was adopted. Furthermore, annealing of samples was done at 300^{o}C for 2 hours in an electric oven.

3.6.2 Synthesis of Cu doped WO_3 nanoplates

First, 0.1M aqueous solution of $Na_2WO_4.2H_2O$ was prepared. Subsequently, an appropriate quantity of NaCl was added. In order to maintain a pH of 1, suitable volume of 3M HCl was used. The solution was left for one hour, leading to the formation of nanoplates. The solution was centrifuged and dried. In order to synthesize Cu doped nanoplates, various concentrations (1, 3, 5 and 8 mol. %) of copper chloride ($CuCl_2.5H_2O$) were also added and rest same procedure was adopted. Furthermore, annealing of samples was done at 300^oC for 2 hours in an electric oven.

3.6.3 Synthesis of Sn doped WO_3 nanostructures

The undoped and 1, 3, 5 and 8 mol. % Sn doped WO_3 nanoplates were fabricated through chemical solution based techniques. Same above mentioned procedure was also repeated for the synthesis of Sn doped samples except for the addition of different molar percentages of $SnCl_4 \cdot 4H_2O$ to obtain 1, 3, 5 and 8 mol. % Sn doped WO_3.

3.6.4 Synthesis of Co doped WO_3 nanoplates

In order to synthesize Co doped nanoplates, various concentrations (1, 3, 5 and 8 mol. %) of $CoCl_2.6H_2O$ were also added and rest same procedure was adopted as mentioned previously.

3.6.5 Synthesis of Ni doped WO_3 nanoplates

2.445 gm of $Na_2WO_4.2H_2O$ was added into the distilled water, to make 0.1 M solution, under continuous magnetic stirring of 500 rpm. For doping, different molar ratios of $Na_2WO_4.2H_2O$ and ($NiCl_2.6H_2O$) were dissolved into distilled water to get 0, 1, 3, 5 and 8 mol. % Ni doped WO_3 nanoplates. Then 1.160g of NaCl was used. The pH value of ($Na_2WO_4.2H_2O$ and

$NiCl_2.6H_2O$) solution was maintained at 1 by adding 3M HCl solution drop-wise. Furthermore, the solution was stirred at 500 rpm on magnetic stirrer for 1 hour at 100^oC and centrifuged. No free Ni ions were detected in the filtrate. Finally, the obtained precipitates were dried and annealed.

3.7 Photocatalytic degradation mechanism

The photocatalytic degradation activities of the undoped and (Fe or Sn or Cu or Co or Ni) doped WO_3 nanoplates were tested for visible light driven photodegradation of methyl red (MR, dye). For this work, 2.0 mg of the photocatalyst, undoped and (Fe or Sn or Cu or Co or Ni) doped WO_3 nanoplates were used for photodegradation of MR solution. The 20mL aqueous methyl red solution (10 mgL^{-1} concentration) was utilized. This solution was furthered sonicated for 10 min in the dark. The solution was placed in dark for 30 min to obtained adsorption–desorption equilibrium of the dye on the catalyst surface. The visible light illumination was achieved with 500 W tungsten halogen lamp (Philips). The distance between the lamp and the reactor (catalyst containing MR solution) was maintained 16 cm. A UV- filter glass was placed between the lamp and the catalyst containing MR solution to block the light with a wavelength of less than 400 nm. Light intensity was measured by a UV radiometer. The lamp filtered visible light intensity was measured to be 347 mW/cm^2. Methyl red degradation experiments were performed for 2 hours. The degraded sample of about 1.7 mL for each set was taken after 0.5 hour intervals using a micropipette, centrifuging it to eradicate the catalyst and then finally recording the UV-vis absorption spectrum. The UV-vis- spectrophotometer was used to measure the photodegradation activities relating to times. The degradation of methyl red has direct link with decrease in

absorbance of the solutions. The photodegradation percentages were calculated using the expression given below:

$$\textbf{Photodegradation}\ (\%) = \frac{\textbf{Co - C}}{\textbf{Co}} \times \textbf{100} \qquad (3.3)$$

Where the concentration of MR before irradiation is C_o and C is after irradiation. Each experiment was carried out three times to ensure the consistency of the photocatalytic degradation activities. The degree of mineralization was monitored using total organic carbon (TOC) analysis under typical experimental conditions using a SHIMADZU TOC VSCH analyzer.

3.8 Cytotoxicity determination through MTT assay

The cancerous and healthy cells were grown and sustained in RPMI 1640 supplemented with 10% fetal bovine serum (FBS) and 5% antibiotics–antimycotic solution (GPPS) at 37 °C in CO_2 incubator (SHEL Lab, USA). RPMI 1640 culture media, the GPPS and FBS were acquired from Invitrogen (USA). The consumables items like plastic and culture wares were commercially obtained from Corning (USA). The standardized protocol was used to measure the percent cell viability of cancer cells using the MTT assay. Initially with 10% FBS and 5% GPPS, the cells were grown and maintained in RPMI 1640 at 37°C within CO_2 incubator. In brief, 96-well culture plates were used to seed these cells (1×10^5) and permitted to grow for 24 hours at elevated humidity atmosphere with 5% CO_2 at 37°C. After that 25µg/µL concentration of undoped and (Fe or Sn or Cu or Co or Ni) doped WO_3 nanostructures, were exposed against these grown cells for 24 hours. In the next step, MTT (5 mg/ml of stock in PBS) was added (10 µl/well of 100 µl of cell suspension) and these plates were incubated for 4 hours. The reaction

solution was removed on the completion of incubation period. Subsequently in every well, 100µl of DMSO was inserted and mixed gently. These plates were maintained at 37°C for 60 min on shaker. At the end, a Platos R496 Micro-Plate Reader (Austria) was used to read the absorbance at 550 nm. Untreated sets were also processed in the same conditions and referred as the controls.

3.9 Characterization and processing techniques

The characterization is the toll to achieve the in-depth information and analysis of the synthesized nanostructures about their structure, morphology and number of different properties. For this purpose various methods and techniques have been developed. A brief discussion on each of techniques is given below.

3.9.1 X-ray diffraction (XRD)

The structures of the prepared nanostructures have been examined through XRD in material science. XRD is a analytical method to evaluate synthesized nanomaterials crystallite size, phase, structure, lattice constants and chemical composition. Materials can be found both in crystalline and amorphous forms. There are various methods of diffraction pattern measurement but the powder diffraction method is preferably better for the identification and characterization of polycrystalline phases.

Bragg's law successfully explains the X-ray diffraction. The scattered rays are in phase, when the extra distance travelled by a ray is in integer multiple of incident wavelength i.e.

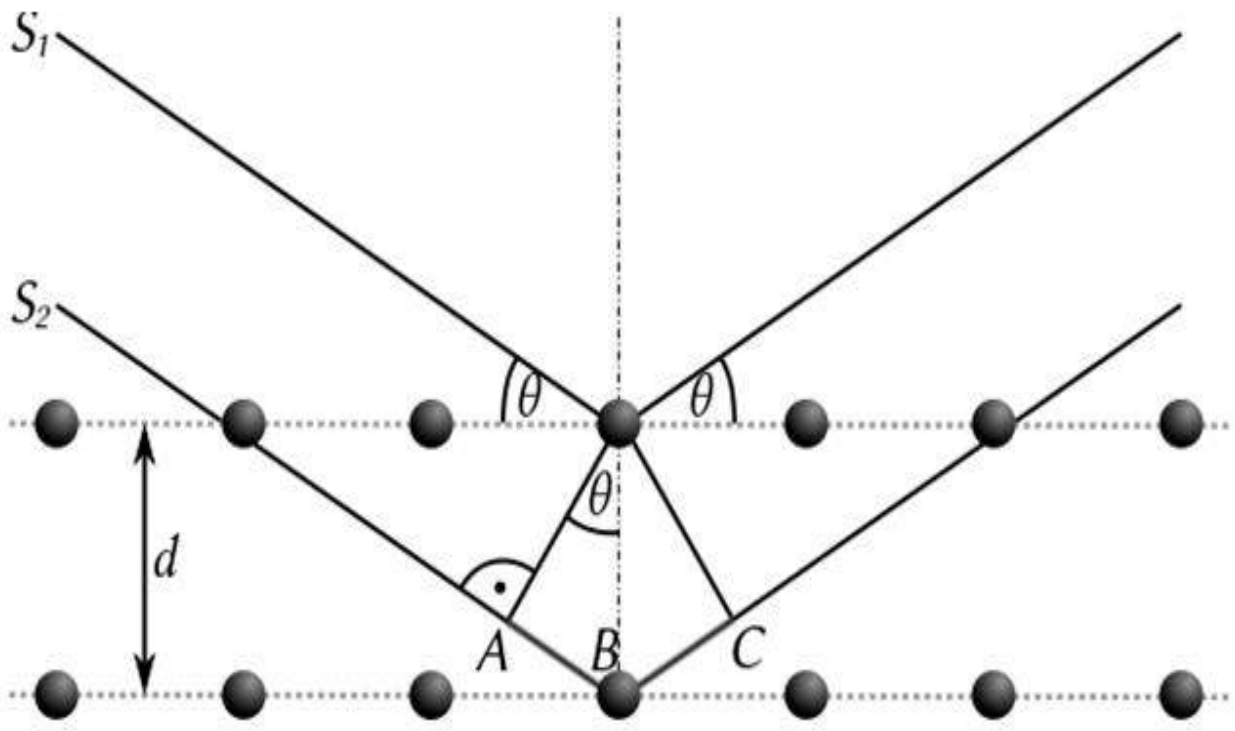

Figure 3.7 Bragg's law

$$2d\sin\theta = n\lambda \qquad (3.4)$$

Where θ is Bragg's angle, wavelength of X-rays is λ, diffraction angle is 2θ, crystal interplanar distance is d, and order of diffraction is depicted by n.

3.9.2 Scanning electron microscopy (SEM)

SEM is utilized to view and examine the surfaces of the synthesized nanomaterials. It provides us the information about different parameters information such as surface quality, shape, density, diameter, thickness, length and orientation of the as synthesized nanostructures. The basic principle of SEM can be described here: In high vacuum chamber, exceptionally short

wavelength of electron beam is focused on the sample with the guidance of electromagnetic lenses.

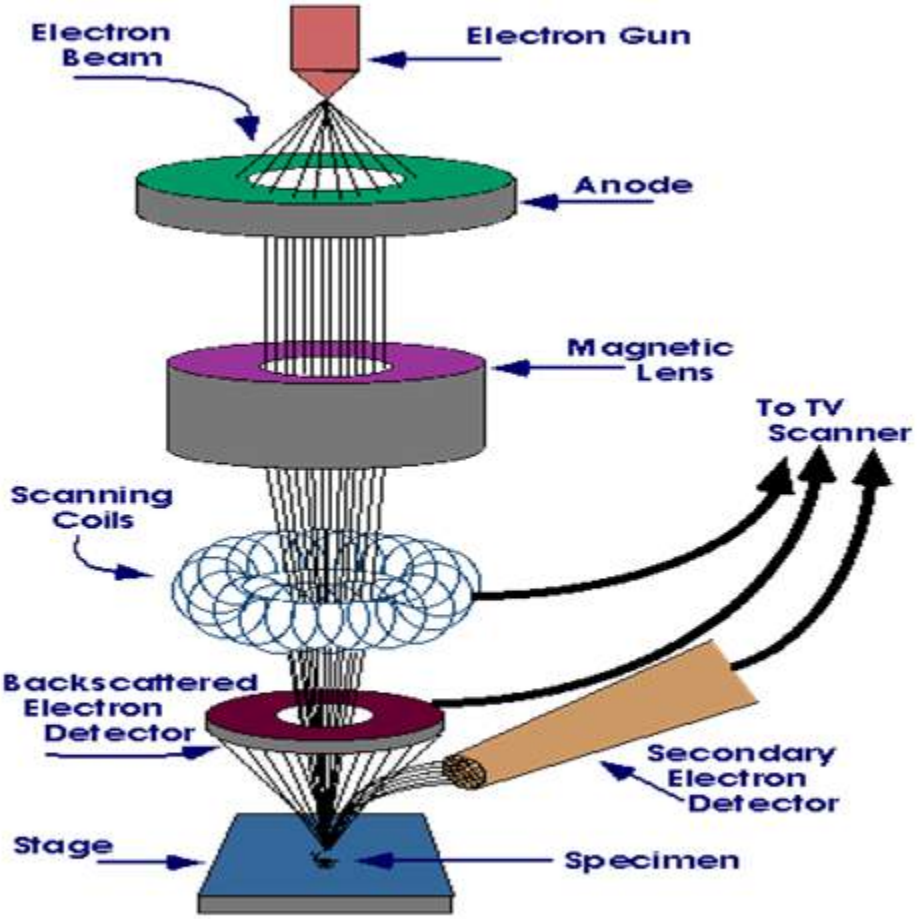

Figure 3.8 SEM schematic diagram

Different electrons are emitted e.g. backscattered electrons, secondary electrons, Auger electrons and X-rays. The detectors are placed to detect these signals in the sample chamber and connected with the computer. Sample image of surface topography is provided by the secondary electrons. The surface charging effects has been avioded through gold, silver or carbon coating on the samples.

3.9.3 Energy dispersive X-ray spectroscopy (EDX)

The material chemical composition can be analyzed effectively through EDX technique. The presence of each element in the sample is observed using EDX. EDX setup is mostly attached with SEM. It depends on samples interaction with inner shells X-ray excitation. Each element possesses its unique X-ray pattern and registers a distinctive peak. So, it can be used to investigate specimen composition. EDX consists of electron beam source which acts as an excitation source to generate X-rays.

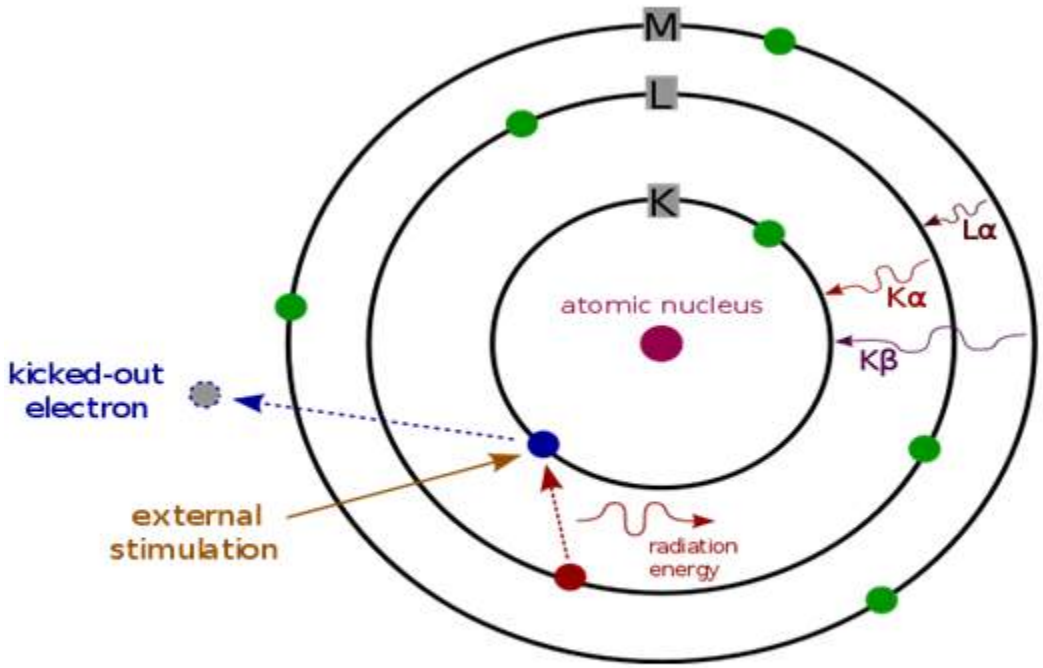

Figure 3.9 Schematic diagram of working principle of EDX.

X-ray detector detects the X-ray produced by the excitation source and a pulse processor that generates pulse. High energy beam of electrons is interacts with sample and emission of X-rays takes place. The incident beam excites the electrons in inner shell. The excited electrons create

holes in inner shells. The electrons from outer shell come to fill the holes vacancy. X-rays are emitted during this event due to energy difference between these two shells. So, we can measure the intensity of X-rays with the energy dispersive spectrometer.

3.9.4 Fourier Transform Infrared (FTIR) and Raman vibrational spectroscopy

The use of FTIR and Raman spectroscopic techniques is the best approach to investigate the vibrational and structural properties of synthesized samples. It is essential to utilize both approaches for a comprehensive picture.

3.9.4.1 FTIR spectroscopy

In FTIR spectroscopy, Michelson interferometer is the core of instrument in which the interference of two beams of radiation produces interferogram. When the particular wavelength of radiation falls on sample molecules, it selectively absorb the radiations which causes variations in their dipole moment and as an outcome FTIR spectrum is formed due to molecular vibrations or phonon modes present in the sample. Certain selection rules have been applied to detect vibrational or phonon modes of the sample material because each polar bond of material has its own particular frequency for excitation. Therefore every material has it specific spectrum. The knowledge about the crystalline quality and crystal structure of the material can also be obtained through peak height, width and position. The bulk WO_3 material has low surfaces to volume ratio of atoms while nanostructuring of WO_3 has created very high surface to volume ratio of atoms. This introduces additional chemical reactivity in to WO_3 nanostructures and as consequence different functional groups can be attached by design or by chance with the surface

in WO_3 nanostructures. The FTIR spectra also reveal the functional groups of molecules which can excite through infrared radiations.

3.9.4.2 Raman spectroscopy

The key advantage of Raman spectroscopy is that it is more effective, sensitive and versatile spectroscopic approach as compared to Fourier transforms infrared spectroscopy. The vibrational, rotational and various frequency modes have been utilized in Raman spectroscopy. In Raman spectroscopic experiments the laser light is used. Different phenomenon that takes place under light illumination and one of the following light scattering can be occurs as shown in Figure 3.10.

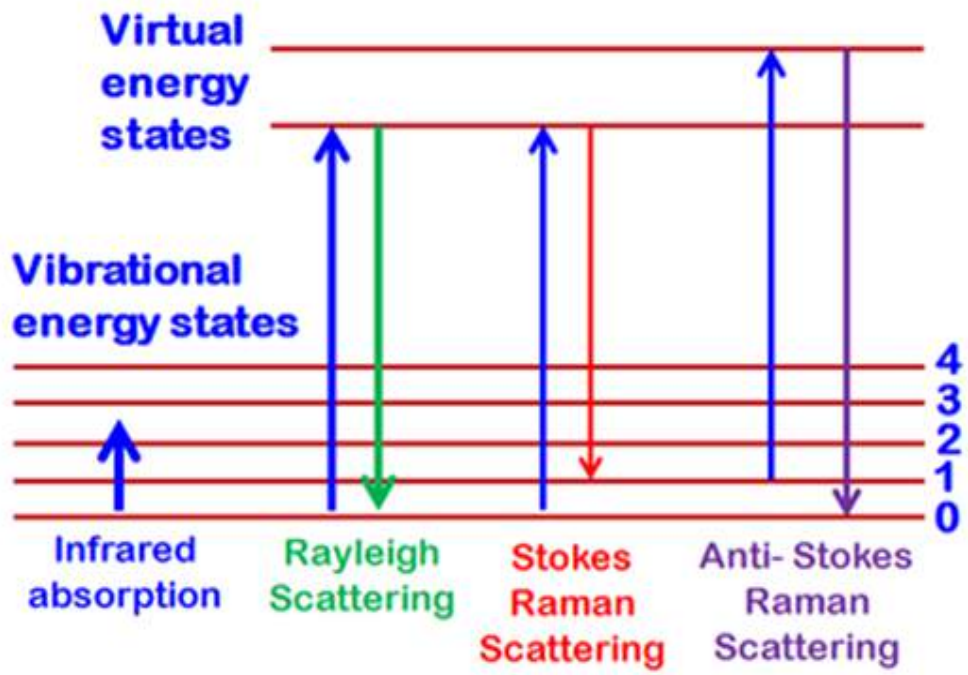

Figure 3.10 Raman spectroscopic scattering under irradiation of light.

3.9.5 X-ray photoelectron spectroscopy (XPS)

The XPS technique is utilized to distinguish the surface recombination centers through surface composition analysis. This procedure depends on the photoionization effect. Under the interaction of x rays, the core electrons obtain minimum required energy through X-rays photons then it will emit from the atom with particular kinetic energy. The electron kinetic energy and photon energy is represented as follows

$$EE_{KK} = h_{vv} - EE_{bb} \quad (3.5)$$

The h_{vv} is the X-ray photon energy, EE_{bb} is the binding energy and EE_{KK} is the kinetic energy. The ultra high vacuum (base pressure of 10^{-10} mbar) has been applied in XPS measurements. The photoelectron has zero degree take-off angles at room temperature in XPS measurements. The Fermi level is used as a reference to achieve the binding energies with an error of ± 0.1 eV.

3.9.6 UV- Vis absorbance measurements

The dye absorbance in photodegradation experiments were founds out through UV-vis spectroscopy experiments between 300-800 nm wavelength regions. Beer-Lambert's law has been utilized to calculate the concentration of absorbing species in dye solution on quantitative analysis bases. Figure 3.11 is reveals the schematic illustration of UV-vis set up.

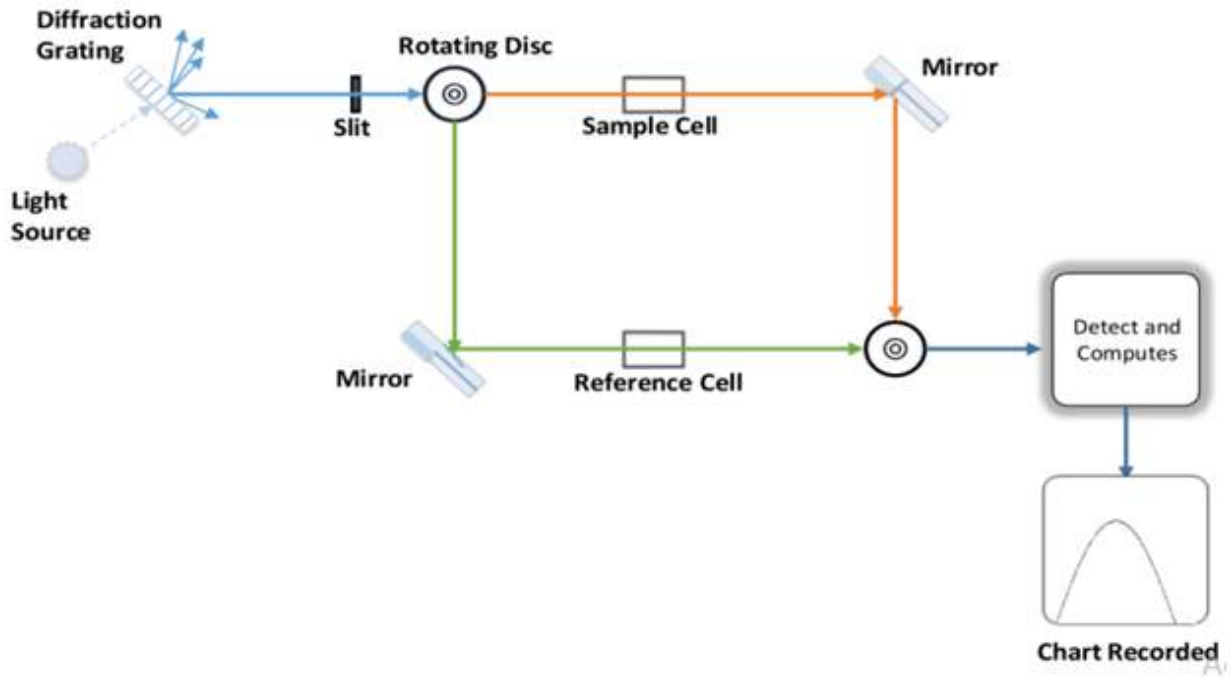

Figure 3.11 The schematic diagram of UV-Vis set up.

3.9.7 Diffused reflectance spectroscopy (DRS)

The ultra violet (UV), visible and infrared light region has been used to observe the optical transitions. The electrons can easily excite from lower energy state to higher energy states by absorbing rays of certain wavelength incident on them. In this DRS technique, the scattering of light take place in different directions of the sample and then scattered light is collected through optical detector. The scanning of the sample over wide range of wavelengths provides the surface reflectance. Figure 3.12 shows diffuse reflectance of a sample under irradiation of light. The band gap energy calculations are achieved with DRS technique.

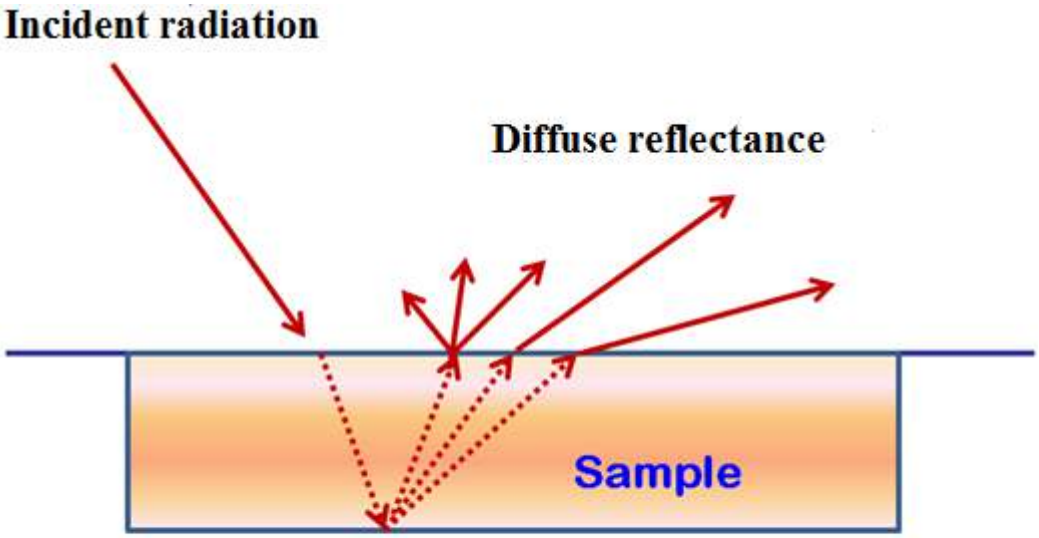

Figure 3.12 Sample diffuse reflectance under irradiation of light.

.

3.9.8 Photoluminescence spectroscopy

The phenomena of photoluminescence take place due to optical excitation under the illumination of light. The highly energetic photons are absorbed on material surface under irradiation of high intensity of light which causes electronic excitations in the materials. After fraction of seconds, the electrons come back to ground state with emission of energy. During this phenomenon, if radiative relaxation happens than the emitted light is called photoluminescence. Some important information can be collected from photo excited material during the detailed analysis of emitted light. The transitions energies can obtain from photoluminescence spectrum which is helpful to measure the electronic energy levels. The luminescent intensity provides a measure of the relative rates of radiative recombination. It provides information about charge separation of the sample under light illumination. The defects are also examined by photoluminescence spectroscopy.

3.9.9 Electrical parameters calculations through LCR meter apparatus

The LCR meter is multipurpose apparatus which gives precise, quick and efficient information at multi-frequencies ranges.

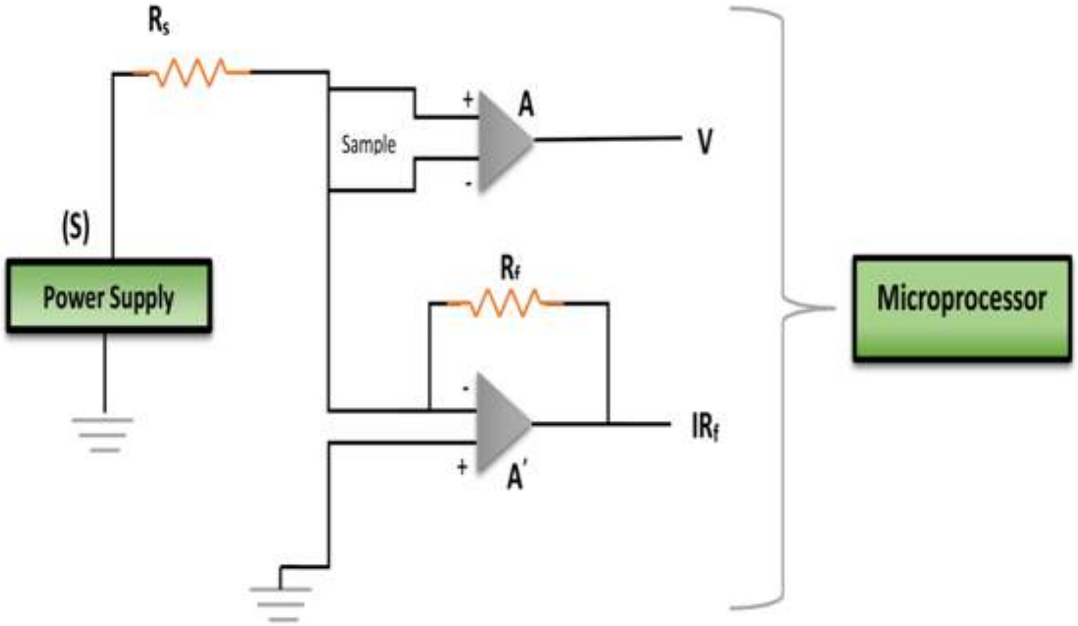

Figure 3.13 Schematic diagram of LCR meter.

Various electrical parameters such as AC conductivity, dielectric constant (ε') and dielectric loss (ε") are measured accurately. Generally, the LCR meter is based on following components such as power supply, AC voltage, broad frequency and amplitude. The systematic diagram of LCR meter is shown in Figure 3.13.

CHAPTER 4

SYNTHESIS, CHARACTERIZATIONS, PHOTOCATALYTIC AND ANTICANCER ACTIVITIES OF Fe DOPED WO_3 NANOSTRUCTURES

4.1 Introduction

Photocatalytic materials have derived intense interest owing to the increased water pollution issues [112]. The best choice is to utilize photoactive materials which harvest sun light on a large scale. Therefore, visible light driven photocatalysis technique has gained much attention due to photo energy utilization, low operating cost and the absence of any secondary pollution [113-117]. Tungsten trioxide (WO_3) is believed to be one of the best photocatalyst due to excellent electron transport properties, high stability, high photo-activity and lack of photo-corrosion [118-120]. But the photocatalytic performance of WO_3 is restricted because of its comparatively broad band gap (2.8–3eV), which means that WO_3 can only be excited by blue or near ultra violet (UV) regions of solar spectrum [121-124]. Narrowing of band gap of the WO_3 based photocatalysts would be very attractive because it will enhance their photocatalytic efficiency. Selective metal ions doping into WO_3 host matrix is considered as an excellent strategy to narrow down its band gap. Previously, numerous research groups have worked on the tailoring of the band gap of WO_3 by doping different metal ions such as Ti, V, Zn, Fe, Mg and Mo [84, 87, 91, 125-128]. Among all dopants, Fe is best choice due to the fact that it can be easily doped into WO_3 lattice because of almost alike ionic radii of W^{6+} (0.62 Å) and Fe^{3+} (0.64 Å) ions [129]. Moreover, huge number of free charge carriers are produced due to reduction in bandgap which ultimately take part in the enhancement of the photocatalytic activities and anticancer properties [130, 131]. The other

possible approach to enhance the photodegradation properties is to tune its morphology and structural characteristics [132-134]. The photodegradation activities of WO_3 have been significantly enhanced with nanostructuring [135, 136]. At nano scale, surface area of WO_3 increases dramatically, and the diffusion length for photo-generated electron hole pair is shortened [137-139]. In addition to the size, the shape of WO_3 nanostructures has also previously been reported to a play vital role in determining its photocatalytic performance [140]. It has been reported that two dimensional pure WO_3 nanoplates have higher photocatalytic activity as compared to nanorods and nanospheres due to their sharp edges and corners [140]. In this chapter, undoped and Fe doped WO_3 nanoplates have been synthesized via soft chemical co-precipitation technique.

4.2 Results and discussions

4.2.1 X-ray diffraction and scanning electron microscope studies

The crystallographic structure of the synthesized samples has been characterized by XRD. The XRD patterns of the prepared samples (undoped and Fe doped WO_3) are shown in Figure 4.1. The found diffraction peaks are well consisted with the monoclinic WO_3 crystal structure (JCPDS card No.043-1035) having lattice constants a = 7.297 Å, b = 7.539 Å and c = 7.688 Å. With Fe doping, no apparent peaks related to iron oxide has been observed suggesting that the Fe ions are successfully doped into WO_3 . This may be due to smaller concentration of Fe ions and little variation between the ionic radii of host W^{6+} (0.62 Å) and dopant Fe^{3+} (0.64 Å) ions. Hence, Fe^{3+} ions may easily be substituted for W^{6+} ions in the host matrix and forming Fe-WO_3 finite solid solution. However, broadening and decrease in X-ray diffraction peaks intensity may indicates the poorer crystalline quality with doping. This could be due to the reduction in crystallite size and slight lattice mismatch [141].

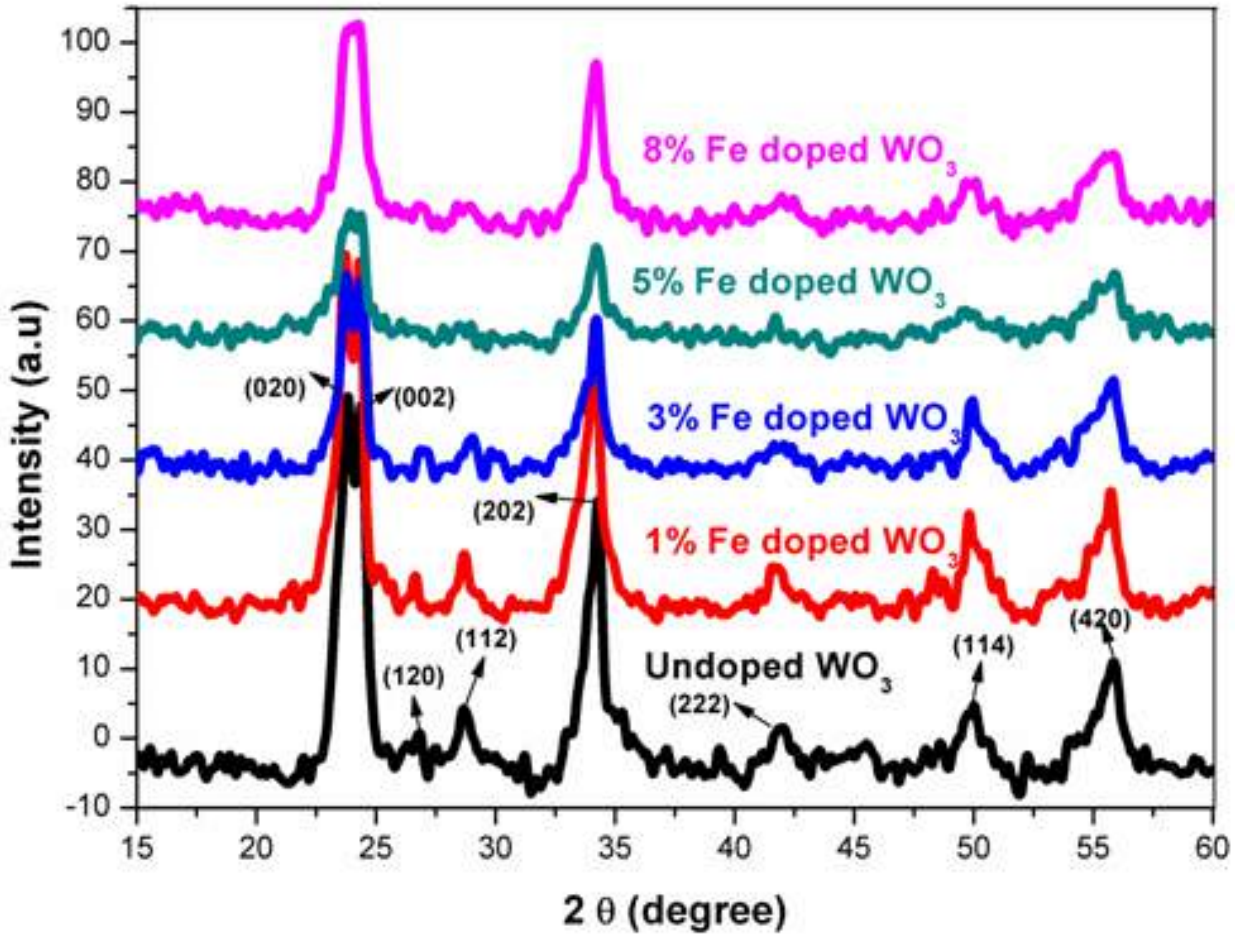

Figure 4.1 XRD patterns of nanoplates.

The morphologies of prepared pristine and Fe doped WO_3 samples have been presented in Figure 4.2. SEM micrographs suggest that the prepared pristine WO_3 sample is comprised of nanoplates having average thickness and diameter of about 45 nm and 200 nm respectively. Fe doping has slightly decreased the thickness and diameter of nanoplates as evident from Figure 4.2(b-e). The detailed growth mechanism of two dimensional WO_3 nanoplates has already been discussed.

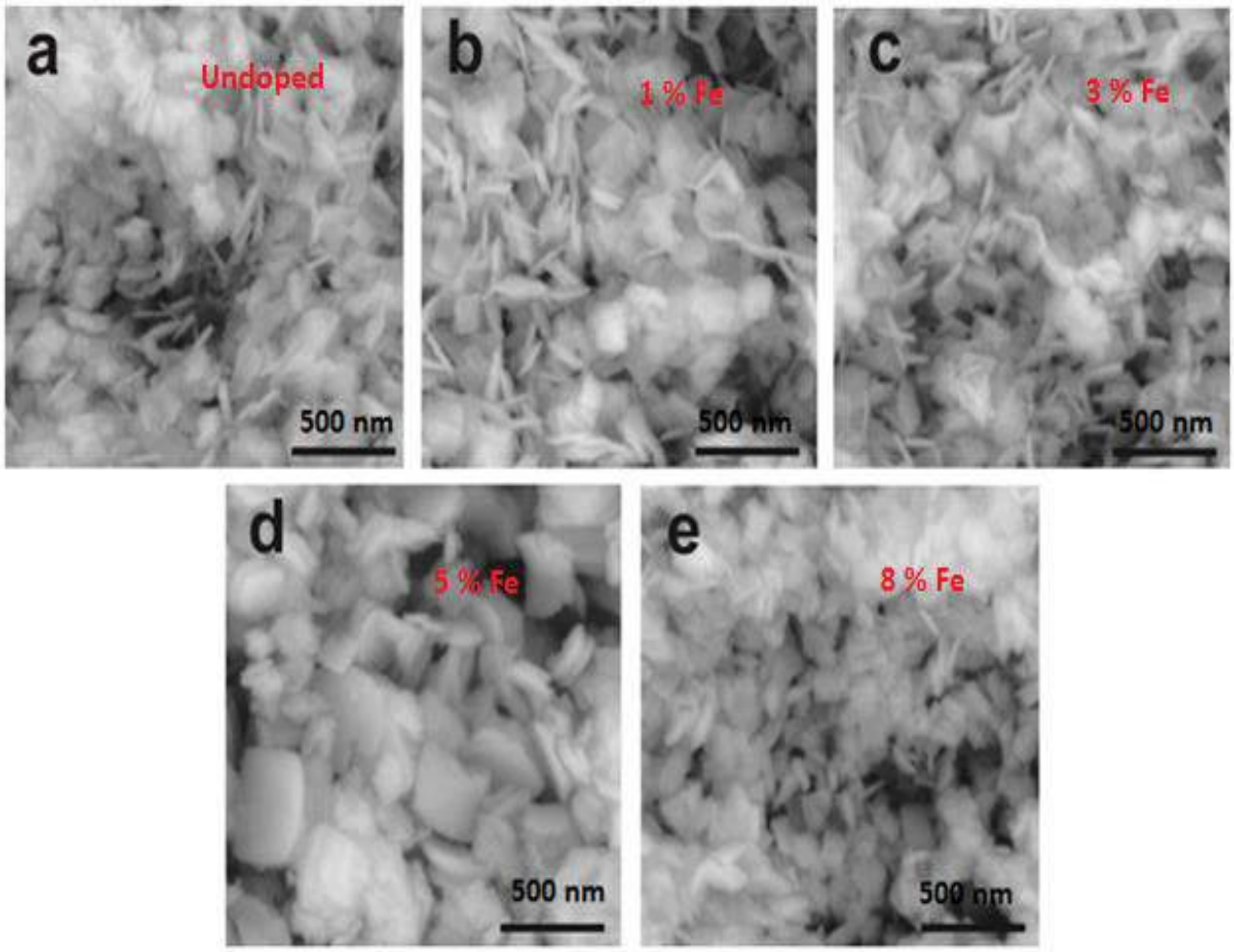

Figure 4.2 SEM images of fabricated nanoplates.

Figure 4.3 depicts the energy-dispersive X-ray spectroscopy (EDX) spectra of synthesized nanoplates. The EDX spectra have revealed the existence of Fe ions in doped nanoplates by displaying Fe peaks while these peaks are absent in undoped samples.

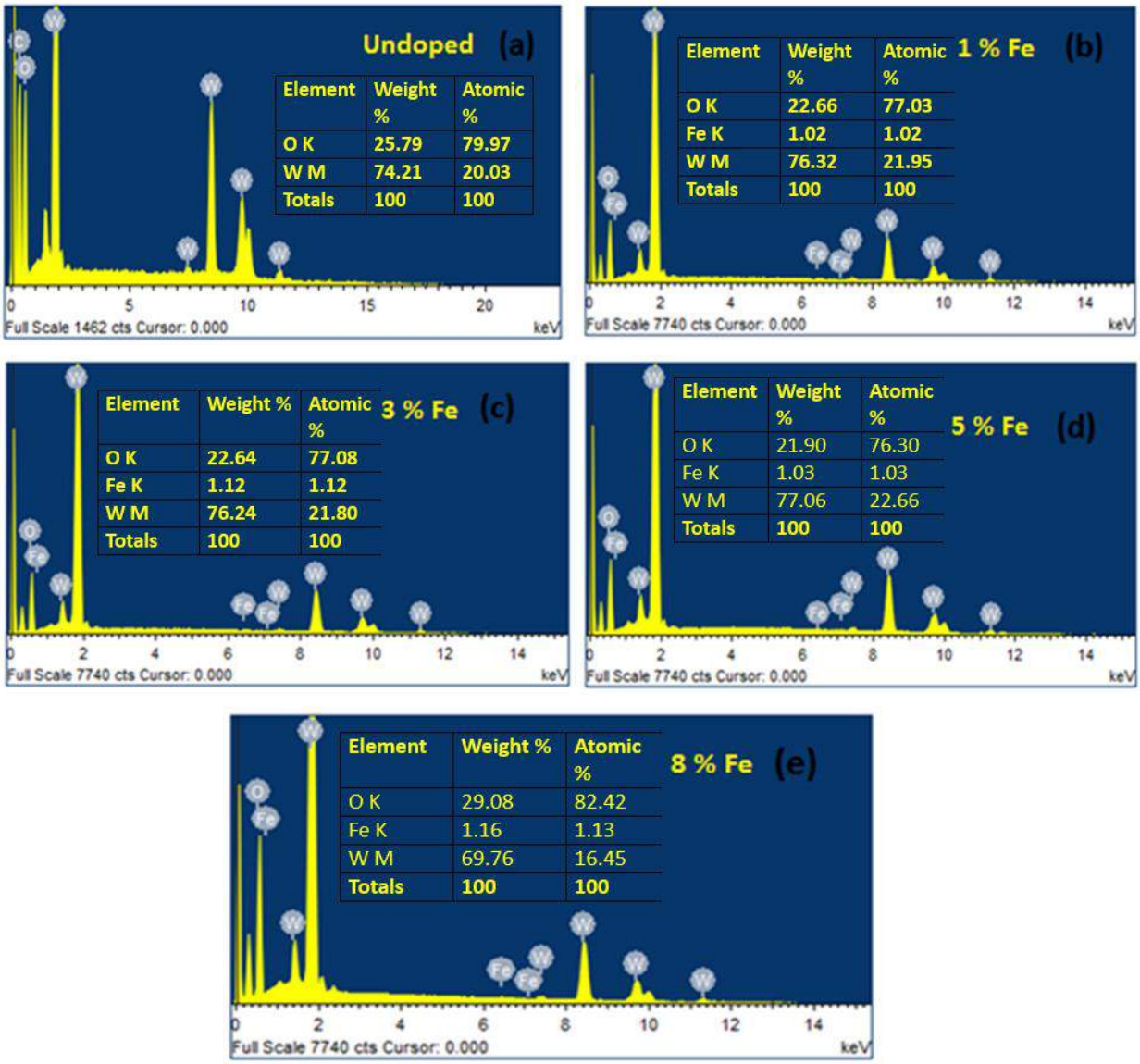

Figure 4.3 EDX spectra.

4.2.2 FTIR and Raman spectroscopic analysis

The knowledge about surface chemistry of nanostructures is highly desired due their higher surface reactivity. The FTIR spectra of fabricated nanomaterials are revealed in Figure 4.4.

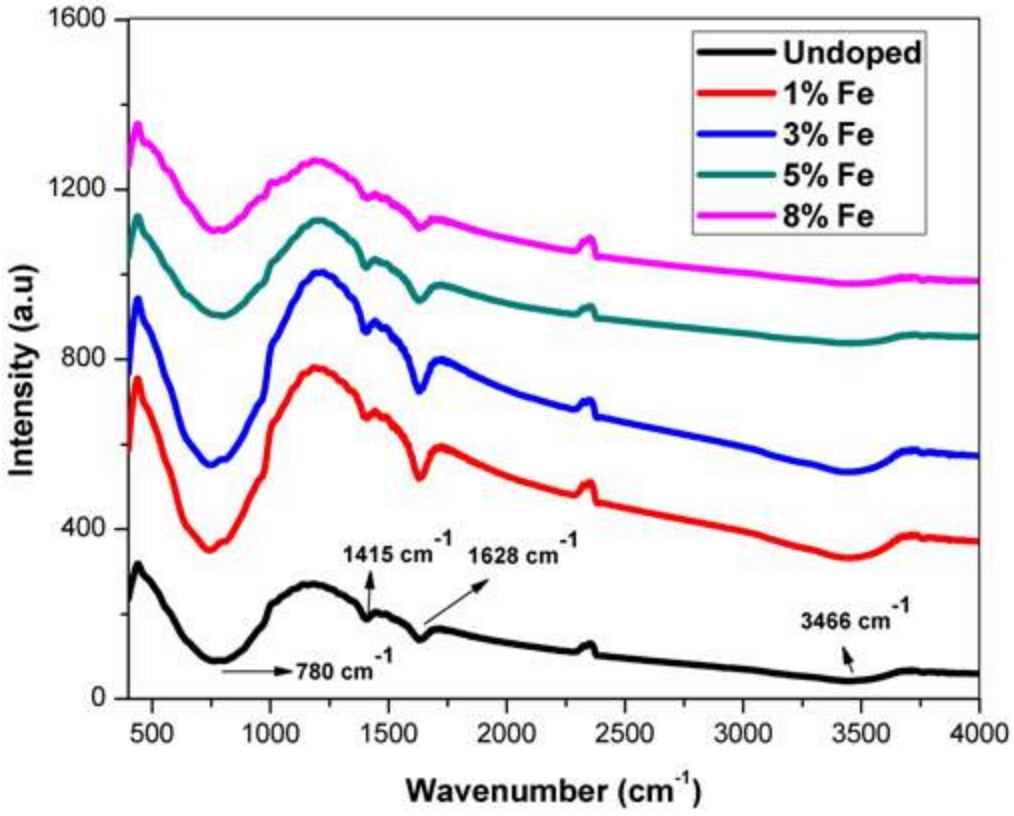

Figure 4.4 Synthesized nanoplates FTIR spectra.

The band found at 780 cm^{-1} is links to the stretching vibration of O-W-O [66]. The other observed vibration modes at 1415cm^{-1} and 1628 cm^{-1} belong to the tungsten-hydroxyl (W–OH) bond but the intensities of these absorption bands are very low which suggest the presence of very minute hydration of the prepared nanostructures. The stretching vibrational mode of O−H groups in H_2O or hydroxyls has been found at 3300-3600 cm^{-1} [142]. Hence, FTIR results again confirm the formation WO_3 in all samples with doping.

To further obtain more information about structural and existence or absence of vibrational modes Raman spectra for undoped and doped WO_3 nanoplates have shown in Figure 4.5.

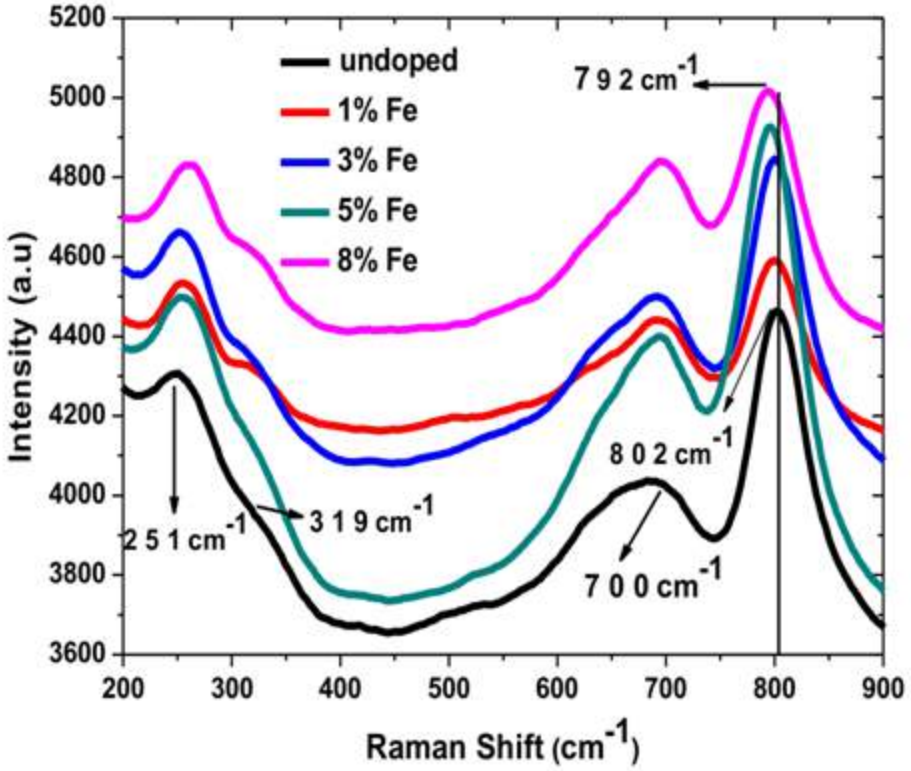

Figure 4.5 Raman spectra of undoped and Fe doped WO_3 nanoplates.

The υ (O–W–O) stretching vibrational modes and δ(O–W–O) bending vibrational modes, found at 700, 802 cm^{-1} and 251, 319 cm^{-1} respectively, may be linked to monoclinic WO_3 [143]. The presence of two υ (O–W–O) stretching vibrational modes as figurative peaks of WO_3 [144]. These observed Raman bands verify the monoclinic crystal structure. Upon Fe doping, no Raman bands related to Fe-O have been observed. A shift in Raman peak positions towards lower wave number has been observed with Fe doping. Some studies have attributed this shift to Fe ions occupying the substitutional sites in monoclinic WO_3 matrix [145]. While the band position in Raman spectrum of WO_3 may be strongly correlated with W content and shift in peak position is the consequence of Fe doping due to the different valance states of Fe^{3+} ions and W^{6+} [128]. Hence, Raman results have strong agreement with XRD and FTIR results regarding

formation of single phase and also hint towards variation in defect densities in host matrix (upon Fe doping).

4.2.3 X-ray photoelectron spectroscopy (XPS) studies

The XPS spectrum of undoped WO_3 nanoplates has been shown in Figure 4.6 (a) depicting the presence of O, W, C and N elements. Their corresponding photo electron peaks have been found to be O1s, W4p, W4d, W4f, C1s and N1s. The W4f peak is the most intense peak. The core level XPS spectrum of W4f has been depicted in Figure 4.6 (b) which hints the existence of two peaks associated to $4f_{5/2}$ and $4f_{7/2}$. The presence of these peaks at corresponding energy values demonstrates that W elements in the sample exist in the form of W^{6+} [146]. The XPS spectra of 3 and 5 mol. % Fe doped WO_3 nanoplates have been described in Figure 4.6 (c) and (d) respectively. All the photo electron peaks have been found to be the same as observed for undoped WO_3 except the presence of Fe2p peak. The core level XPS spectrum of Fe2p for 3 and 5 mol. % Fe doped WO_3 nanoplates have been shown in the inset of figure 6 (c) and (d) respectively. It has been observed that there are two peaks related to $Fe2p_{3/2}$ and $Fe2p_{1/2}$ which depicts that Fe is incorporated in the host matrix of WO_3 nanoplates in the form of Fe^{3+}.

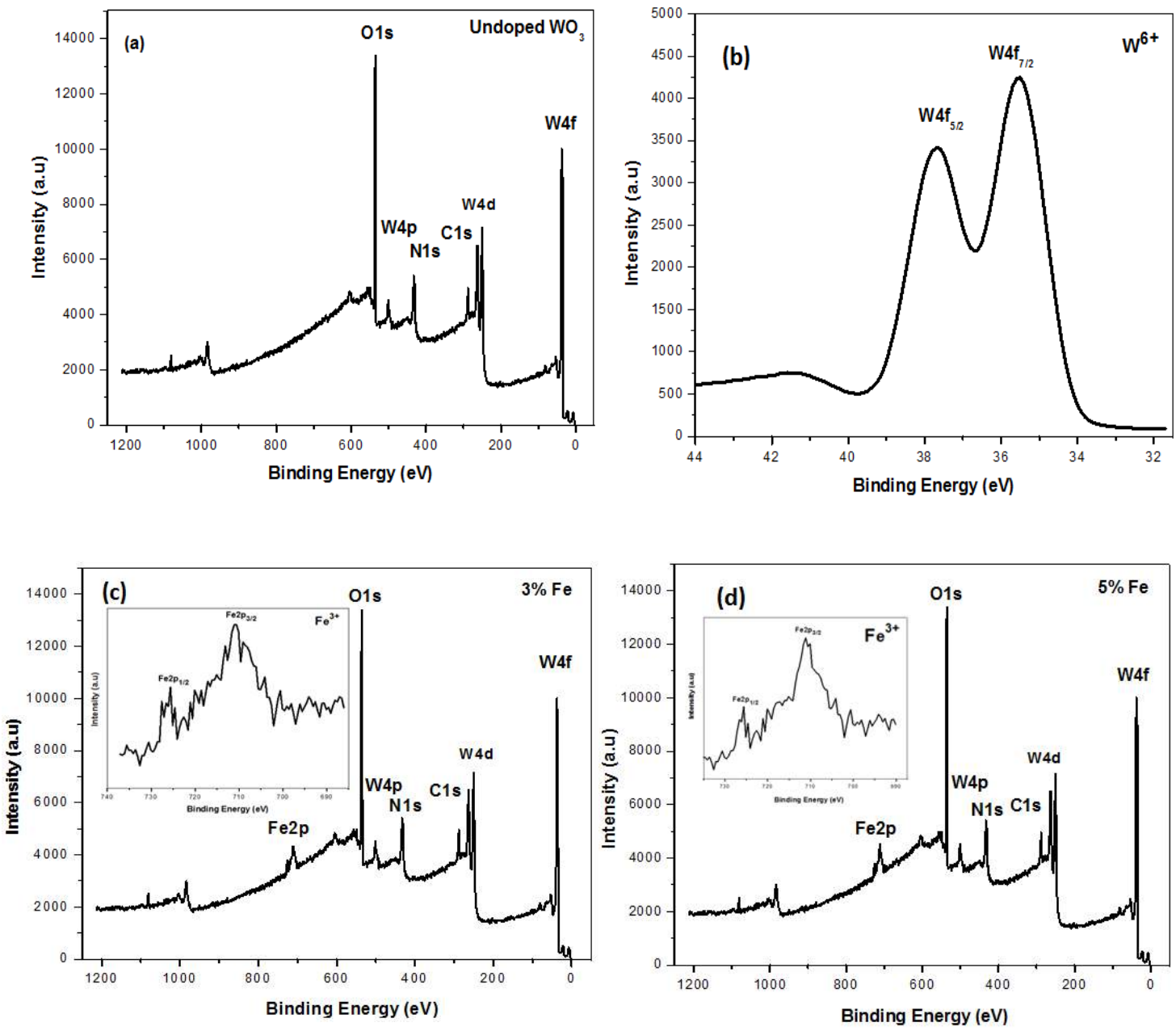

Figure 4.6 XPS spectra of **(a)** undoped WO_3 nanoplates, **(b)** core level spectrum of undoped WO_3 nanoplates **(c)** 3% Fe doped (inset of the figure depicts the plot Fe2p) and **(d)** 5% Fe doped WO_3 nanoplates (inset of the figure depicts the plot Fe2p).

4.2.4 Optical characteristics investigations

Figure 4.7 describes the DRS spectra of the prepared nanoplates. The optical band gap energies of the prepared nanoplates could be confirmed by Kubelka-Munk relates which is expressed as follows [144].

$$\mathbf{F(R)} = \frac{\mathbf{(1-R)^2}}{\mathbf{2R}} \qquad (4.1)$$

Where $\mathbf{[F(R)\,hv] = A\,(hv - Eg)^n}$ (4.2)

Where F(R) is Kubelka-Munk function and R represents the diffuse reflectance. For WO_3, the value of n which is dependent on properties of band gap is considered 2 (indirect transition) [146, 147]. The classification of transition is based on the value of exponent 'n' [148]. The values of indirect bang gap energies have been determined in the inset of Figure 4.7. The band gap energy for undoped WO_3 nanoplates has been measured to be 2.54 eV which is reduced down to 2.47, 2.39, 2.05 and 2.02 eV for 1%, 3%, 5% and 8% Fe doped WO_3 nanoplates, respectively. This reduction can be understood on the basis of hybridization between Fe 3d orbital and the O 2p orbital. As it is well known that in case of pristine WO_3, valance band is dominated by O 2p and conduction band is dominated by W 5d orbitals. But when Fe ions are introduced in the system, their 3d orbitals emerge around valence band and induce slight positive shift in it. Besides, Fe ions can also lead to downshift of conduction band.

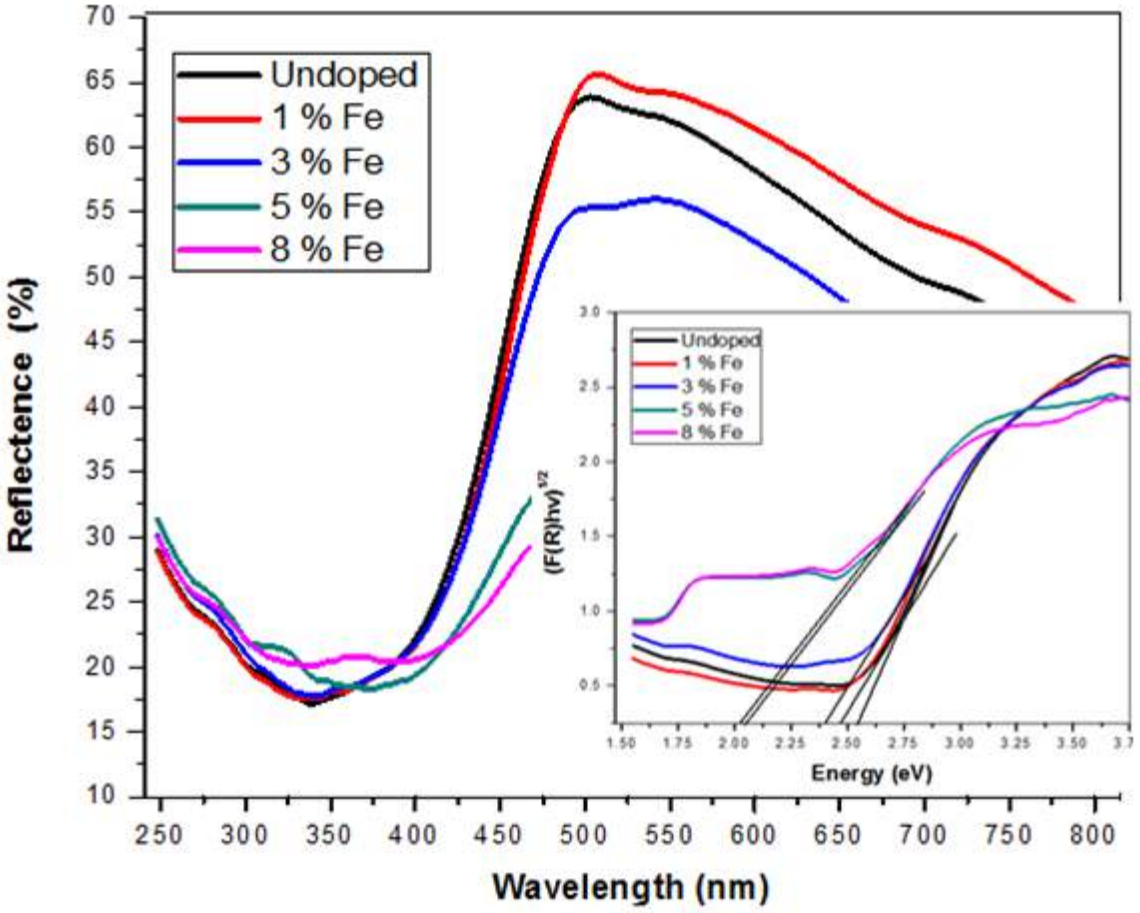

Figure 4.7: DRS spectra of the prepared nanoplates (Inset of the figure depicts the plot for band gap energy calculation)

Figure 4.8 describes the photoluminescence properties. The peak found at 414 nm is belongs to near band edge emission (NBE). The other wider and high intensity peak observed at 533 nm is usually linked to the defects. Similar results have also been reported for undoped and metal doped WO_3 nanoparticles [108, 145]. The particle morphology and size can take part in the variation of PL intensities of prepared samples [149-151].

The NBE and defects peaks intensities significantly decrease with Fe doping as a consequence of large number of defect densities.

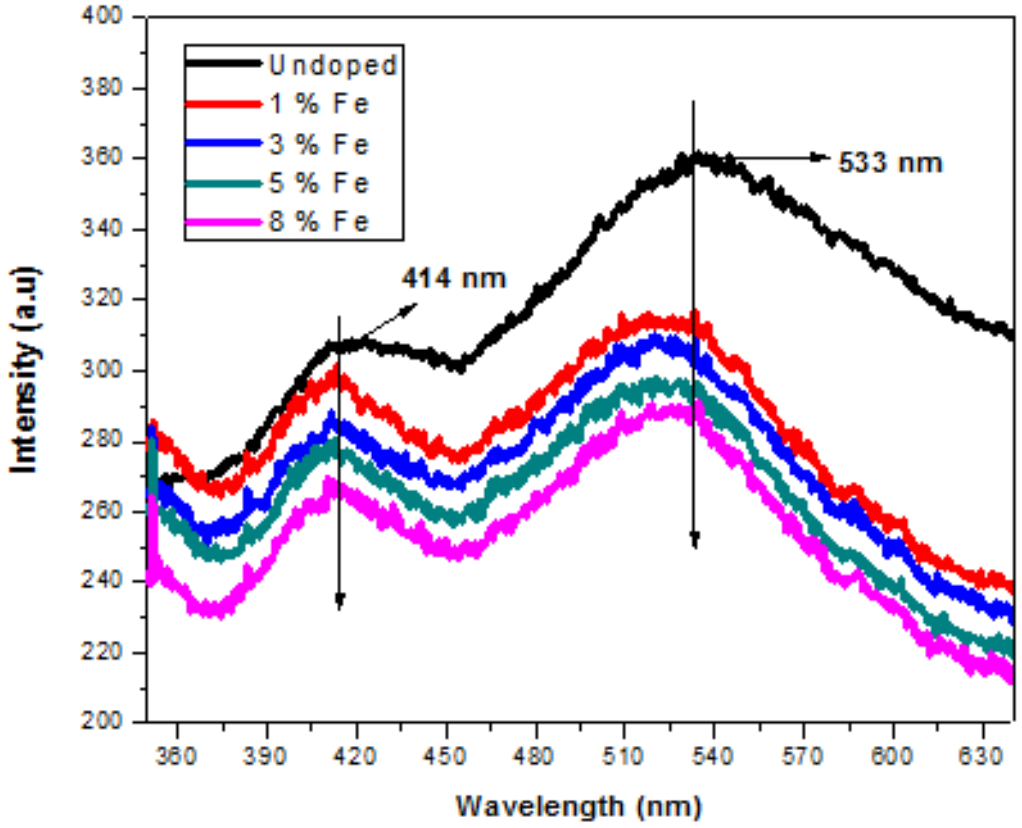

Figure 4.8 PL spectra of nanoplates.

4.2.5 Dielectric and Electrical Studies

The synthesized nanoplates were pressed into pellets using a hydraulic presser and sintered at 180 °C in an electric oven for 2 hours. The dielectric constant (ε') was measured using the equation [152].

$$\varepsilon' = (t \times C_p) / (A \times \varepsilon_o) \qquad (4.3)$$

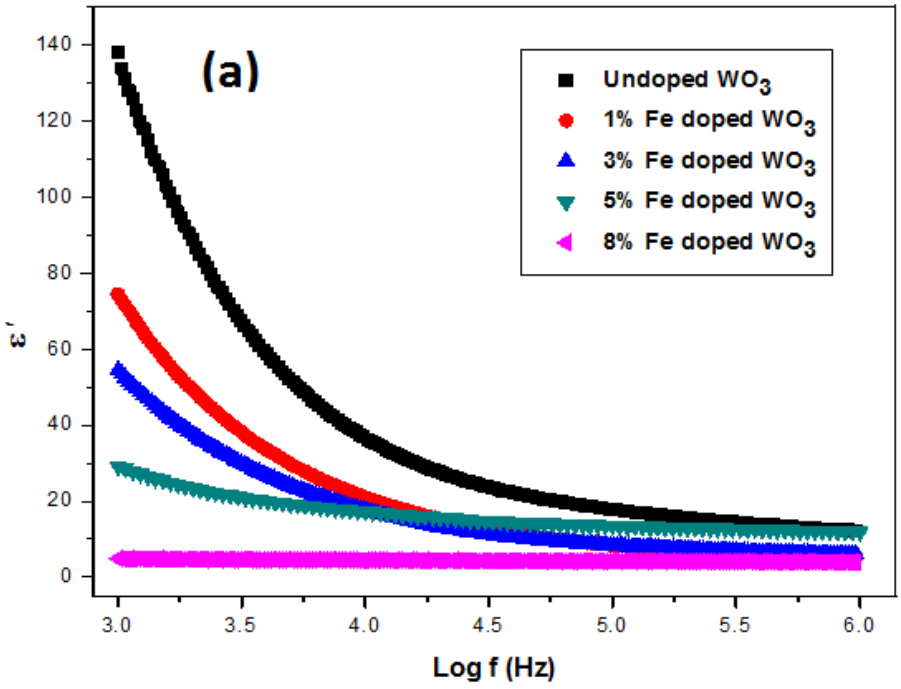

Figure 4.9 (a) dielectric constant (ε')

Where ε_o is permittivity of vacuum, C_p is the equivalent parallel capacitance, t is thickness of the pellets, A is the area of the pellets. The dielectric constants curves for undoped and Fe doped WO_3 nanostructures are shown in Figure 4.9 (a). At lower frequencies, a relatively larger value of the dielectric constant has been observed. However increase in frequency lead to a significant decrease in the value of dielectric constant for all samples. These results are in well accordance with Maxwell–Wagner dielectric model [153]. The space charge polarization phenomenon and defects may also influence the dielectric constant [154].

The dielectric constant is sensitive to the polarizability of the material which is directly linked with the electronegativity (EN) differences between the Fe and W atoms (like EN for Fe (1.83) and W (2.36) [152]. The Fe doped samples have greater electronegativity difference and have stronger bonding energies between Fe and O atoms and cannot be easily polarized with AC frequency, as a consequence the gradual decrease in dielectric constant occurs with 1% to 8% Fe

doping [152]. Furthermore, it is reported that the dielectric constant has direct relation with the particle and grain size of doped metal oxides nanostructures [155]. As evident from the FESEM images (Figure 4.2), the size of nanoplates decreases with increasing Fe concentration. A smaller particle size means a higher density of grain/particle boundaries and, consequently, the dielectric constant is lowered.

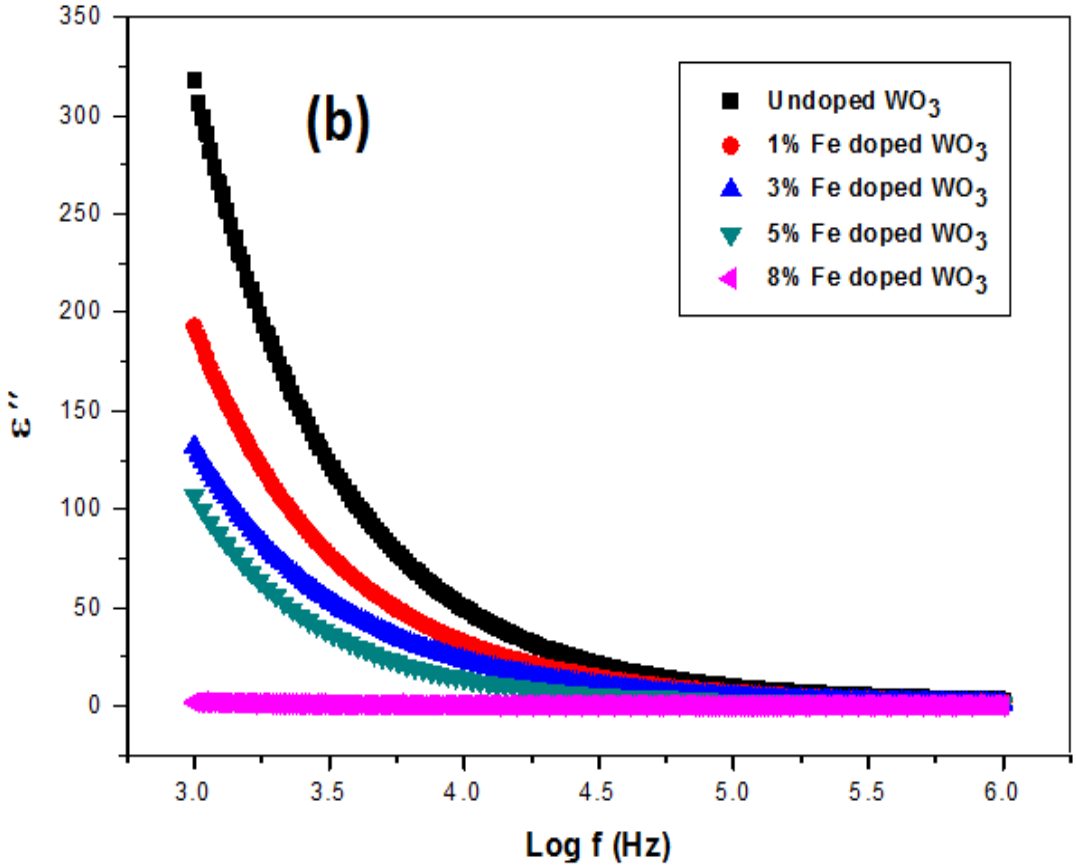

Figure 4.9 (b) dielectric loss (ε'')

The imaginary part of the dielectric constant (ε'), which represents the dielectric loss or dissipation of energy in dielectric materials, is shown in Figure 4.9 (b). The dielectric loss is calculated using the equation [152].

$$\varepsilon'' = \varepsilon' \tan\delta \qquad (4.4)$$

A higher value dielectric loss has been found at lower frequencies. Furthermore, it decreases with the increase in frequency, like dielectric constant. The higher value of dielectric loss at lower frequencies can be understood by Koop's model [156]. According to this model, the high resistivity (due to grain boundaries) is observed at lower frequency region as a results it requires more energy for electron exchange between W^{6+}, W^{5+} and Fe^{3+} ions. The significant decrease in dielectric loss at lower frequency is also observed with Fe doping which may be due to the decrease in polarization. The decrease in dielectric loss with Fe doping at lower frequency can be useful in high frequency based electronic devices applications

In order to see the effect of Fe doping on the conductivity (σ_{ac}) of WO_3 nanoplates, the frequency dependent AC conductivity of all samples was calculated using the following equation;

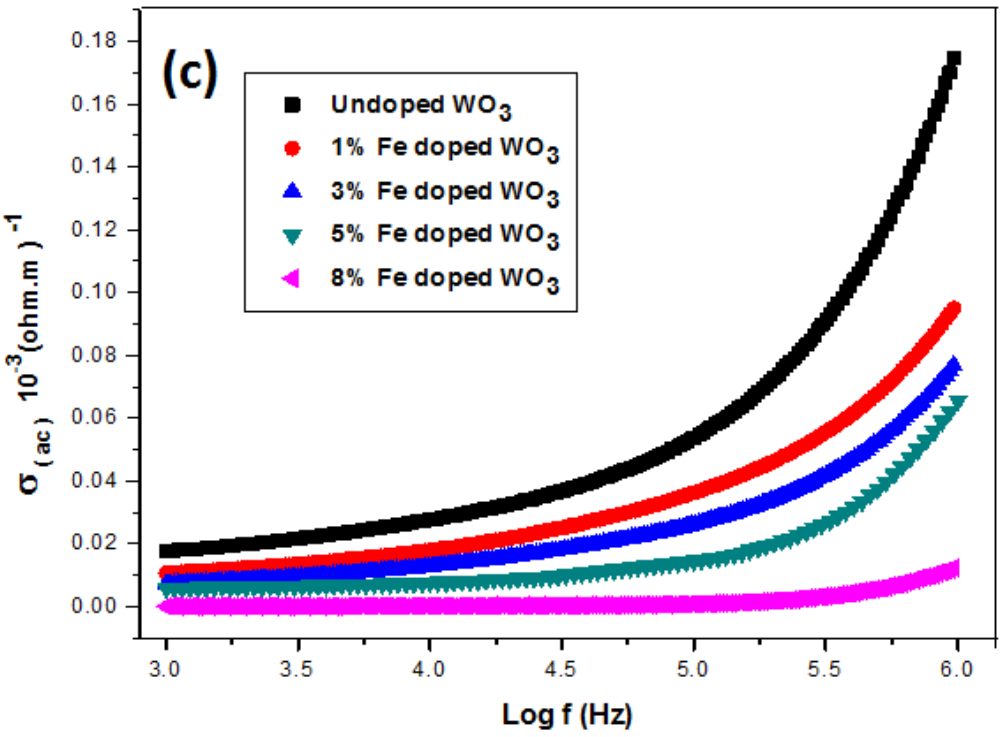

Figure 4.9(c) AC conductivity (σ_{ac}).

$$\sigma_{ac} = 2\pi f \varepsilon_o \varepsilon' \tan\delta \quad (4.5)$$

Figure 4.9(c) depicts the AC conductivity of undoped and Fe doped samples of WO_3 at room temperature. The power law is well consistent with these findings of conductivity (σ_{ac}). The conductivity has shown a significant decrease with Fe doping [157]. This decrease in the AC conductivity is due the occupation of tiny amorphous cluster of Fe ions may be reside at grain boundaries can creates electrical barriers and more scattering of the charge carriers [158].

4.2.6 Visible light driven degradation of methyl red (MR) using undoped and Fe doped WO_3 nanoplates

Photocatalytic advanced oxidation process is proved to be an environmentally friendly technology for water pollutant degradation [146]. Figure 4.10(a) depicts that undoped WO_3 nanoplates have degraded almost 67% of methyl red in two hours. With Fe doping, the photo degradation of MR with WO_3 nanoplates has been systematically increased up to 94% which depicts the Fe doping dependent activity as shown in figure 4.10 (b-d). Here a question arises that why photocatalytic degradation of methyl red by WO_3 nanoplates enhances with Fe doping. The photocatalytic degradation of organic dyes by semiconductor photocatalyst occurs in three steps. First, absorption of light takes place by semiconductor which leads to photo-generation of electron-hole pairs. As undoped WO_3 nanoplates can be activated only by blue or UV region of solar spectrum, therefore the narrowing of optical band gap will result in increase in the electron-hole pair generation. This means that more and more electron-hole pairs will be available for reactions involved in photocatalytic degradation of methyl red.

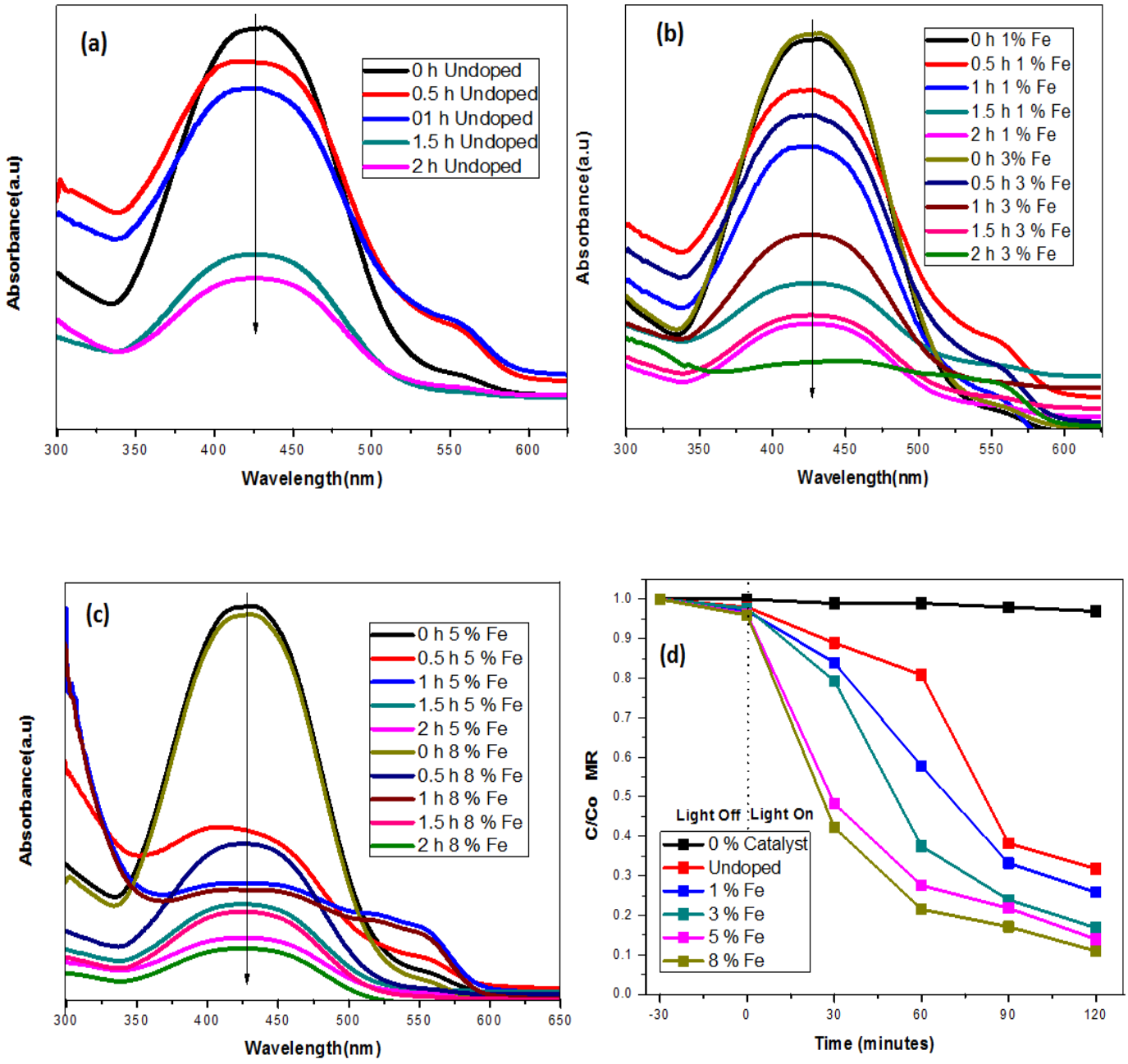

Figure 4.10 (a) Photodegradation of methyl red under visible light illumination by undoped WO_3 nanoplates **(b, c)** Photodegradation of methyl red under visible light irradiation using Fe doped WO_3 nanoplates **(d)** C/C_o versus time plot for the visible light driven photodegradation of methyl red (MR) using undoped and Fe doped WO_3 nanoplates.

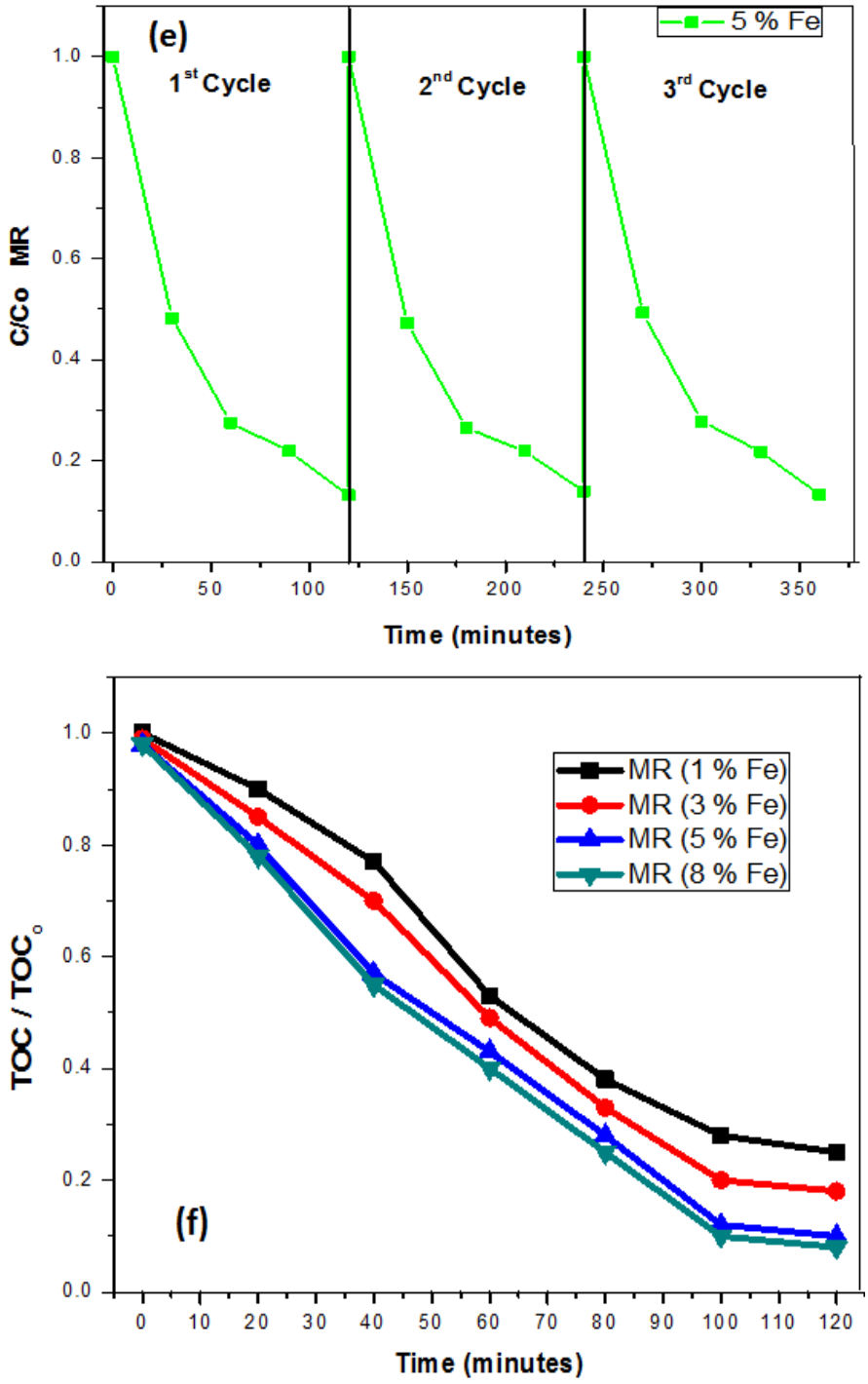

Figure 4.10 (e) The recyclability performance of 5% Fe doped WO_3 nanoplates. **(f)** Total organic carbon (TOC) removal from MR solutions during photocatalytic degradation by Fe doped WO_3 nanoplates.

As energy band gap of WO_3 nanoplates has been reduced from 2.54 eV down to 2.02 eV. Hence, this could be the one reason for higher degradation of methyl red by Fe doped WO_3 nanoplates as compared to undoped WO_3 nanoplates.

Secondly, the defects act as the trapping centers for photo-generated electrons and reduce the electron hole pair recombination rate in oxide based semiconductors like WO_3, ZnO, Fe_2O_3 and TiO_2 [159]. In our case, it has been observed from PL results that Fe doping leads to higher densities of crystal defects in WO_3 nanoplates. This may be the second possible reason for higher degradation of methyl red by Fe doped WO_3 nanoplates.

Thirdly, these photo-generated charge carriers reacts oxygen and water molecules or hydroxyl groups adsorbed on the surface of the photocatalyst and produce ·OH radicals and radical anions [146]. These produced ·OH radicals and radical anions act as oxidizing species for oxidation of methyl red and degrade it to intermediates. Furthermore, the ·OH radicals react with the intermediates resulting into CO_2 and H_2O as final products [146, 159]. The photocatalytic degradation ability of the prepared undoped WO_3 nanoplates is 70%, which is higher than the previously reported activity for some other metal oxides such as ZnO nanoparticles (28%), SiO_2 nanoparticles (46%) and TiO_2 (68%) but lower than CuO nanosheets (75%) [160-163].

Figure 4.10 (e) reveals the recyclability performance of 5% Fe doped WO_3 nanoplates. In order to further demonstrate photocatalytic characteristics of the Fe doped WO_3 nanoplates, total organic carbon content (TOC) analysis has been performed. It can be seen from Figure 4.10 (f), that TOC gradually decreases with exposure time which hints the removal of organic carbon content when methyl red was treated with prepared nanoplates. The removal of TOC reached to 94% when methyl red was treated with Fe doped WO_3 nanoplates after two hours [164].

4.2.7 Anticancer activities

The anticancer activities against MCF-7 and Hep-2 cancer cells were measured using MTT assay treated with 25μg/ml of undoped and Fe doped WO_3 nanoplates water suspensions under LED light.

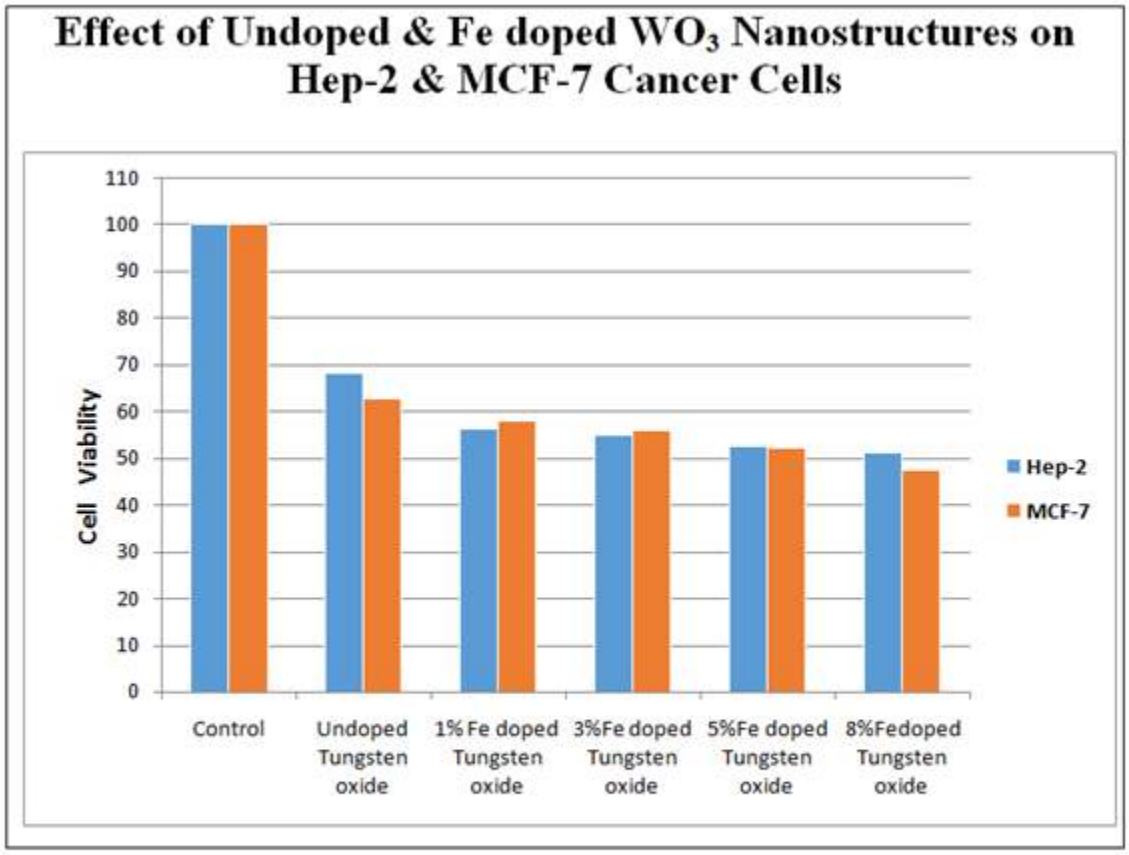

Figure 4.11 Effect of undoped and Fe doped WO_3 nanoplates on Hep-2 and MCF-7 cancer cells viability

The percent cell viability of MCF-7 and Hep-2 cancerous cells decreases up to 62% and 67% respectively with undoped WO_3 nanoplates as compared with the untreated control samples, have been shown in Figure 4.11. The 8% Fe doped samples further decrease Hep-2 and MCF-7 cancer cells viability up to 51% and 47% respectively. Importantly, the decrease in percent cell viability of MCF-7 cancerous cells in this report is better than our previous report for similar

concentrations. Previously, it has been reported that the anticancer activity mechanism of Hep-2 and MCF-7 cancer cells when treated with metal oxide nanoparticles [28]. There are number of mechanisms proposed for the anticancer characteristics of metal oxide nanomaterials such as accumulation of nanoparticles inside the cells, electrostatic rupturing of cell wall and excessive oxidative stress due to production of reactive oxygen species [28, 33, 34]. The nanomaterials exposed redox active mitochondria and these are considered to be the key site for ROS production in cells [39, 40]. The increase in ROS generation via Fe doping into WO_3 nanoplates becomes a cause to decrease percent cell viability of both cancerous cells.

This may become a cause to higher electron-hole pairs generations and ultimately results in higher ROS generation, which can play role in apoptosis of cells through oxidative damage intercellular proteins and DNA [165].

CHAPTER 5

SYNTHESIS, CHARACTERIZATIONS, PHOTOCATALYTIC AND ANTICANCER ACTIVITIES OF Sn DOPED WO_3 NANOSTRUCTURES

5.1 Introduction

Tungsten oxide (WO_3) nanostructures are an efficient choice for several applications [166-168]. It is a promising n-type $5d^0$ transition metal oxide semiconductor t [92]. Furthermore, it has good Hall mobility and long diffusion length which makes it suitable for applications such as optoelectronics devices, photocatalysis and antibacterial activities [169-175]. However, it has been reported that photo-conversion efficiency of undoped WO_3 nanostructures is low due to its low conduction band level [168]. The properties of WO_3 nanostructures are very sensitive to their size, morphology, type and concentration of dopants. For example, the reduction particle size becomes a cause to enhance surface area and diffusion length is reduced, which is advantageous for photodynamic activities [137, 139, 176].

Metal doping could be very effective in tailoring the free charge carriers, reduction potential and conduction band level because of the introduction of impurity levels, which would enhance the photodynamic anticancer activity of WO_3 nanostructures [177-180]. For example, Ti doping of WO_3 successfully enhanced the carrier density, and conduction band edge was shifted up which led to an increase in photo-response [87]. Song et al., reported tuning of band gap and an enhanced photocatalytic activity of WO_3 nanostructures with Fe doping [146]. Sn may be an ideal cationic dopant for WO_3 nanostructures because of its similar atomic radius compared to

W. It has been reported that Sn doping of WO_3 lattice leads to a higher visible light driven photocatalytic response [145]. This chapter seems to suggest that Sn doping may also be beneficial for enhancing the optical, electrical, photodynamic anticancer and photocatalytic activities of WO_3 nanostructures [145].

5.2 Results and discussion

5.2.1 X-ray diffraction and scanning electron microscope studies

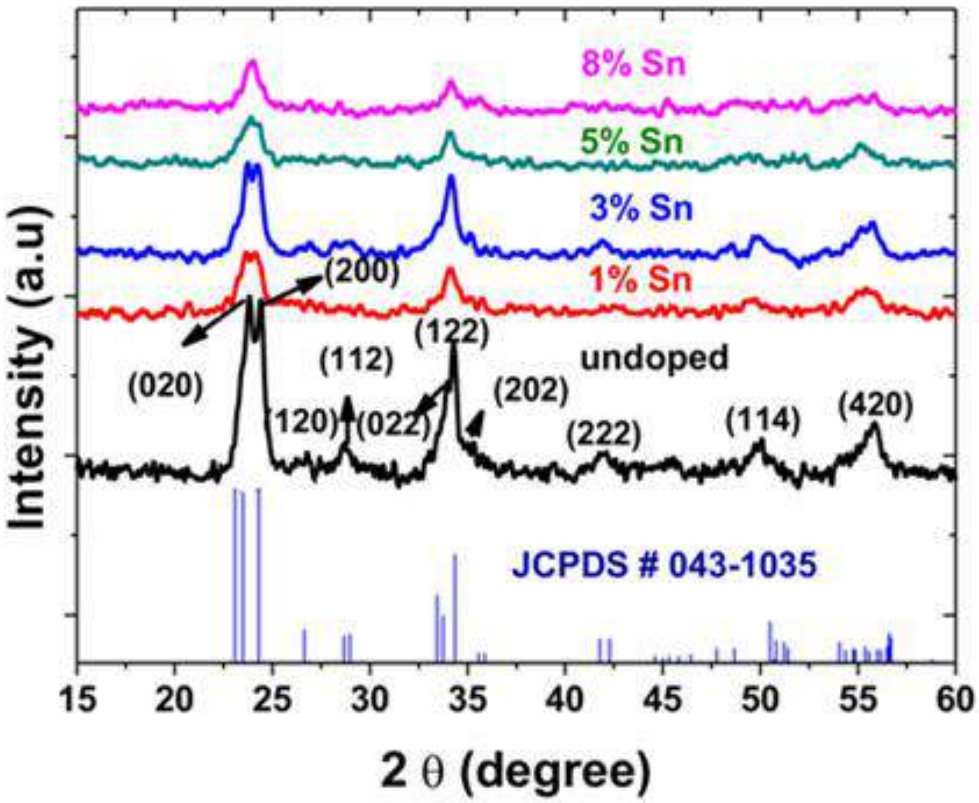

Figure 5.1 XRD patterns of undoped and Sn doped WO_3 nanostructures.

All samples have shown broad diffraction peaks, which indicate their nanocrystalline nature. In Figure 5.1, the phase purity of the Sn doped WO_3 samples were verified by the nonexistence of Sn related peaks. A sharp doublet diffraction peak corresponding to (020) and (200) planes was observed for undoped WO_3 samples which gradually changes into a singlet peak [145]. The lack of Sn related XRD peaks and suppression of the doublet peak into a singlet peak demonstrates successful doping and formation of the single phase Sn-W finite solid solution [181]. This change is probably associated with the variation in ionic radii of W^{6+} (0.062 nm) and Sn^{4+} (0.069 nm) ions [182].

Figure 5.2 (a-e) depicts the SEM images of the samples. As evident from the SEM images, all samples have plate-like morphology. However, there is a slight variation in the size and shape of nanoplates with Sn doping. For high concentrations of Sn, there is a significant amount of spherical nanoparticles in the final yield (Figure 5.2d, e) [92]. However, there is a slight variation in the size and shape of nanoplates with Sn doping. For high concentrations of Sn, there is a significant amount of morphological changes.

As evident from Figure 5.3, a slight Sn peak appears in the EDX spectra for doped samples. The peak is absent in undoped sample.

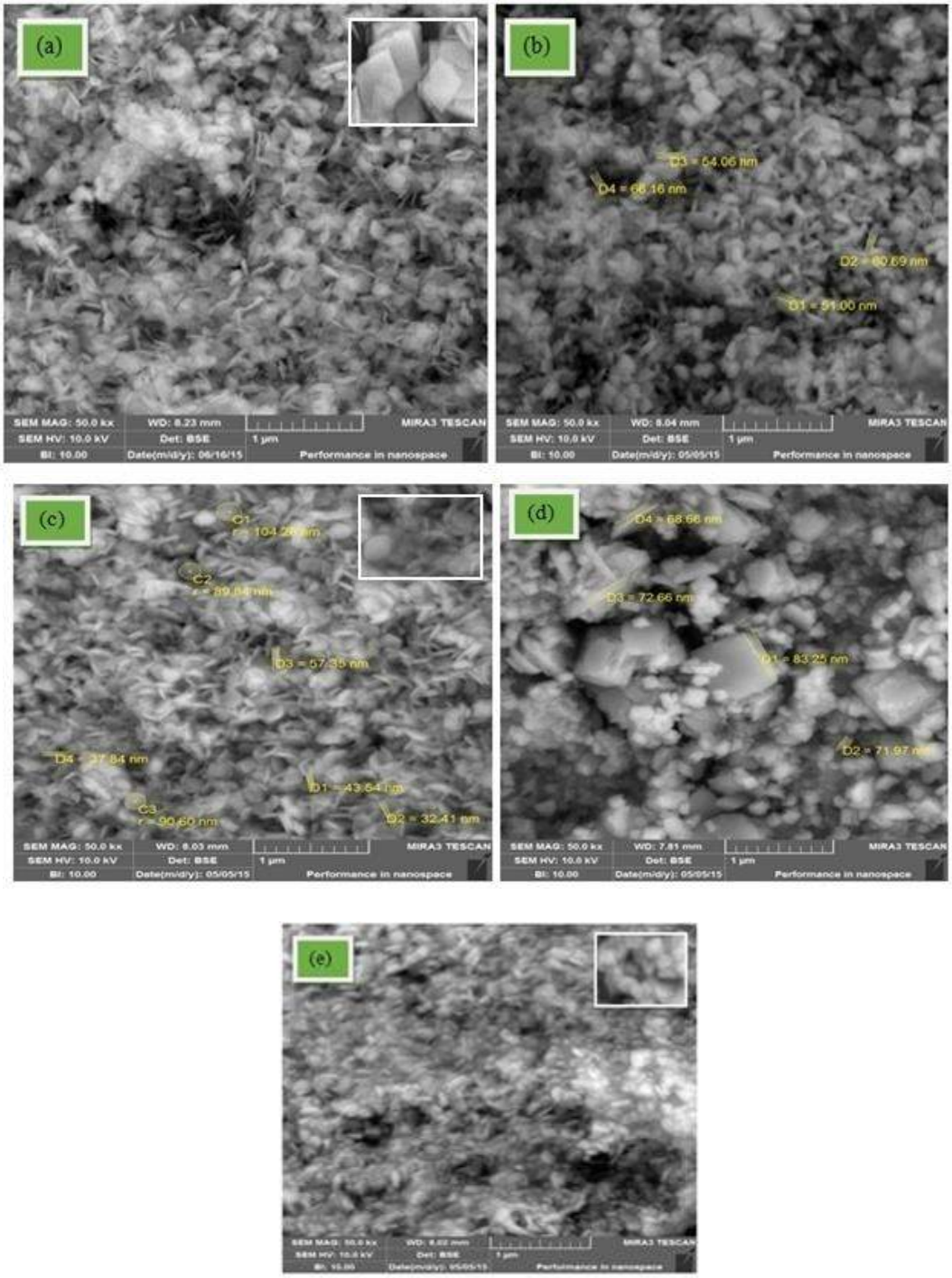

Figure 5.2 SEM images of (a) undoped (b) 1% (c) 3% (d) 5% and (e) 8% Sn doped WO_3 nanostructures.

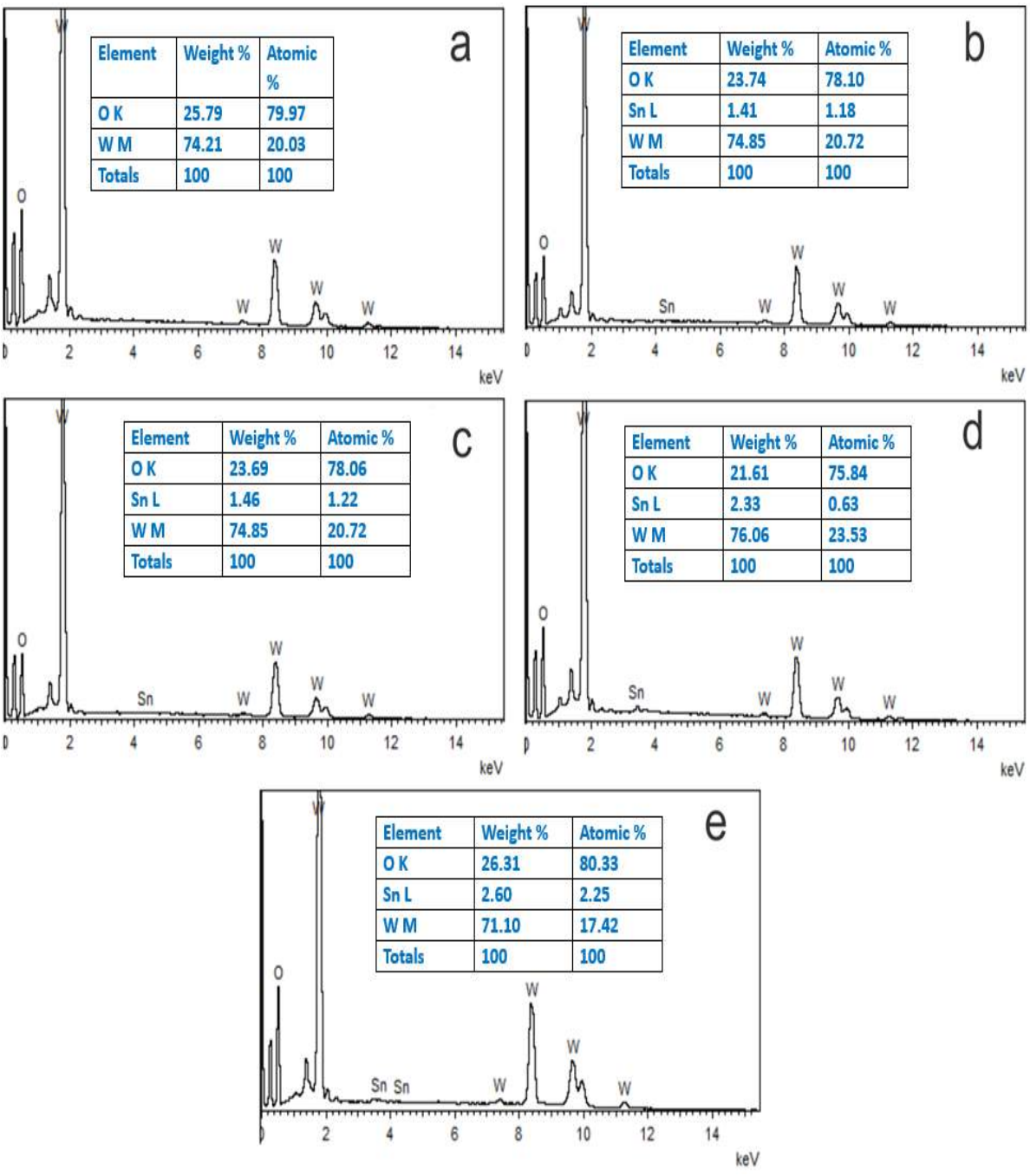

Figure 5.3 EDX spectra of (a) undoped, (b) 1% (c) 3%, (d) 5% and (e) 8% Sn doped WO_3 nanoplates.

5.2.2 FTIR and Raman spectroscopic studies

Figure 5.4 depicts the FTIR spectra of the samples. The band found at 550 to 1050 cm^{-1} is links to the stretching vibration of O-W-O [66]. The other observed vibration modes at 1415cm^{-1} and 1628 cm^{-1} belong to the tungsten-hydroxyl (W–OH) bond but the intensities of these absorption bands are very low which suggest the presence of very minute hydration of the prepared nanostructures. The stretching vibrational mode of O−H groups in H_2O or hydroxyls has been found at 3300-3600 cm^{-1} [142]. Hence, FTIR results again confirm the monoclinic formation of WO_3 structure in all samples with doping.

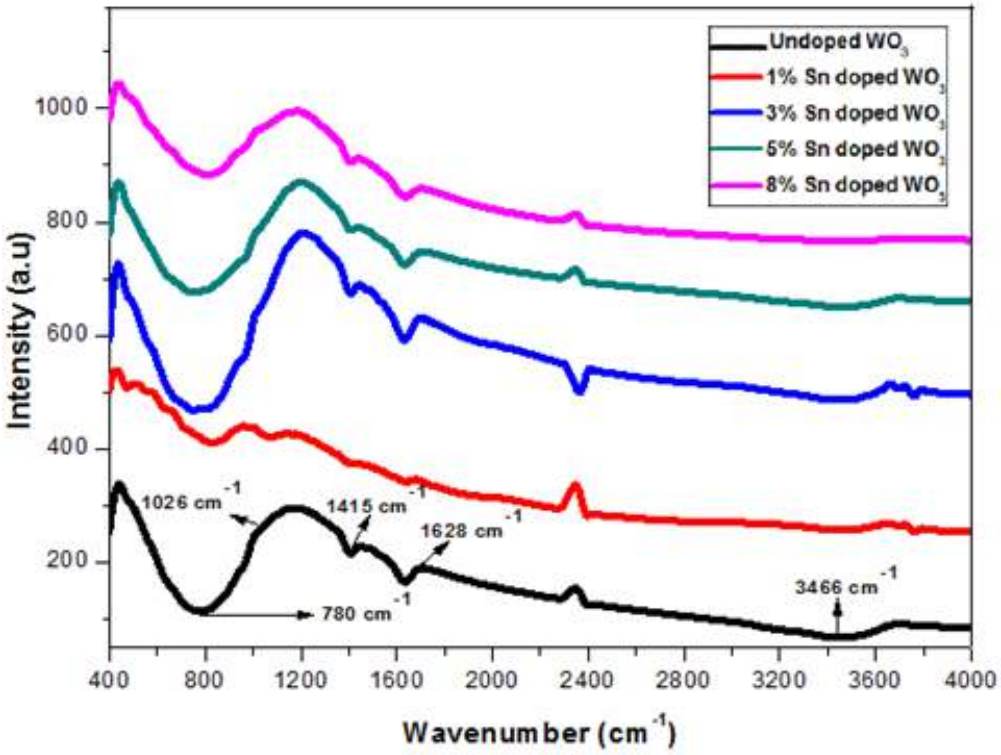

Figure 5.4 Synthesized nanoplates FTIR spectra.

The microstructural properties and the possibility of the presence of any secondary phases were further studied by Raman spectroscopy. The Raman spectra of undoped and Sn doped WO_3 nanoplates are shown in Figure 5.5. The stretching vibrational modes υ (O–W–O) are found at 700 and 802 cm^{-1} and bending vibrational modes δ(O–W–O) are observed at 251 and 319 cm^{-1}. Our results are consistent with previously reported results for WO_3 [143]. The absences of bands related to SnO_2 or any other impurity associated bands in Raman spectra verify successful Sn doping.

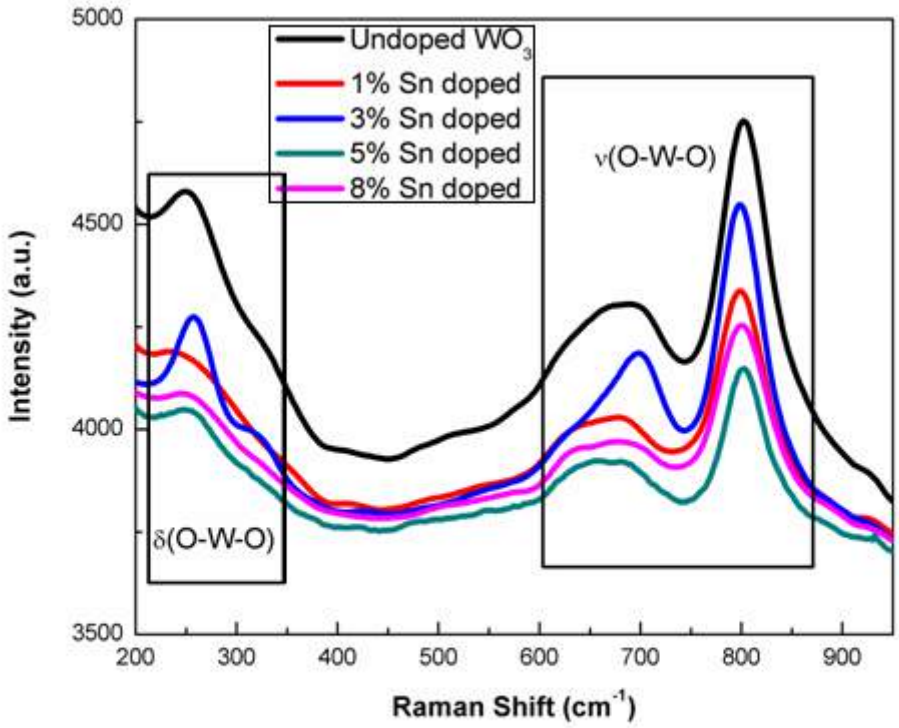

Figure 5.5 Raman spectra of WO_3 nanoplates doped with varying amounts of Sn.

The peak positions of υ (O–W–O) stretching vibrational bands are slightly shifted towards lower wave numbers. Furthermore, the peak intensities are suppressed with the increase in Sn doping concentration. In our case, Sn doping has affected crystallite size, and particle size and shape as observed by XRD analysis and SEM images.

5.2.3 Photoluminescence spectroscopic analysis

In Figure 5.6, the photoluminescence (PL) measurements of undoped and Sn doped WO_3 nanoplates were performed. The PL spectra show two distinct peaks centered at 421 nm (blue emission, NBE peak) and 540 nm (green emission, defects peak) [183, 184].

The green emission intensities are positively correlated with the defect densities and average particle size [150, 151]. These defects mediated visible luminescence may play a vital role in tuning the frequency dependent dielectrics characteristics and enhance the photodynamic anticancer activity of WO_3 nanoplates.

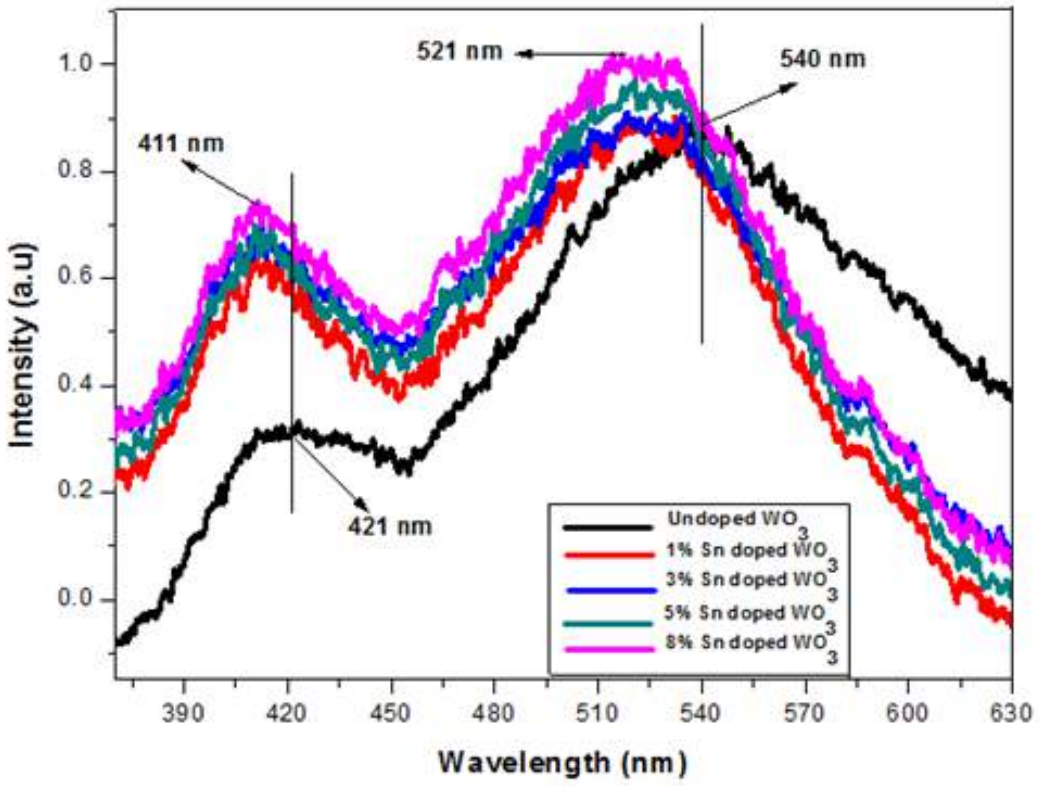

Figure 5.6 PL spectra of undoped and Sn doped WO_3 nanostructures.

5.2.4 Dielectric and electrical analysis

The frequency dependent dielectric behavior of undoped and Sn doped WO_3 nanoplates were investigated between 1 kHz to 1MHz AC frequency range. The dielectric constant (ε') was measured by using the equation 4.3 [152].

Figure 5.7 depicts the behavior of dielectric constant of undoped and Sn doped WO_3 nanoplates. These results are consistent with Maxwell–Wagner dielectric model [153].

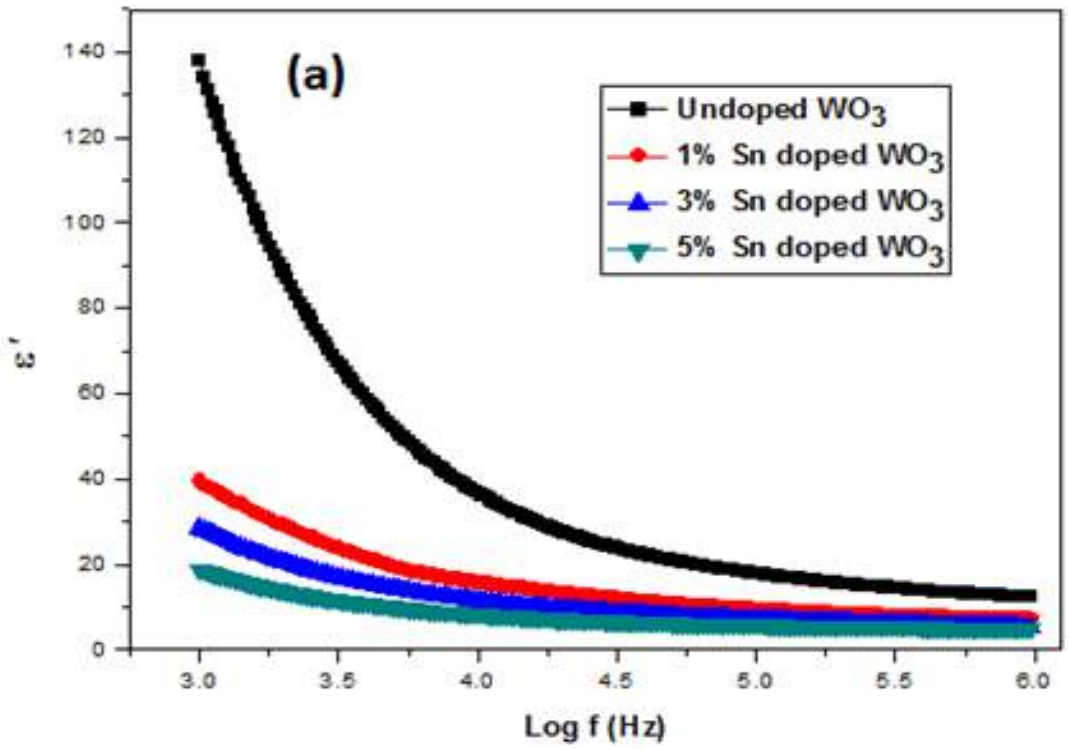

Figure 5.7 (a) dielectric constant (ε').

The Sn doping of WO_3 matrix has significantly decreased the dielectric constant. The dielectric constant depends upon the polarizability of the dielectric material, which in turn is directly linked with the electronegativity. The electronegativities of Sn and W are 1.96 and 2.36,

respectively [152]. Hence, the introduction of Sn ions may reduce the polarizability of nanoplates and cause gradual decrease in dielectric constant [152].

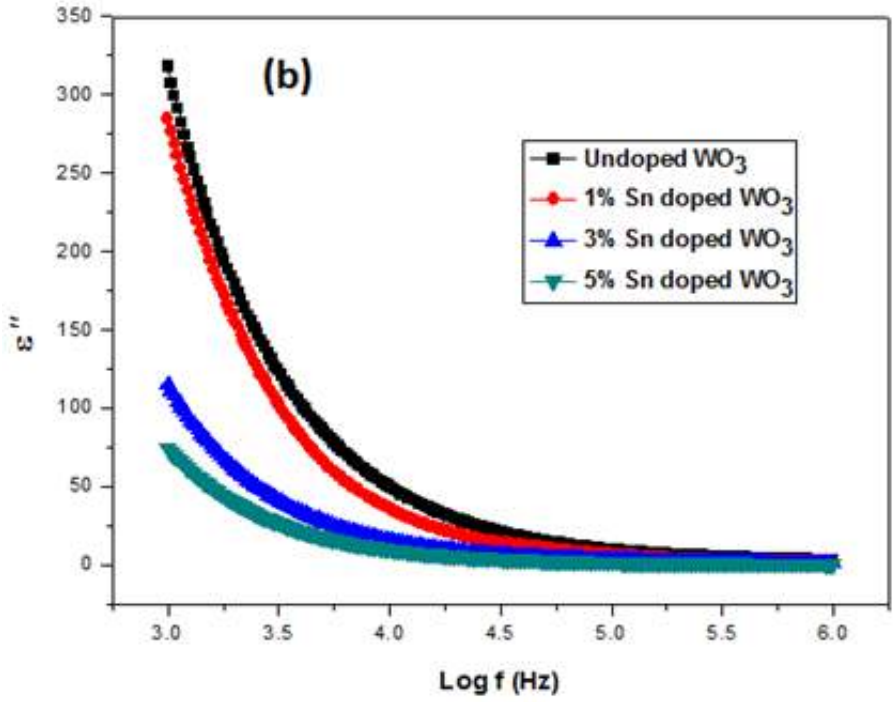

Figure 5.7 (b) dielectric loss (ε'').

The dielectric loss was calculated in Figure 5.7 (b) from experimental data via equation 4.4 [152]. The significant decrease in dielectric loss at lower frequency was observed with Sn doping due to the reduced electric polarization. This makes Sn doped WO_3 nanostructures a potential candidate for application in high frequency based electronic devices.

The influence of Sn doping on AC conductivity (σ_{ac}) was determined by the equation 4.5 [152]. The frequency dependent σ_{ac} of the nanoplates is shown in Figure 5.7(c). The σ_{ac} remained almost constant at low frequency range due to grain boundaries conduction effects. It then experiences a rapid increase at a certain higher frequency range because of the grain conduction effects. These results are well consistent with power law.

The Sn doping has significantly decreased the conductivity of WO_3 nanoplates. This may be due to several factors such as oxygen vacancies, segregation of grain boundaries, and tungsten interstitials [157, 158].

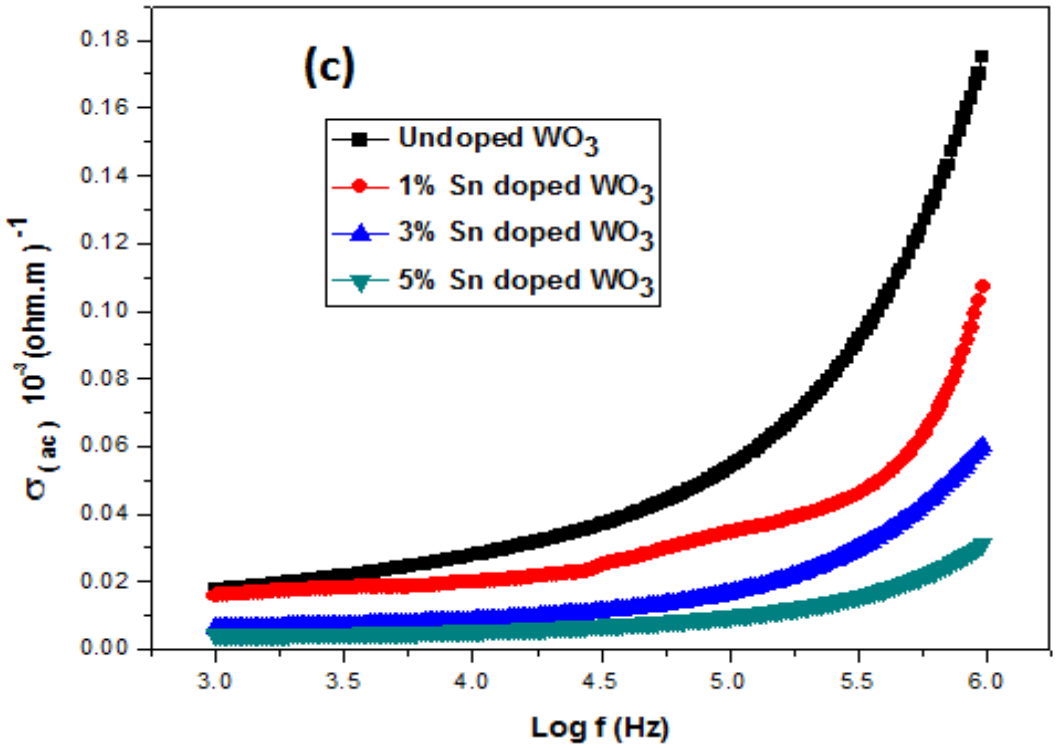

Figure 5.7(c) AC conductivity (σ_{ac})

5.2.5 Visible light driven degradation of methyl red using undoped and Sn doped WO_3 nanoplates

The photocatalytic activity of the prepared nanoplates were explored using an organic dye, methyl red, as water contaminant as shown in Figure 5.8 (a-c). The undoped WO_3 nanoplates were done degradation about 67% of MR dye under visible light irradiation in 120 minutes. The photodegradation efficiency of methyl red were further increased up to 83% in just 120 mint

with the presence of Sn doped WO_3 nanoplates under illumination of visible light. The mechanism involves in photocatalytic dye degradation were already explain in previous chapters.

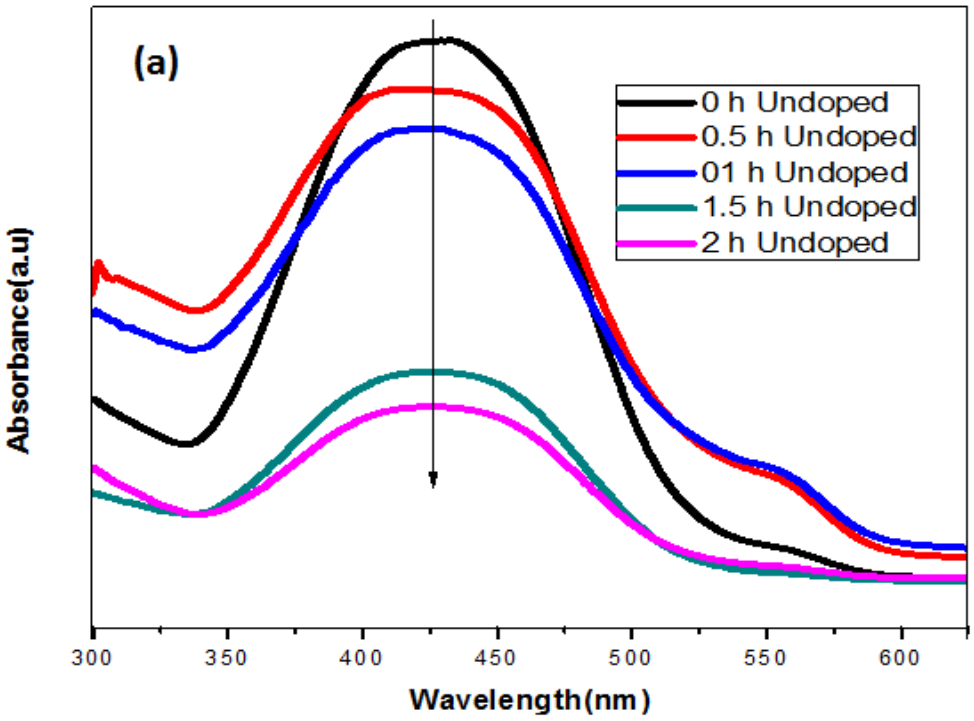

Figure 5.8 (a) Photodegradation of methyl red under visible light illumination by undoped WO_3 nanoplates

Figure 5.8 (c) also describes that methyl red does not undergo any significant degradation under visible light illumination in the lack of photocatalyst. There is one major drawback related to photocatalysis technique is its fast photoinduced electrons and holes recombination rates that reduces the photodegradation activities. With Sn doping induced defects, the separation rates of photoinduced charge carriers efficiently increases because these defects act as the active centers

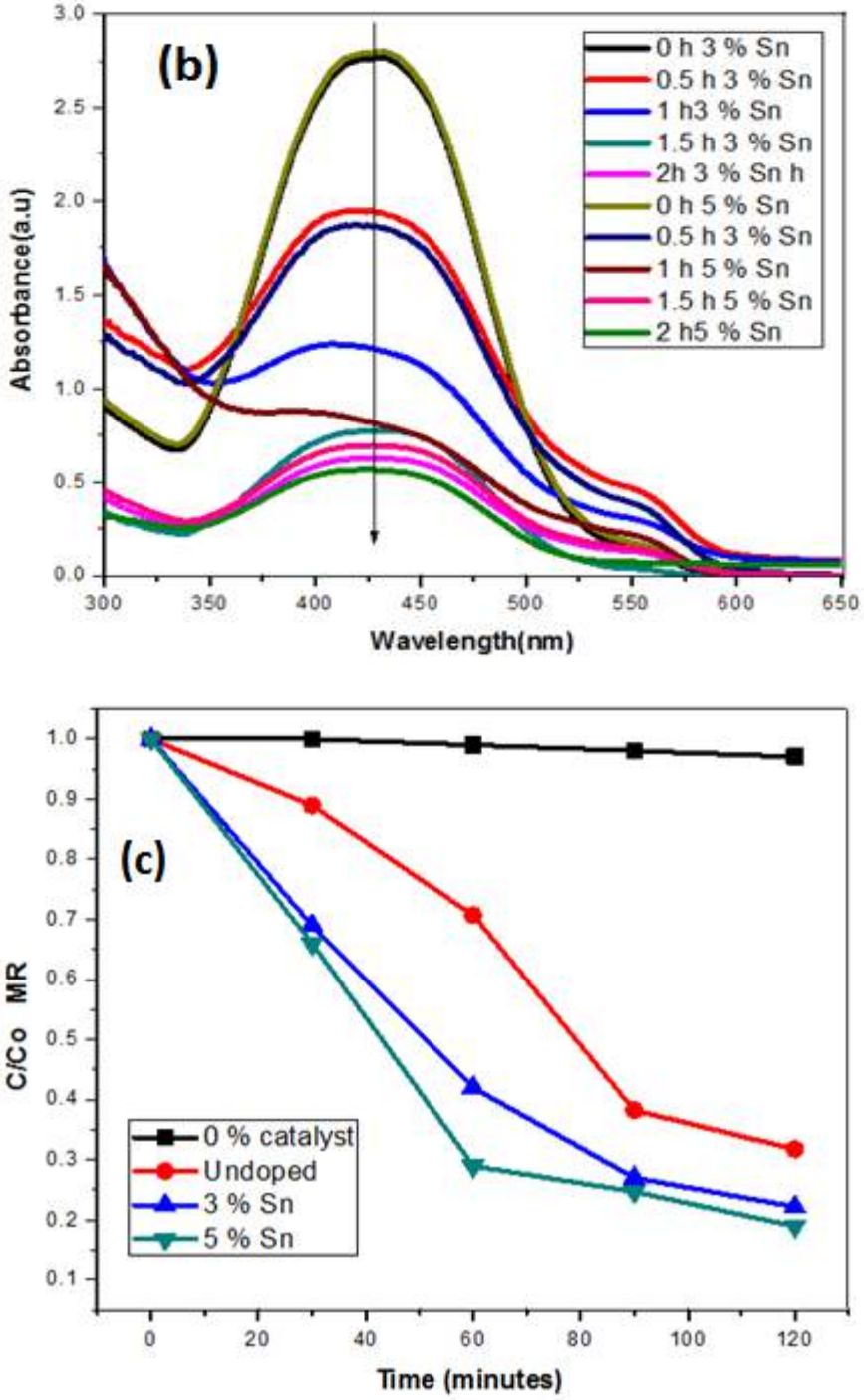

Figure 5.8 (b) Photodegradation of methyl red under visible light irradiation using Sn doped WO_3 nanoplates **(c)** C/C_o versus time plot for the visible light driven photodegradation of methyl red (MR) using undoped and Sn doped WO_3 nanoplates.

to capture photoinduced electrons and reduces the electron hole pairs recombination rates and enhanced photocatalytic activities [185].

5.2.6 Anticancer activities

The cytotoxic measurements were performed through MTT assay in LED white light using concentrated suspensions of undoped and Sn doped WO_3 nanostructures in water. Figure 5.9 depicts the cancerous cells viability treated with undoped and Sn doped WO_3 nanostructures (25μg/μL). Compared with the untreated control sample, undoped WO_3 nanoplates have reduced the cell viability of MCF-7 cancerous cells down to 73%, which is further reduced systematically with increase in Sn doping. The 8% Sn doped sample has reduced the cell viability to 56%. Interestingly, the reduction in percent cell viability of MCF-7 cancerous cells in our case is better than those reported for Fe_2O_3 and ZnO nanoparticles for similar concentrations [28, 40]. Although the mechanism for anti-cancer activity of some metal oxide nanostructures has been suggested, the exact mechanism of the interaction of WO_3 nanostructures with MCF-7 cancerous cells is unknown. For ZnO, it has been reported that initially nanoparticles may attach to the outer membrane of cancer cells due to electrostatic interaction and then penetrate into the cancer cell layer [16, 33, 34]. The nanoparticles may attack the redox active mitochondria which are considered to be the major site for ROS production in cells exposed to nanomaterials [39, 40]. Hence, nanostructures can produce ROS which may result in apoptosis in cells via oxidative damage intercellular proteins and DNA [165]. The production of ROS and oxidative stress is reported to be strongly dependent on particle size and crystal defects [165, 186, 187]. Hence, nanostructures smaller in size and having high defects densities may have the best anticancer

activity.

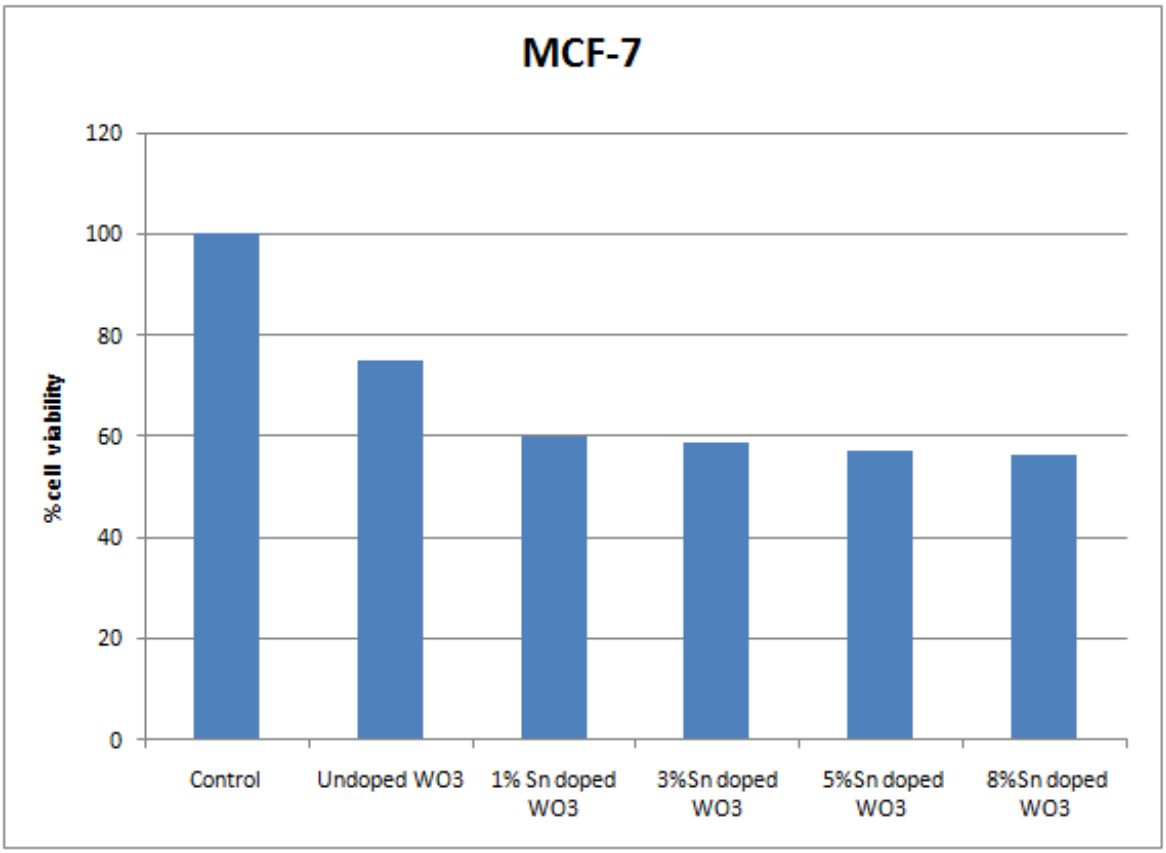

Figure 5.9: Effect of undoped and Sn doped WO_3 nanostructures on MCF-7 cells viability.

CHAPTER 6

SYNTHESIS, CHARACTERIZATIONS, PHOTOCATALYTIC AND ANTICANCER ACTIVITIES OF Cu DOPED WO_3 NANOPLATES

6.1 Introduction

Recently, the two-dimensional (2-D) nanomaterials have demonstrated diverse properties [188-190]. The 2-D morphology has an enormous impact on the properties of WO_3 nanomaterials [191-193]. The 2-D morphology of WO_3 nanostructures assists to increase the charge carrier transfer rate and enhances the specific surface area [194]. These properties clearly help to promote the photodynamic activities of WO_3 nanomaterial when they are exposed to visible light. Different morphologies of WO_3 nanomaterials have been utilized in various applications like catalysis, sensors, electrochromic displays and cytotoxic activities [97, 195-198].

Nanomaterials have shown excellent potential for cancer therapy applications due to their unique physiochemical and biological properties [199]. Among them, metal oxide nanomaterials have shown great prospects for visible light driven cancer therapy [200]. Their effective interaction with the cancerous cells under the exposure of visible light can open new ways for cancer therapy applications in future [201, 202]. However, their potential toxicity towards healthy cells reduces their effectiveness in cancer treatments [203, 204]. Therefore, new biocompatible anticancer agents must be developed.

In the present chapter, we have examined, the effects of Cu doping on the electrical and visible light responsive photocatalytic degradation properties of WO_3 nanoplates. Furthermore, the anticancer properties were also investigated with biocompatible Cu doped WO_3 nanoplates.

6.2 Results and discussion

6.2.1 X ray diffraction and scanning electron microscope studies.

In Figure 6.1, the phase purity of Cu doped WO_3 nanoplates has been validated by the nonexistence of Cu peak. This also verifies the successful incorporation of Cu ions as a

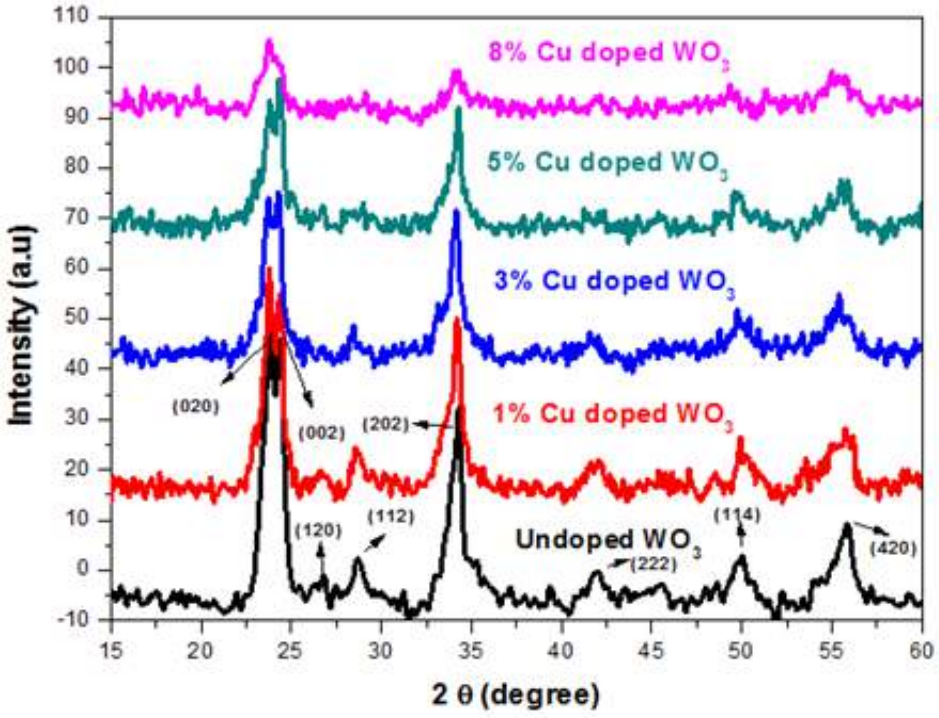

Figure 6.1 XRD patterns of undoped and Cu doped WO_3 nanoplates.

replacement for the W ions. Our results agree well with a previous report on the Cu doped WO_3 nanostructures [205]. However, the peak intensities are gradually decreased with Cu doping which is due to the reduction in crystallinity with Cu doping. By applying the Scherer's equation, the average crystallite size of 36 nm has been obtained for the undoped sample, which reduces to 22 nm for 8% Cu doped sample.

The scanning electron microscopy (SEM) images of the samples are depicted in the Figure 6.2(a-e). The 2-D square plate-like morphology is observed for all samples. The undoped WO_3 2-D nanoplates have an average thickness of about 47 nm. However, the 2-D morphology is slightly changed with Cu doping.

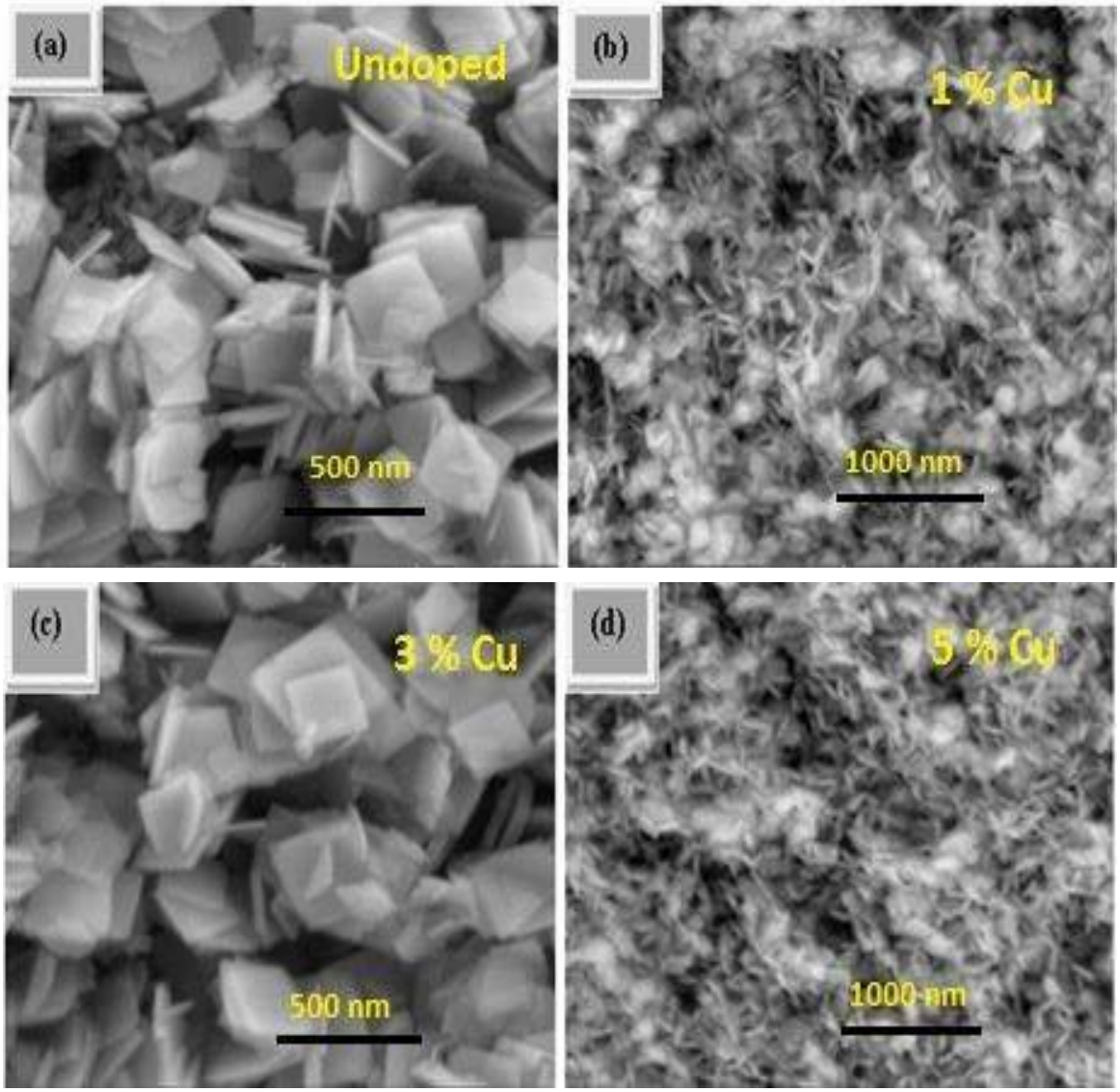

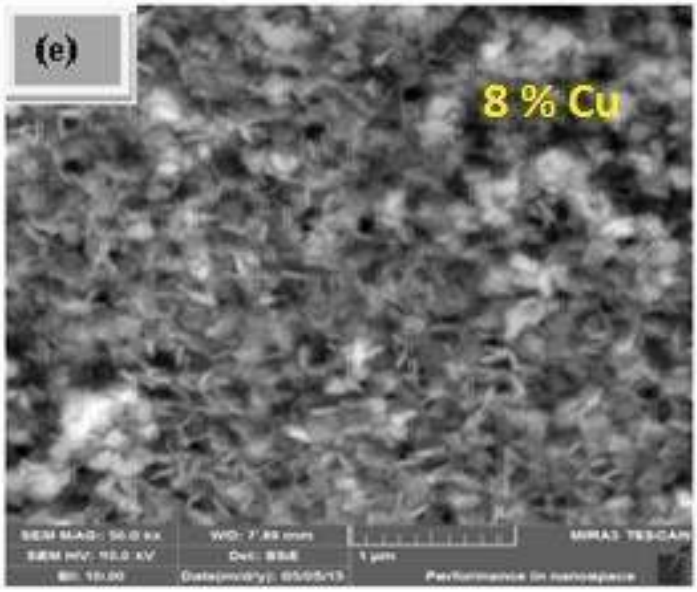

Figure 6.2 SEM images of (a) undoped (b) 1% (c) 3% (d) 5% and (e) 8% Cu doped WO_3 nanoplates.

Figures 6.3 depict the energy-dispersive X-ray spectroscopy (EDX). The presence of Cu dopant in the WO_3 host matrix is also confirmed by EDX. There are small Cu peaks for the doped samples (Figure 6.3b-e), while the undoped sample has no Cu peaks (Figure 6.3a).

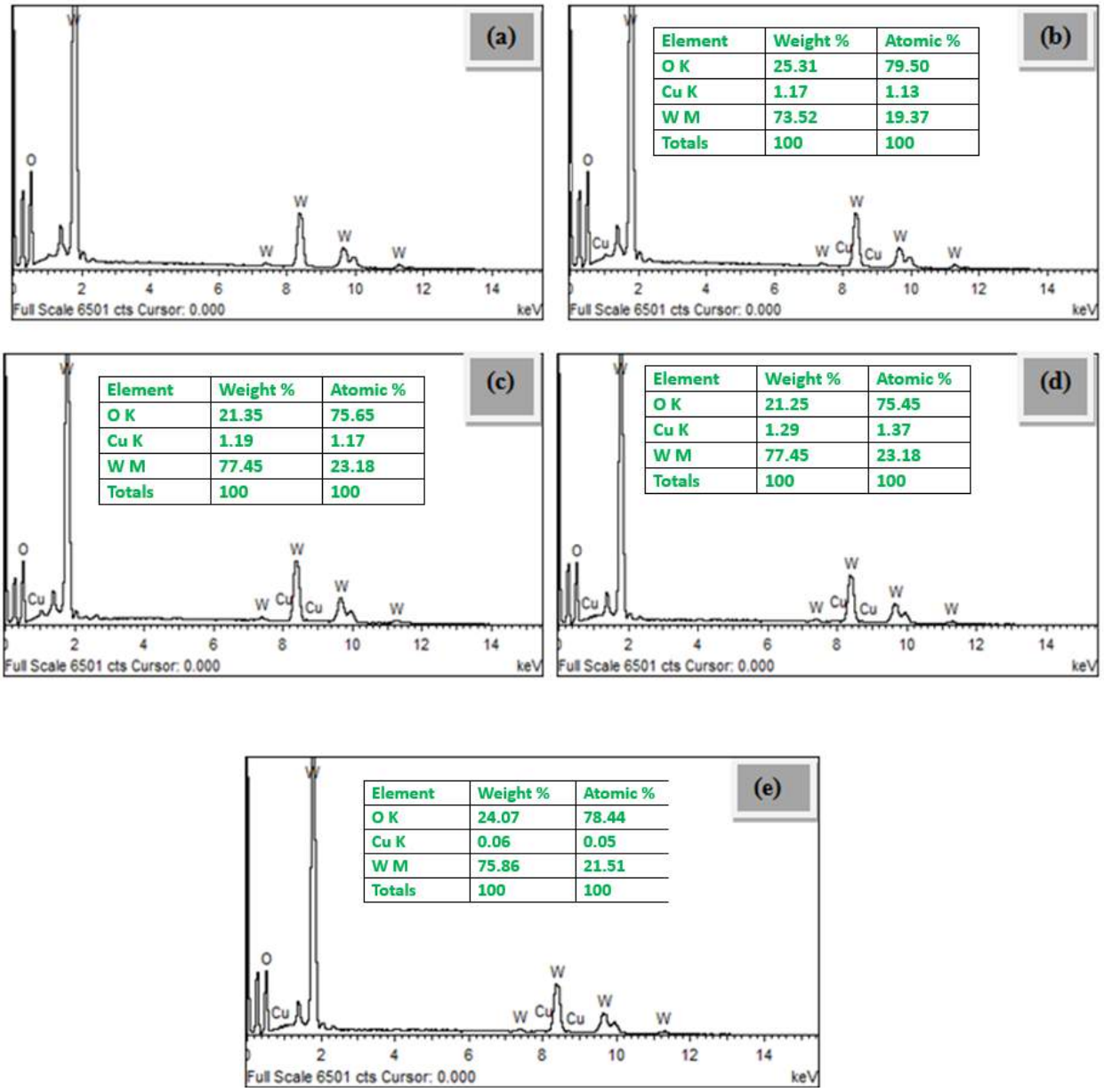

Figure 6.3 EDX spectra of (a) undoped, (b) 1% (c) 3%, (d) 5% and (e) 8% Cu doped WO_3 nanoplates.

6.2.2 FTIR and Raman spectroscopy studies

Figure 6.4 represents the FTIR spectra of undoped and Cu doped WO_3 nanoplates. The band emerged between 550 and 1050 cm^{-1} belongs to the O-W-O stretching mode while the band at

1415 cm^{-1} and 1628 cm^{-1} are linked with the bending modes of O–H groups. Another band found between 3300 and 3600 cm^{-1} is linked to the stretching modes of the O−H groups in water or hydroxyls [66].

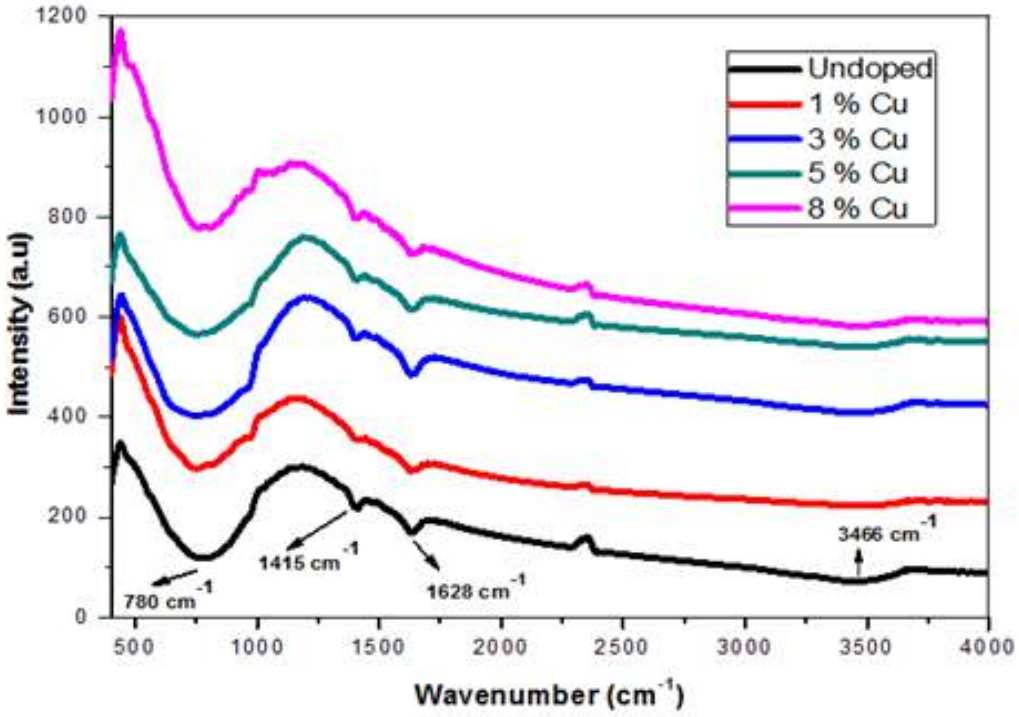

Figure 6.4 FTIR spectra of the undoped and Cu doped WO_3 nanoplates.

Figure 6.5 depicts the Raman spectra of all samples. The stretching vibrational modes υ (O–W–O) are found at 690 and 802 cm^{-1} and bending vibrational modes δ(O–W–O) are observed at 251 and 319 cm^{-1} [143].

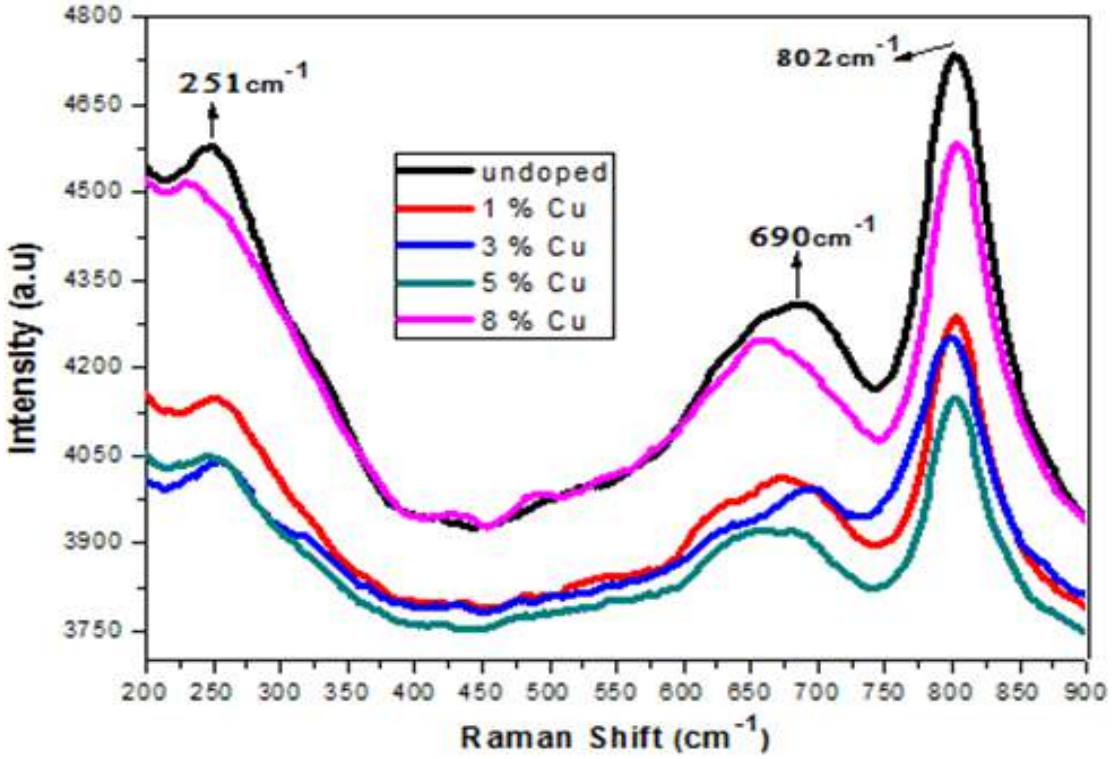

Figure 6.5 Raman spectra of undoped WO_3 and Cu doped WO_3 nanoplates

6.2.3 Optical characteristics analysis

In order to study the optical characteristics of semiconductor nanomaterials, particularly to investigate the impurity related effects, the diffuse reflectance spectroscopy (DRS) technique are usually employed and shown in Figure 6.6 [206]. The undoped WO_3 nanoplates have an energy band gap of about 2.5 eV, which is narrower as compared to that of the bulk WO_3. It further decreases due to defects down to 2.15 eV with 8% Cu doping [207]

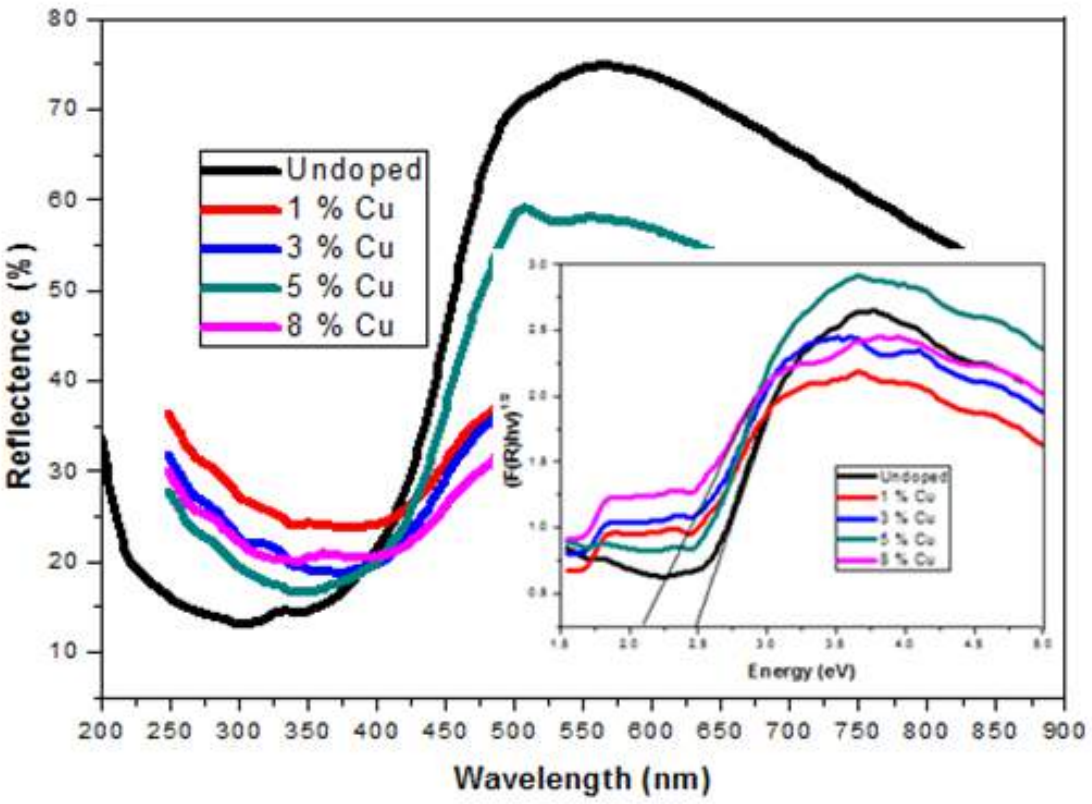

Figure 6.6 (a) DRS spectra of undoped and Cu doped WO_3 nanoplates.

The photoluminescence (PL) spectra of nanoplates have been shown in Figure 6.6 (b). In PL spectra, the peak found at 412 nm is designated as near band edge emission (NBE). The other wider and high intensity peak found at 535nm is usually because of the deep level (DL) emissions owing to the oxygen vacancies and other interstitial defects [145]. The particle morphology plays vital role in the variation of PL intensities of the prepared samples [149-151]. The Cu doping significantly increases the intensity of both NBE and the DL peaks. These defects may have direct links in the enhancement of cytotoxicity of the nanoplates.

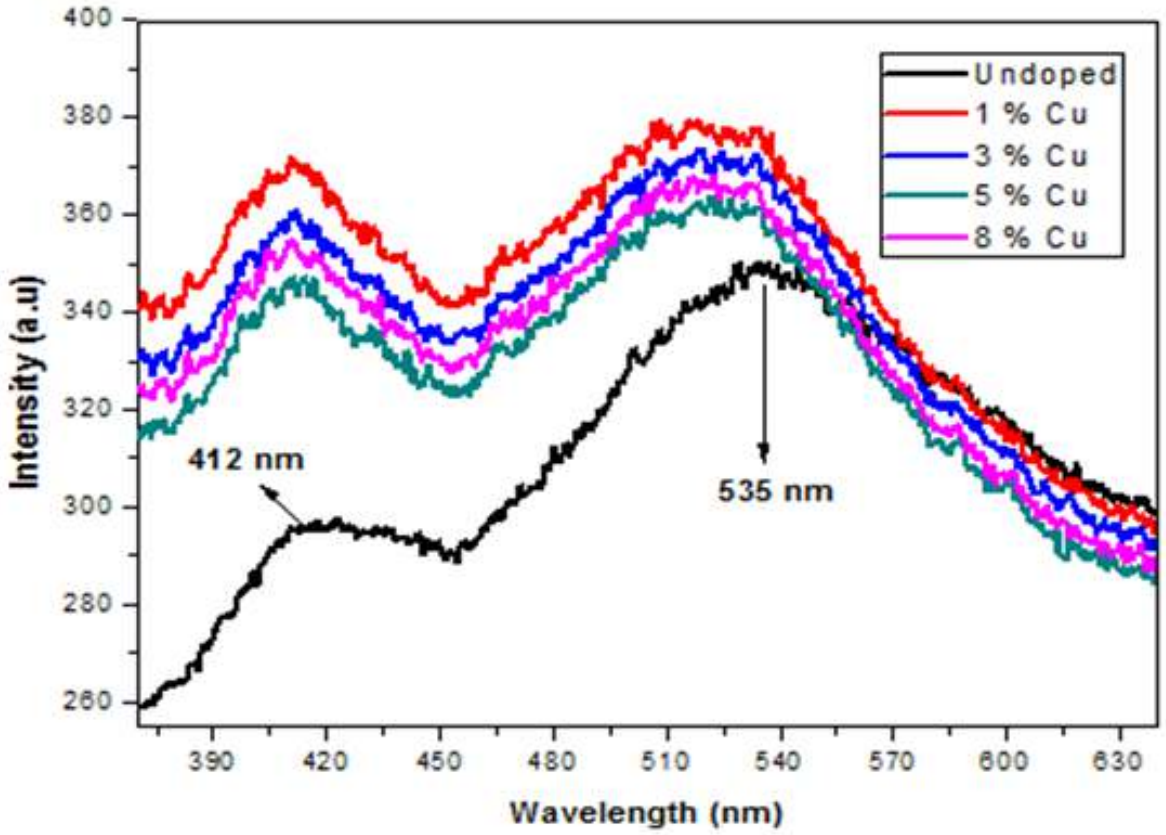

Figure 6.6 (b) PL spectra of undoped and Cu doped WO_3 nanoplates.

6.2.4 Dielectric and electrical analysis

Figure 6.7 depicts the dielectric constant (ε') was measured by using equation 4.3 [152]. These results are consistent with Maxwell–Wagner dielectric model [153]. The dielectric constant has been decreased with Cu doping. The Cu doping reduces the polarizability of material due the electronegativity differences between Cu (1.90) and W (2.36) and also slight variation in their nanoplate sizes [152].

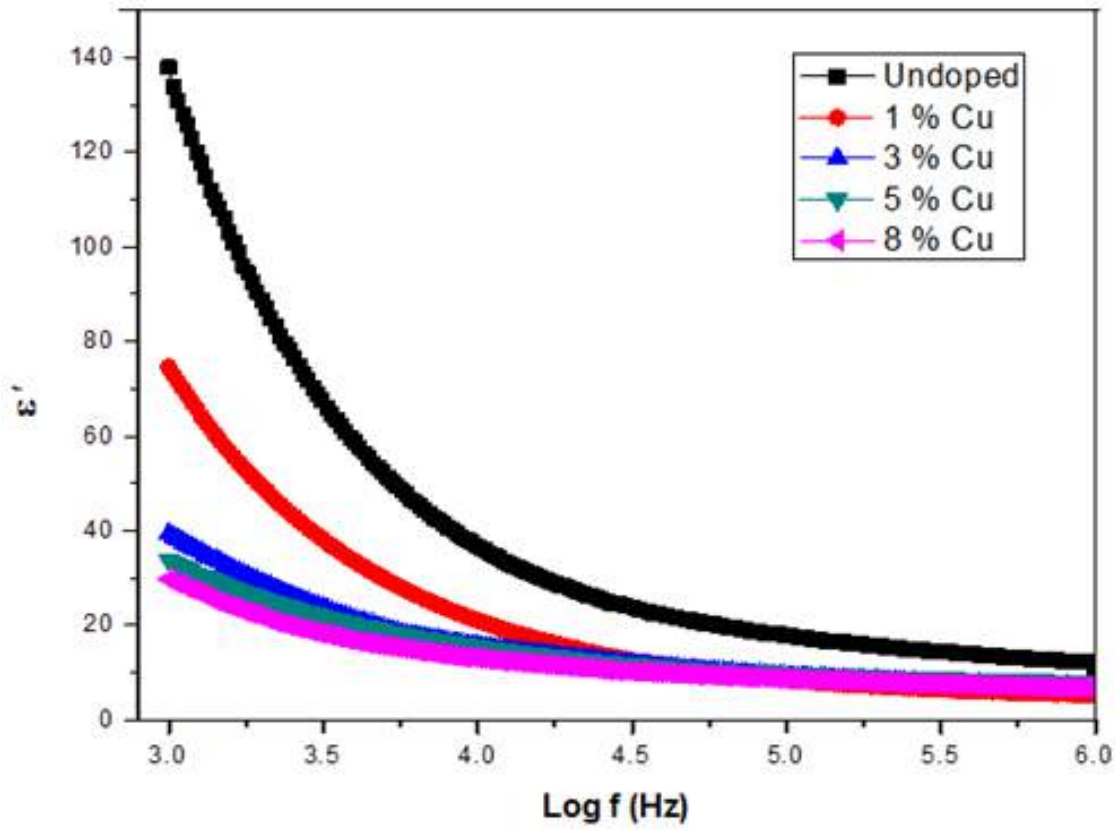

Figure 6.7 dielectric constant (ε')

The dielectric loss (ε'') of the dielectric material was calculated from experimental data via equation 4.4 [152]. These results are well consistent with Koop's model and have shown in Figure 6.8 [156].

The frequency dependent σ_{ac} of the nanoplates is shown in figure 6.9. The σ_{ac} results are well coordinated with power law power law. The conductivity of WO_3 nanoplates has also been decreased Cu doping. This may be due to several factors such as oxygen vacancies and segregation of grain boundaries [157, 158].

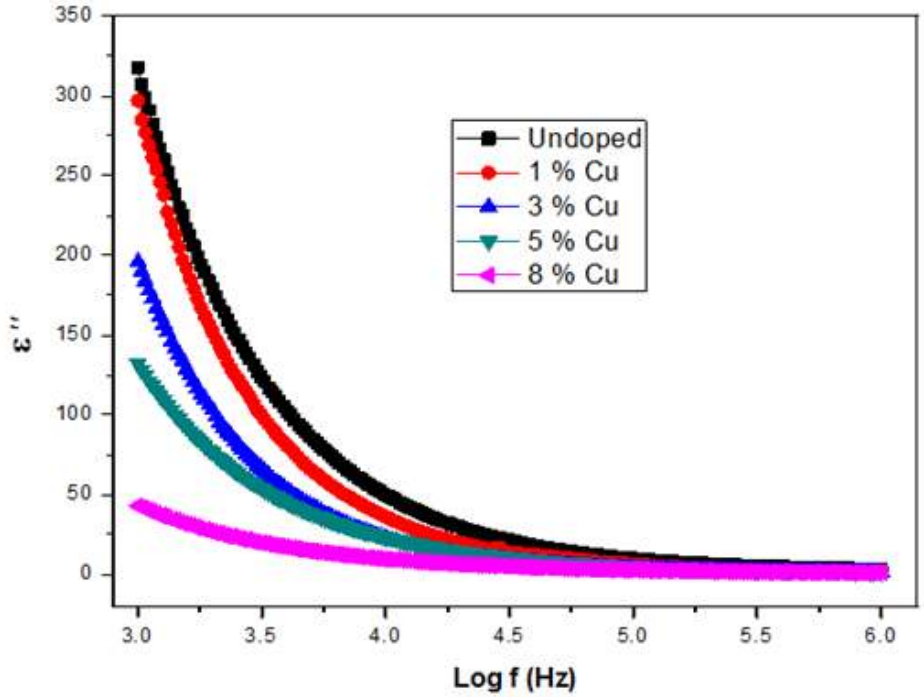

Figure 6.8 dielectric loss (ε'').

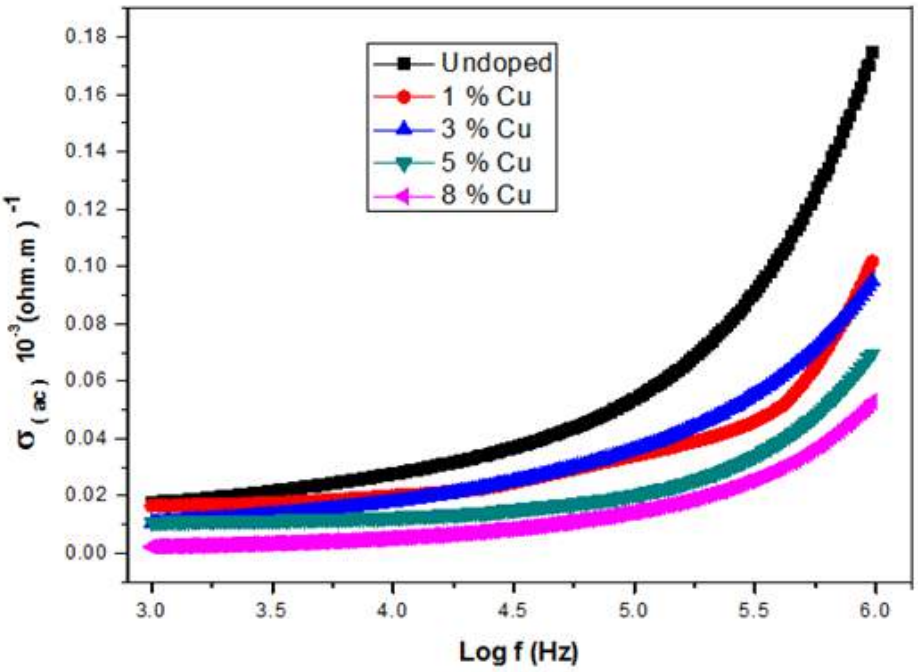

Figure 6.9 AC conductivity (σ_{ac}).

6.2.5 Visible light driven degradation of methyl red using undoped and Cu doped WO_3 nanoplates

The photocatalytic activity is achieved up to 80% with Cu doping as shown in Figure 6.10 (a, b). The photodegradation mechanism has already been explained in previous chapters [177-180, 208, 209]. The PL spectra confirm the existence of large number of oxygen vacancies. The numbers of oxygen vacancies were increased due energy band gap reduction with Cu doping into WO_3 nanoplates and as a consequence the electron hole pairs recombination rate is reduced. Therefore photocatalytic dye degradation efficiency is increased remarkably with Cu doping.

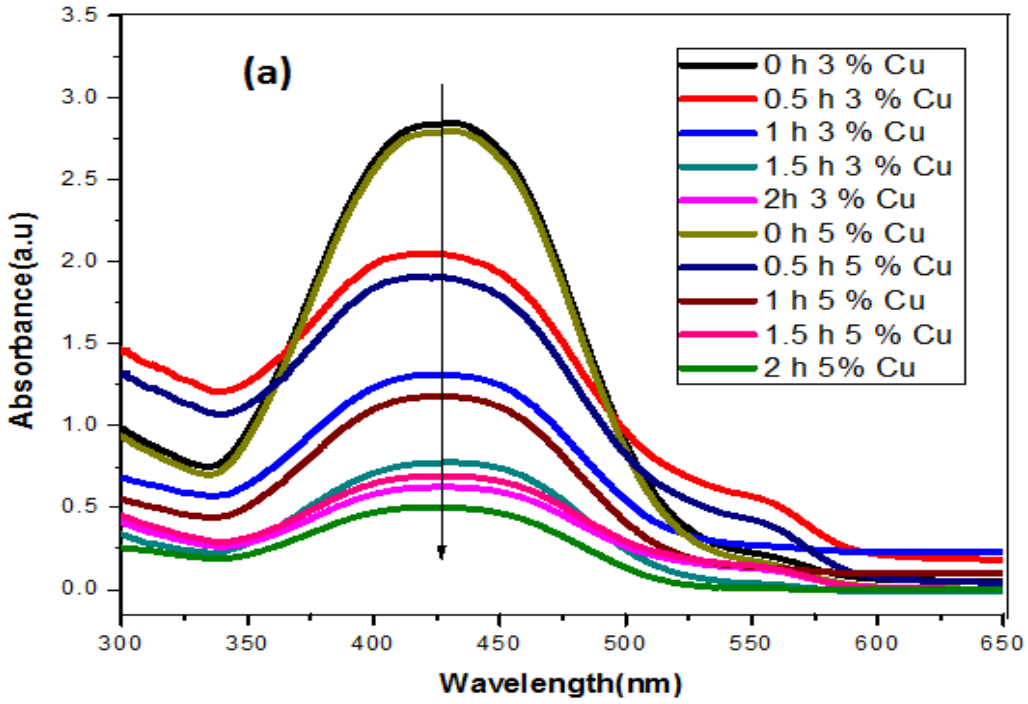

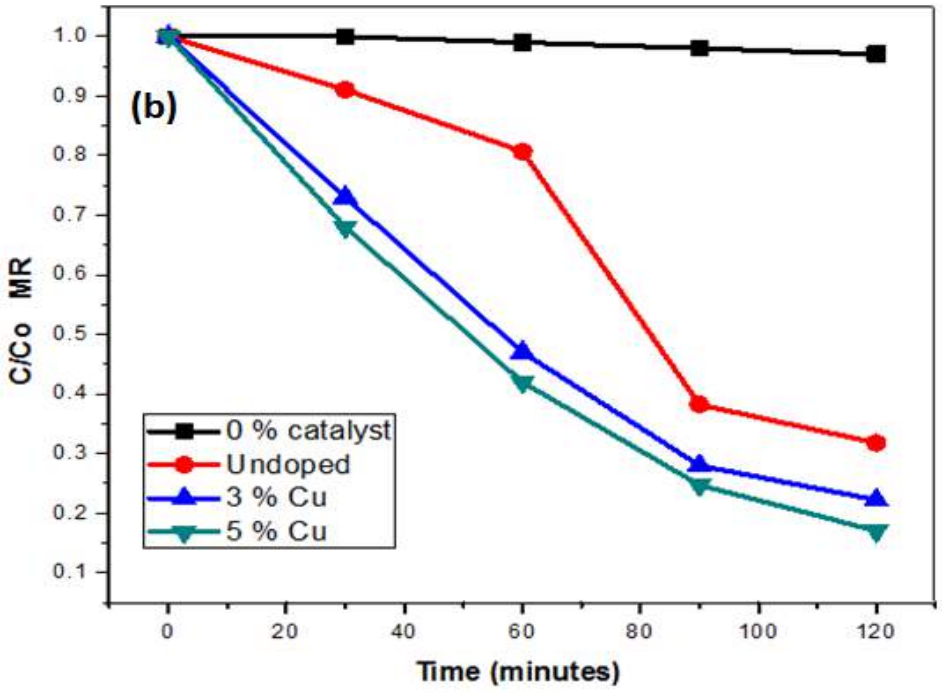

Figure 6.10 (a) Photodegradation of methyl red under visible light irradiation using Cu doped WO_3 nanoplates **(b)** C/C_o versus time plot for the visible light driven photodegradation of methyl red (MR) using undoped and Cu doped WO_3 nanoplates.

6.2.6 Differential anticancer activities investigations

Differential cytotoxicity of Cu doped WO_3 nanoplates were explored for the breast (MCF-7) cancer cells, lever Hep-2) cancer cells and human ectocervical epithelial (HECE) healthy cells through MTT assay. Figure 6.11 depicts percent cells viability against (MCF-7 and Hep-2) cancerous and healthy (HECE) cells. Interestingly, it has been found that the percent cell viability of healthy cells remain unaltered after exposure to Cu doped nanoplates, which shows the biocompatibility of Cu doped WO_3 nanoplates. Moreover, the breast and liver cancer cells viability decreased systematically with Cu doping. It can be seen from Figure 6.11 that maximum cancer cells viability is reduced to about 60 % and 65 % against the MCF-7 and the

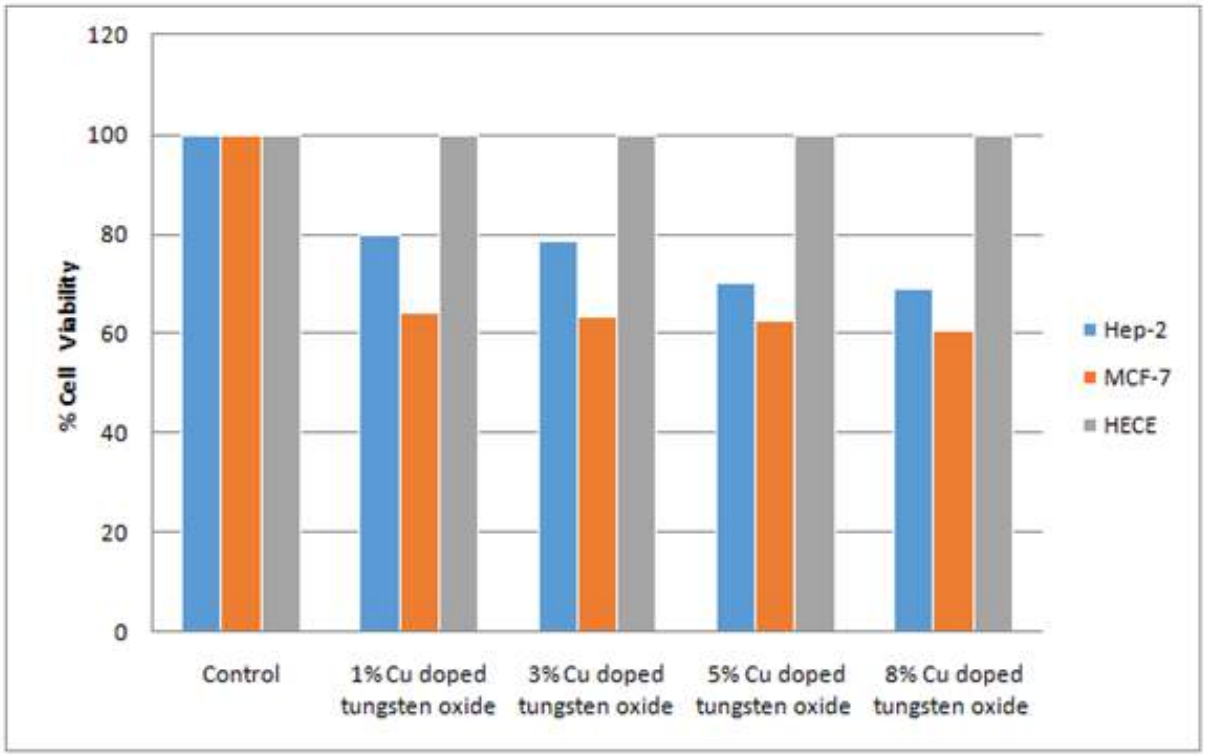

Figure 6.11 Effect of Cu doped WO_3 nanoplates on cancerous MCF-7, Hep-2 cells viability as well as against healthy human HECE cells viability

Hep-2 cancer cells, respectively with 8 % Cu doped WO_3 nanoplates without harming the healthy cells. Our results suggest that Cu doping has enhanced selective killing ability of WO_3 nanoplates towards cancer cell without posing any threat to the healthy cells. Here a question arises that why the prepared nanoplates selectively kill cancer cells by accumulating within cells and ROS generation, while protecting healthy cells? This may be due to the biochemical differences between healthy and cancer cell lines [210, 211].

CHAPTER 7

SYNTHESIS, CHARACTERIZATIONS, PHOTOCATALYTIC AND ANTICANCER ACTIVITIES OF Co DOPED WO_3 NANOSTRUCTURES

7.1 Introduction

The optical and catalytic activity of WO_3 nanomaterials can be efficiently improved via transition metal ions doping [84, 212-214]. The generation of charge carriers is one of the key factors for the degradation of organic pollutants. The cationic doping into WO_3 host matrix has different ionic states which can increase optical and photocatalytic activities because the dopant can generate lot of oxygen vacancies, which can act as a charge trappers, in order to obtain charge neutrality [87, 145, 146, 215]. Previous reports suggest that the photodegradation activity of methyl orange could be further enhanced with Co doping into WO_3 nanostructure by tuning its optical band gap energy [216]. Arul et al. reported that the enhancement of catalytic activity with Co doping into metal oxide nanomaterial [217]. Fazal et al. reported that the Co doping into metal oxide nanoparticles improves the anti cancer activity against cancer cells due to structural defects like oxygen vacancies [218]. In this study, the effects of Co doping on the structural, optical, electrical and photodegradation as well as anti cancerous properties of WO_3 nanoplates has been examined.

7.2 Results and discussions

7.2.1 Structural and morphological studies

The absence of Co related peaks in WO_3 samples doped up to 5 mol. % patterns provides the evidence of successful Co doping into the WO_3 crystal structure in Figure 7.1. Only a small variation in the peaks intensity with Co doping suggests good crystallinity for doped samples. The slight change in lattice constant with Co doping is probably linked with the difference in respective ionic radii of W^{6+} (0.062 nm) and Co^{2+} (0.072 nm) ions [216].

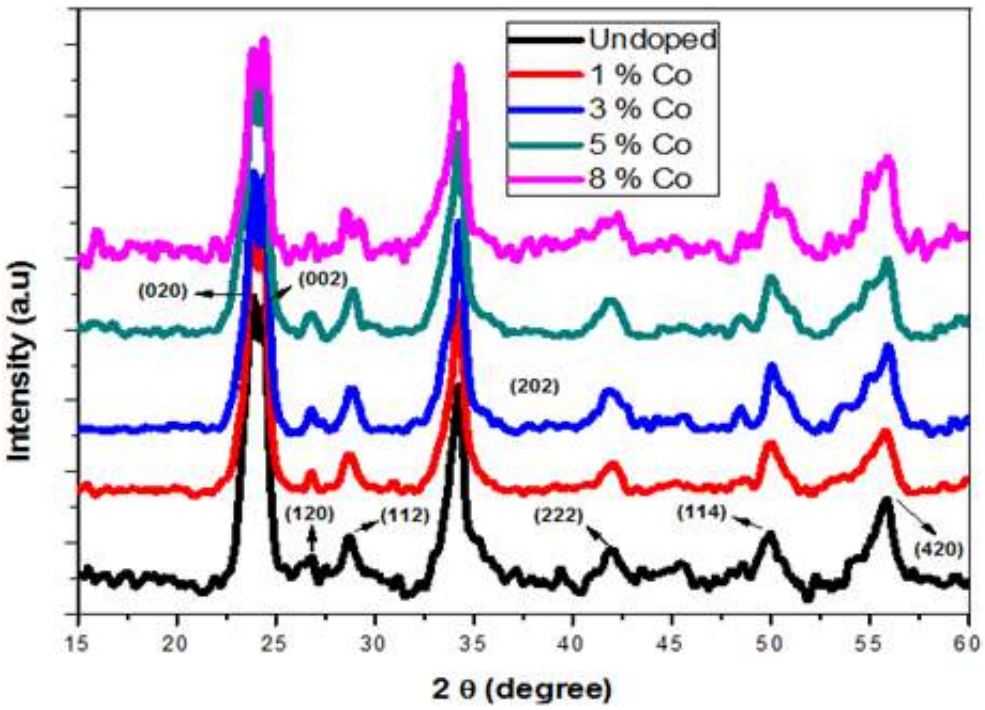

Figure7.1 XRD patterns of undoped and Co doped WO_3 nanoplates.

The surface morphology and chemical composition of the undoped and Co doped WO_3 samples have been examined by SEM and EDX. SEM images of the prepared samples are given in figure 7.2 (a-e). As evident from the SEM images, two dimensional (2-D) square plate-like morphologies are observed in undoped and Co doped samples. The undoped WO_3 is composed of nanoplates having average thickness of about 48 nm. However, there is a slight decrease in the thickness of nanoplates with Co doping.

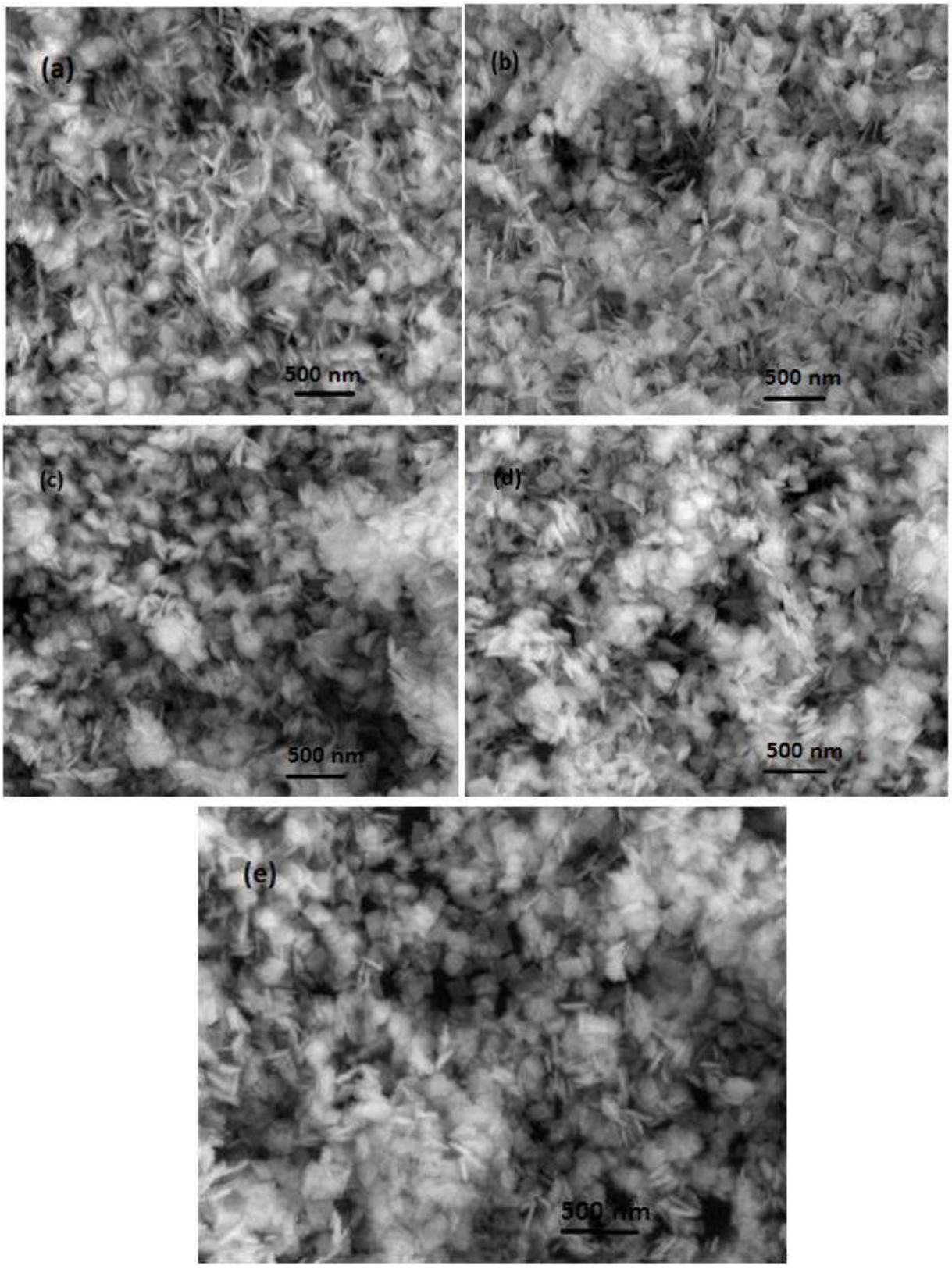

Figure 7.2 SEM images of (a) undoped (b) 1% (c) 3% (d) 5% and (e) 8% Co doped WO_3 nanoplates.

Figure 7.3 depicts the energy-dispersive X-ray spectroscopy (EDX) spectra of undoped and Co doped WO_3 nanoplates. The EDX spectra reveals the presence of Co ions in doped nanoplates by displaying Co peaks while this peak is absent in undoped samples which confirm the successful doping of Co ions into WO_3 matrix.

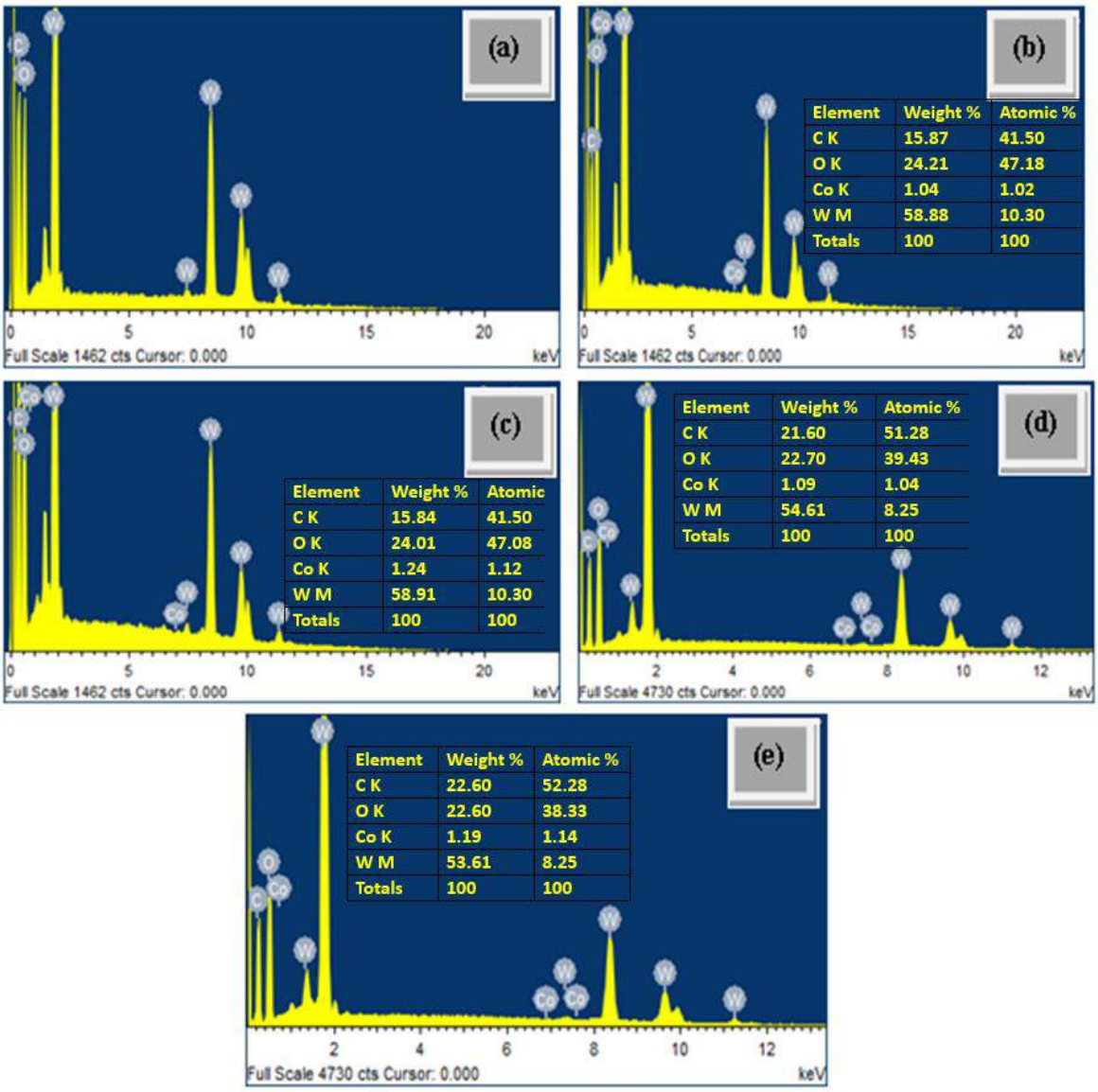

Figure 7.3 EDX spectra of (a) undoped (b) 1% (c) 3%, (d) 5% and (e) 8% Co doped WO_3 nanoplates.

7.2.2 FTIR and Raman spectroscopic studies

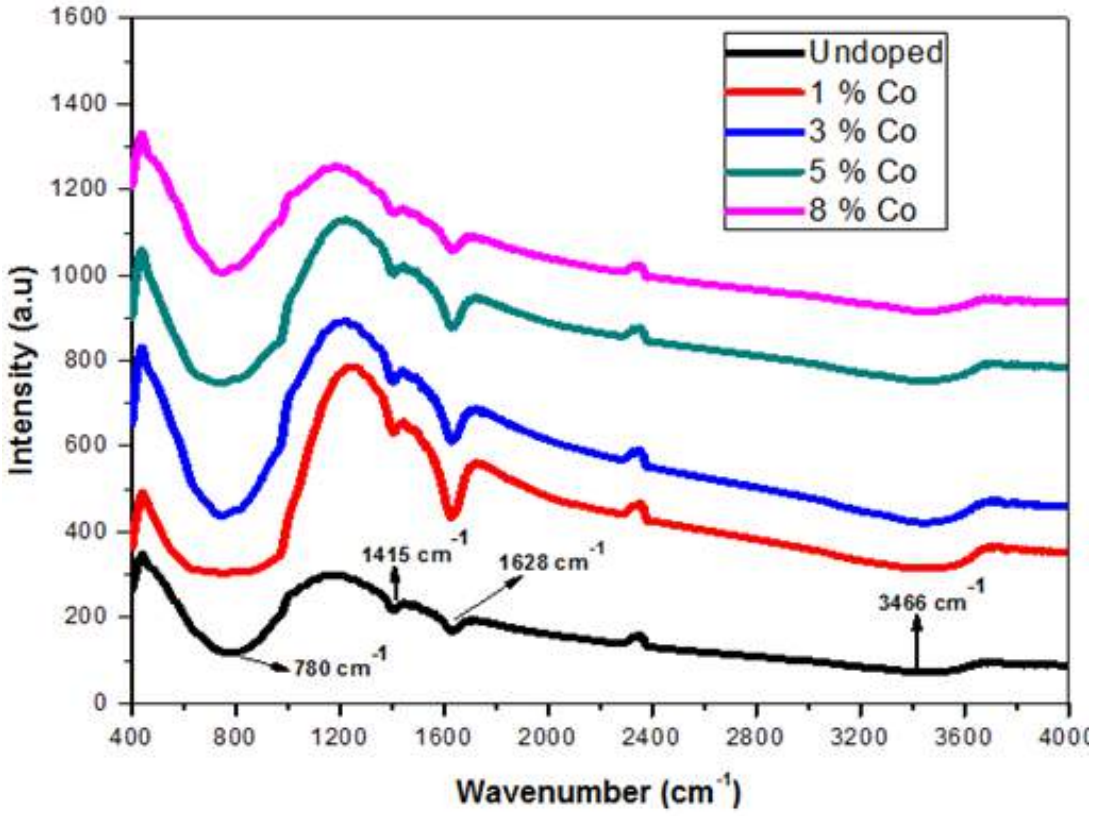

Figure 7.4 FTIR spectra of undoped and Co doped WO_3 nanoplates.

In Figure 7.4, the broad band located at 550 to 1050 cm^{-1} is linked with the O-W-O stretching mode and the bands found at 1415 cm^{-1} and 1628 cm^{-1} belongs to the bending modes of O–H groups [66]. The broad band obtained at 3300-3600 cm^{-1} may be associated with the stretching modes of O−H groups. The presence of WO_3 stretching mode and absence of any impurity (Co) related modes further validate the successful doping of Co ions into the WO_3 monoclinic crystalline structure.

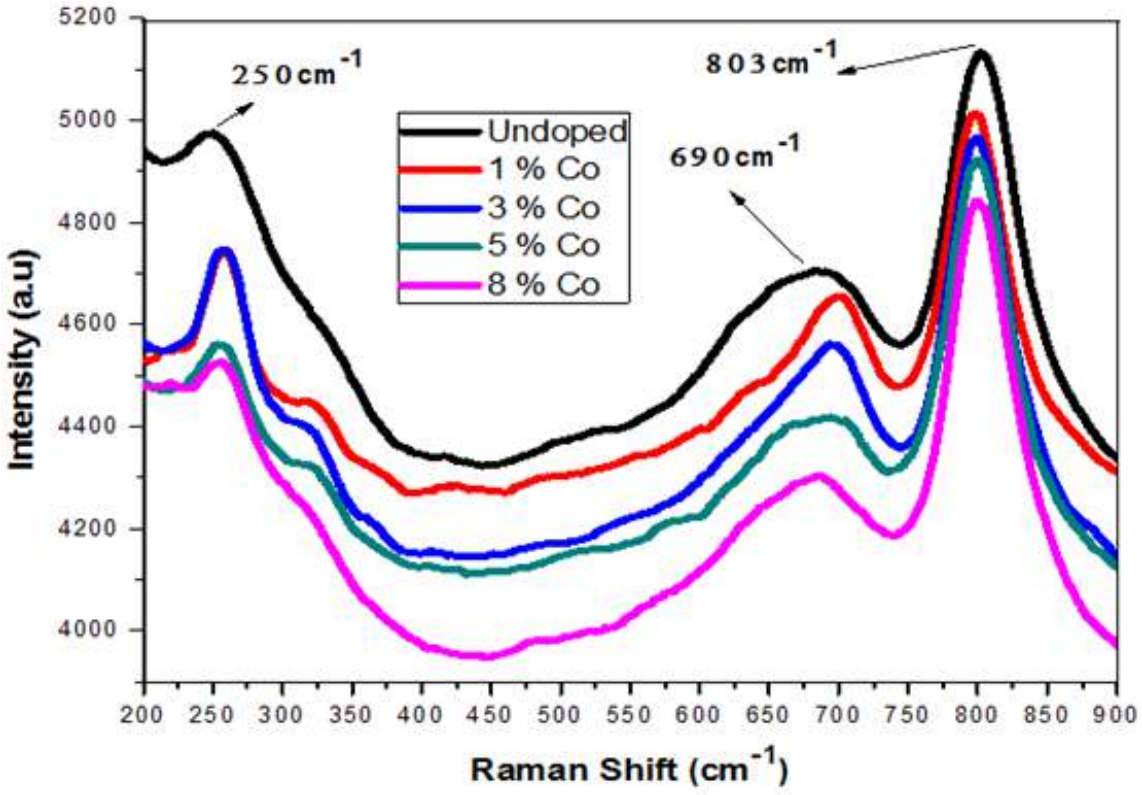

Figure 7.5 Raman spectra of undoped and Co doped WO_3 nanoplates.

Raman spectra of undoped and Co doped WO_3 nanoplates were recorded at room temperature and shown in Figure 7.5. The stretching vibrational modes υ (O–W–O) are found at 690 and 803 cm^{-1} and bending vibrational modes δ(O–W–O) are observed at 250 cm^{-1}[143]. The observation of slight shift in Raman peak position upon Co doping may be linked to the formation of defects which are an inevitable consequence of the different valance states of Co^{2+} and W^{6+} ions [67, 68]. In doped samples, no Raman band is found related to Co related vibrations.

7.2.3 X-ray photoelectron spectroscopy (XPS) studies

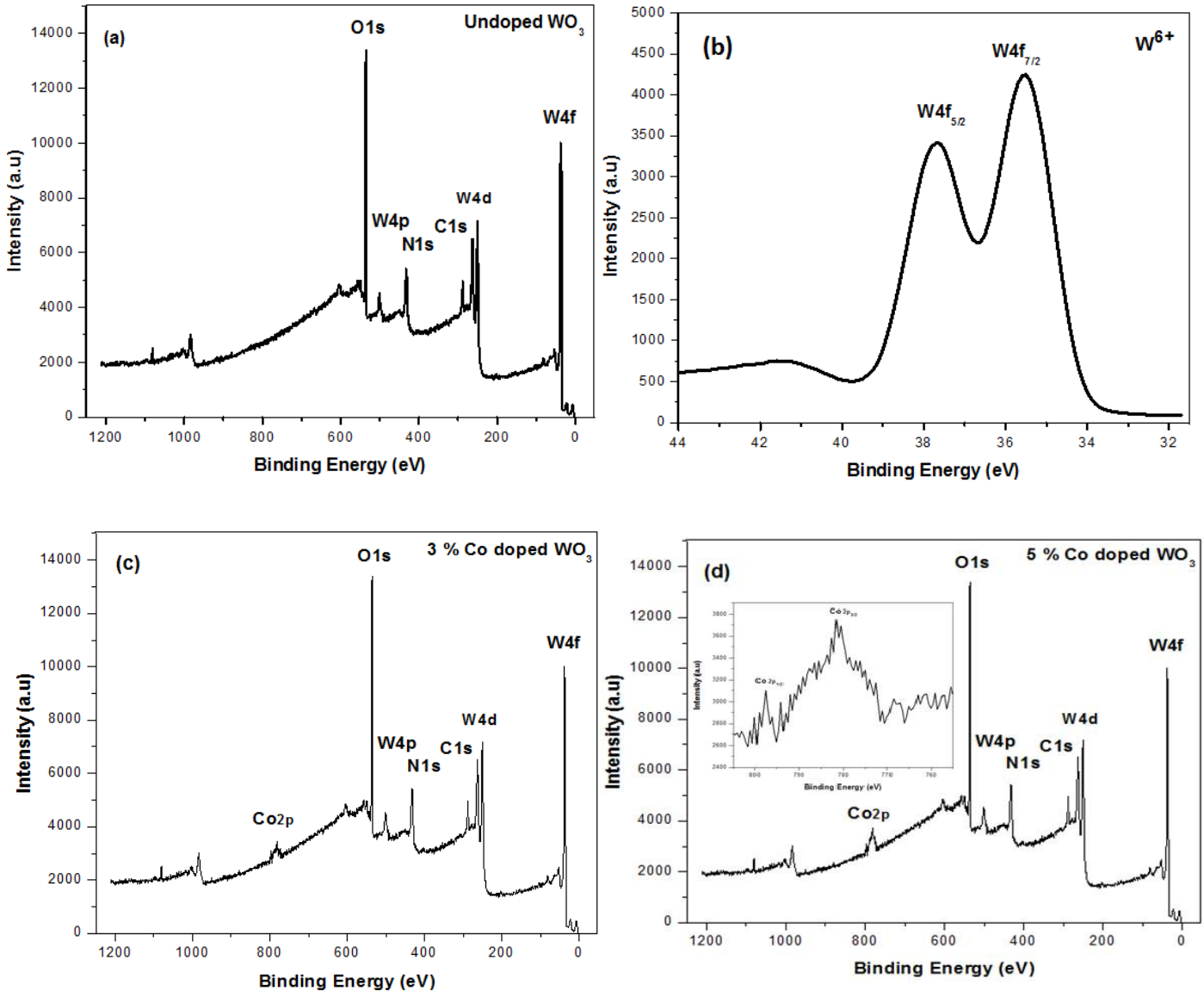

Figure 7.6 XPS spectra of **(a)** undoped WO_3 nanoplates **(b)** core level spectra of undoped WO_3 nanoplates **(c)** 3 % Co doped and **(d)** 5% Co doped WO_3 nanoplates (Inset of the figure depicts the plot Co2p)

The XPS survey scan spectra of undoped WO_3 nanoplates depict that the main peaks could be attributed to O and W elements as shown in Figure 7.6 (a). There is also presence of some minute impurities related peaks which could be assigned to C1s and N1s elements. Figure 7.6 (b) depicts the core level XPS W4f spectrum demonstrating the presence of two peaks linked to $4f_{7/2}$ and $4f_{5/2}$ which hints that W elements in the sample exist in the form of W^{6+} [146]. Figure 7.6 (c) and (d) show the XPS spectra of 3 and 5 mol. % Co doped WO_3 nanoplates respectively, which indicates the presence of same peaks as for undoped sample except one peak which is related to Co2p. The core level XPS spectrum of Co2p for 5 mol. % Co doped WO_3 nanoplates is the inset of Figure 7.6 (d) depicting two peaks related to $Co2p_{3/2}$ and $Co2p_{1/2}$. This demonstrates that Co ions with valance state of +2 are successfully doped into WO_3 nanoplates.

7.2.4 Diffusion reflectance spectroscopic analysis

The precise information about optical absorption characteristics of nanostructure has utmost significance regarding photocatalytic degradation applications. Diffused reflectance spectroscopy (DRS) was applied to inspect the optical characteristics of prepared nanoplates. The optical band gap energies of the prepared nanoplates have been calculated by Kubelka-Munk relation (equation 4.1, 4.2) [206]. The bang gap energies have been shown in the inset of figure 7.7. The undoped WO_3 sample has shown energy band gap of about 2.40 eV which is observed to decrease down to 2.15 eV with 8 % Co doping. This decrease in the band gap energies with Co ions doping may be due to the creation of localized states in the band gap which are caused by the creation of crystal defects like dislocations, stacking faults and more oxygen vacancies [207].

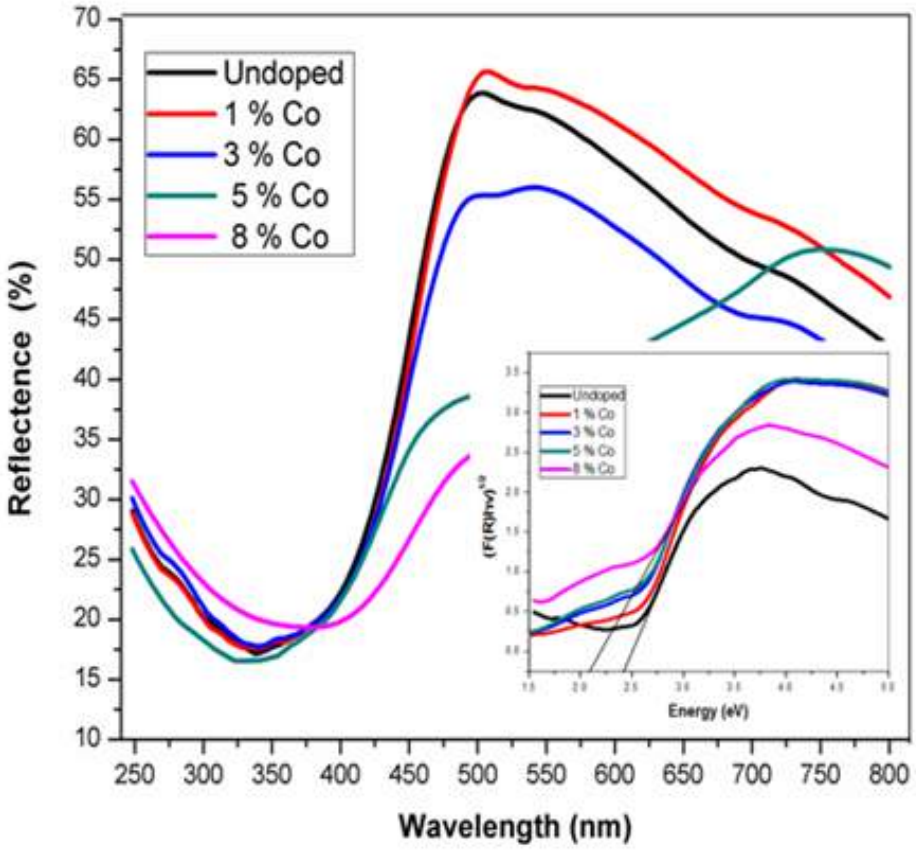

Figure 7.7 DRS spectra of undoped and Co doped WO_3 nanoplates (Inset of the figure shows band gap energies calculation).

7.2.5 Photoluminescence spectra investigations

In Figure 7.8, the peak located at 417 nm belongs to near band edge emission (NBE). The high intensity peak found at 536 nm is assigned to defects [145]. The particle morphology and size play vital role in the variation of PL intensities of prepared samples [149-151]. The NBE and defects peaks intensities significantly decrease with Co doping as a consequence of large number of defect densities.

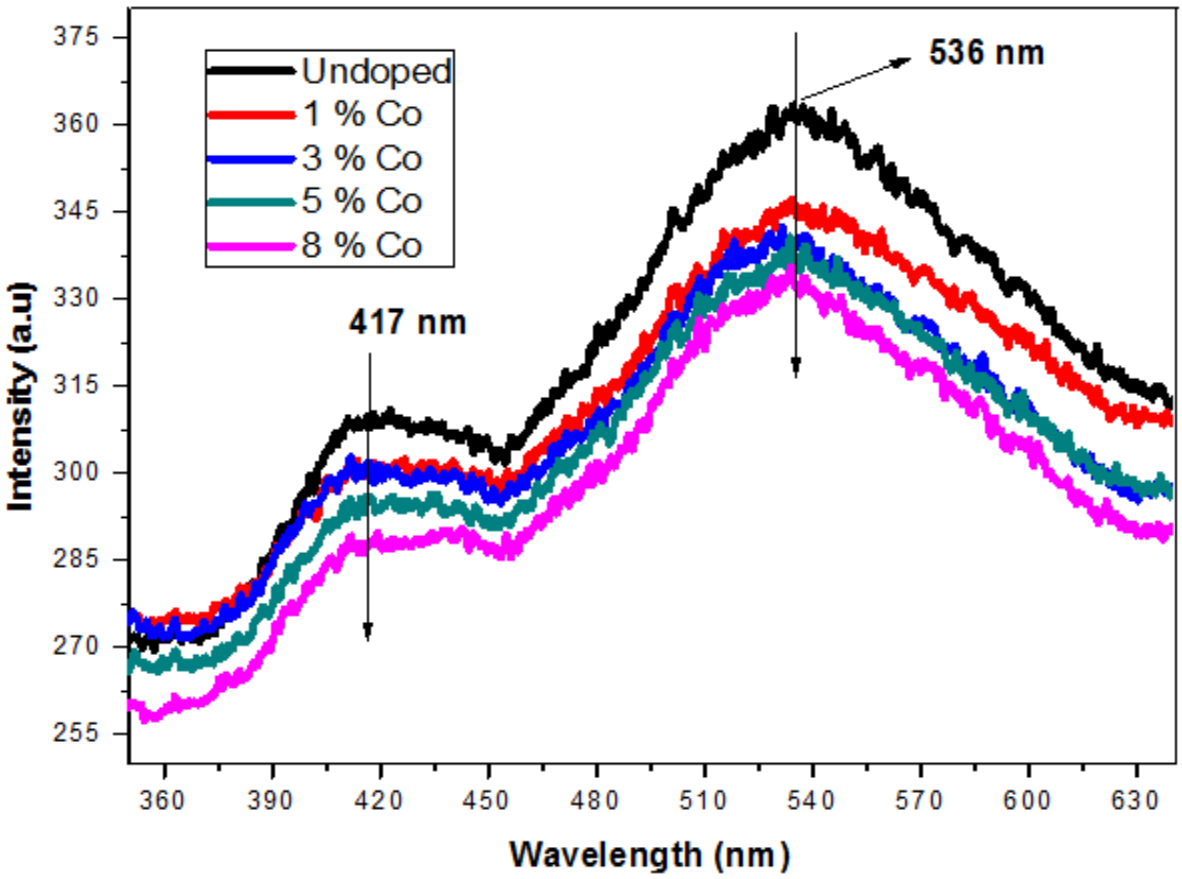

Figure 7.8 PL spectra of undoped and Co doped WO_3 nanoplates.

7.2.6 Electrical and dielectric studies

In Co doped samples, the initial value of ε' at lower frequency range decreases with Co doping. This variable nature of ε' is directly linked with the polarization which varies due to electronegativity difference between dopant Co (1.88) and host matrix W (2.36) [152]. Figure 7.10 depicts the dielectric loss (ε'') of prepared samples. Dielectric loss (ε'') was measured from experimental data using equation 4.4 [152]. Dielectric loss (ε'') has similar trend as the ε'. This dielectric loss (ε'') behavior is in well accordance with Koop's model.

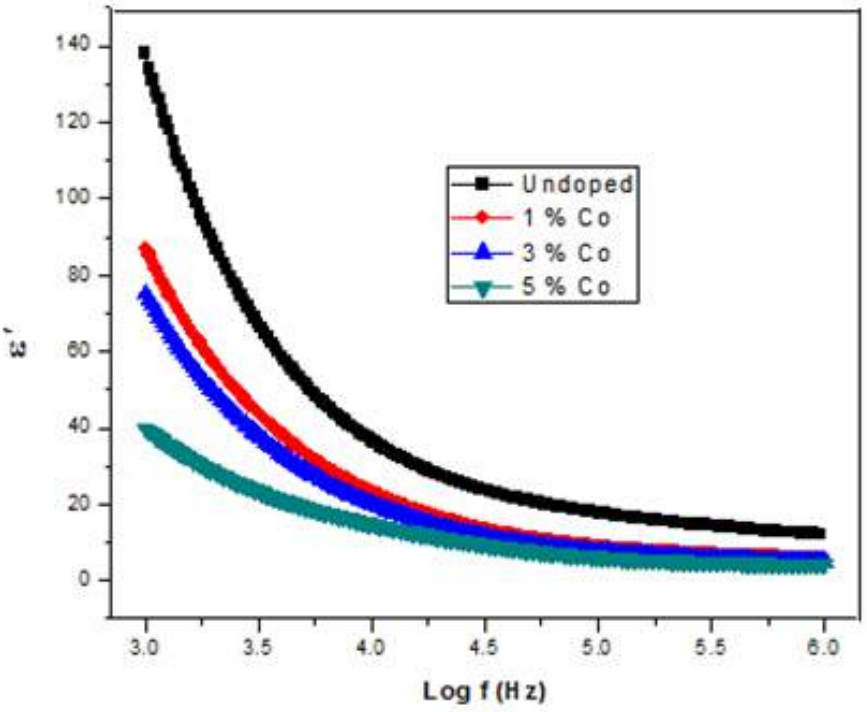

Figure 7.9 dielectric constant (ε').

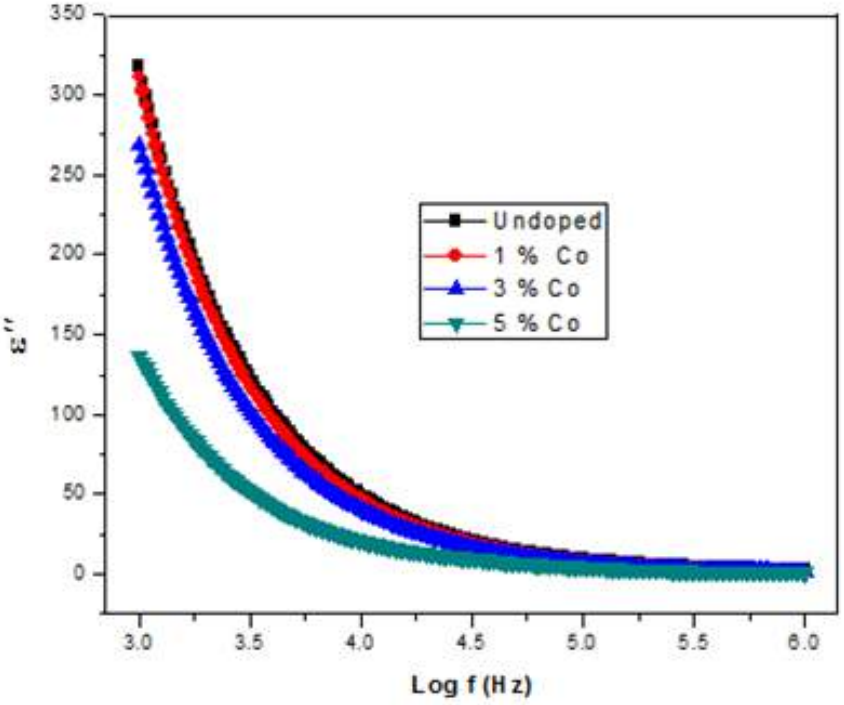

Figure 7.10 dielectric loss (ε'')

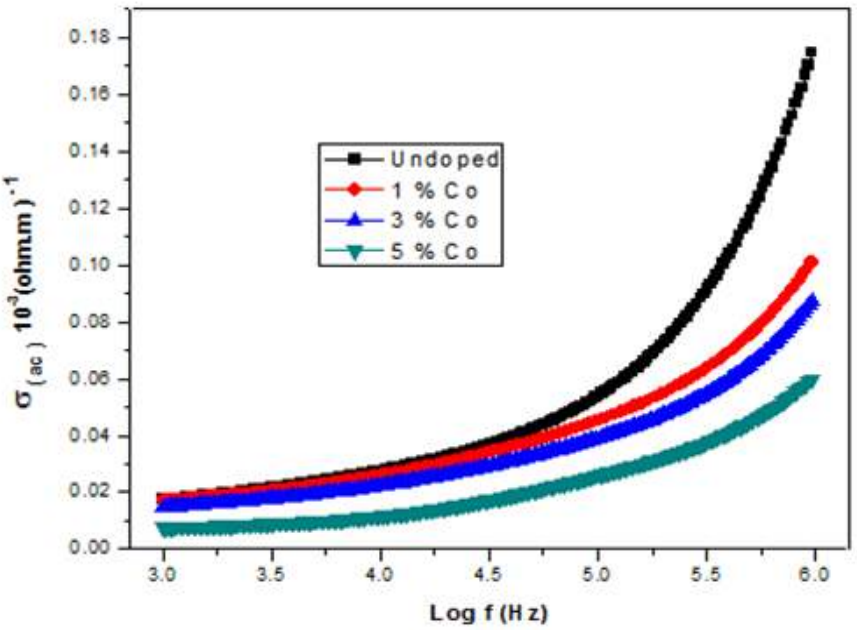

Figure 7.11 AC conductivity (σ_{ac})

Accordance to this model, higher value of resistivity in the lower frequency range is happened due to the grain boundaries. The ε''significantly decreases with Co doping due to less electrical polarization and it can be useful for high frequency based bio-sensing applications [219].

The AC conductivity (σ_{ac}) of the as synthesized nanoplates was measured by the equation 4.5 [152]. Figure 7.11 shows the σ_{ac} of undoped and Co doped WO_3 nanoplates. The conductivity enhances rapidly at high frequency range because of dominant grain conduction effects. These σ_{ac} responses are in well accordance with power law. Moreover, conductivity also decreases markedly with the Co doping due to defects [157].

7.2.7 Visible light driven degradation of methyl red using undoped and Co doped WO_3 nanoplates

Photocatalytic advanced oxidation process is an environmentally friendly technology for water pollutant degradation. In this regard, 2-D nanomaterials holds high surface area, increased number of reaction sites and minimal difference in the catalytic activity at different sites [220]. In Figure 7.12 (a-d), the photodegradation activities have been found to enhance up to 90% in 2 hours with Co doped WO_3 nanoplates. The mechanism of photocatalytic dye degradation has already been explained previously [221, 222]. The PL spectra confirm the existence of large number of oxygen vacancies. The oxygen vacancies have been increased due energy band gap reduction with Co doping into WO_3 nanoplates and as a consequence the photo generated electron hole pairs recombination rate has been decreased. Therefore, photocatalytic dye degradation efficiency is remarkably increased with Co doping. The small space-charge regions and least band bending are produced in nano scaled WO_3 which allows the photo-generated charge carriers to migrate easily to surface and react with dye molecules. Apart from defects, the doping of metal ions lead the optimum band structure of WO_3 at nano scale due to effective intercalation of dopants which results in higher photocatalytic performance of doped WO_3 nanoplates [223, 224].

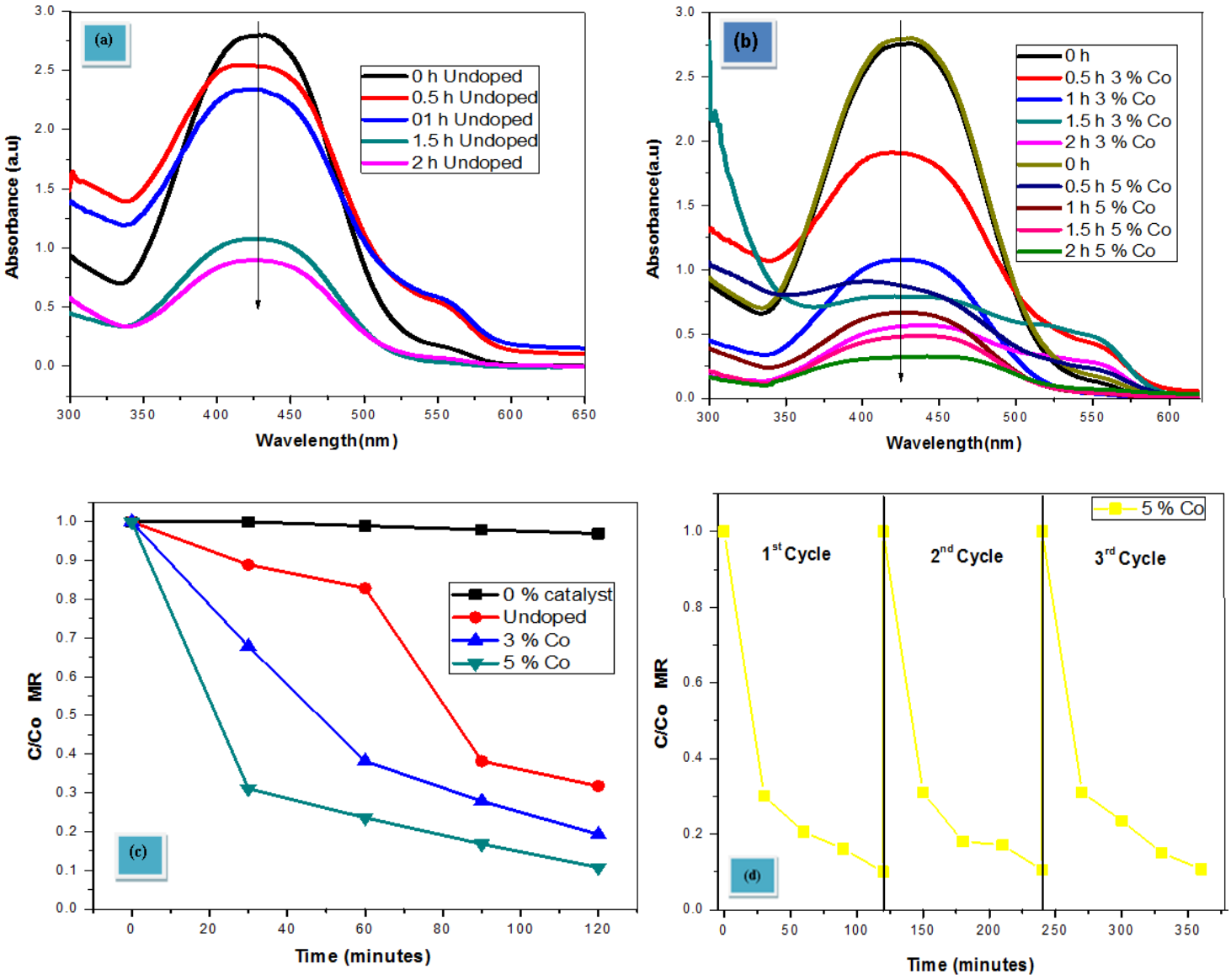

Figure 7.12 (a) Photodegradation of methyl red under visible light illumination by undoped WO_3 nanoplates. **(b)** Photodegradation of methyl red under visible light irradiation using Co doped WO_3 nanoplates. **(c)** C/C_o versus time plot for the visible light driven photodegradation of methyl red (MR) using undoped and Co doped WO_3 nanoplates. **(d)** The recyclability performance of 5% Co doped WO_3 nanoplates.

7.2.8 **Anticancer characteristics**

The anticancer activities of the synthesized WO_3 nanoplates doped with different molar percentages of Co were carried out via MTT assay against breast (MCF-7) and lever (Hep-2) cancer cells.

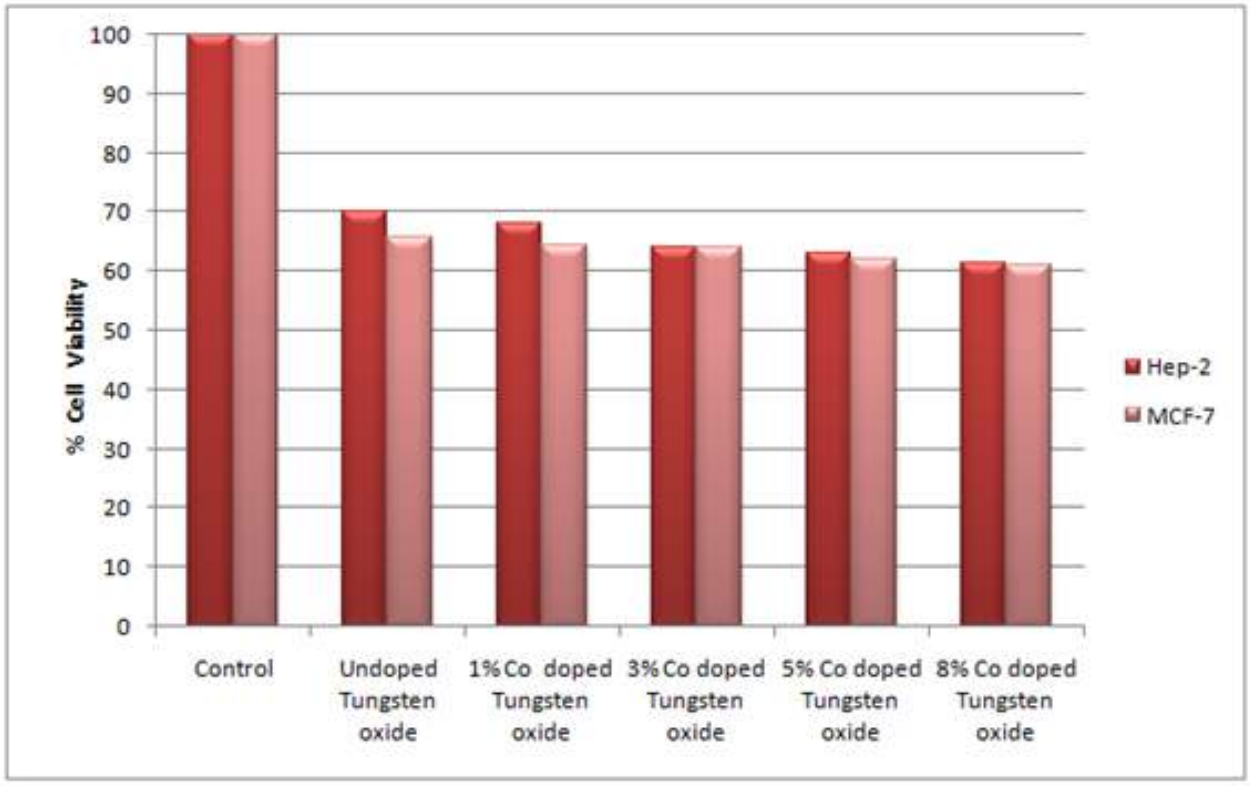

Figure 7.13 Effect of undoped and Co doped WO_3 nanoplates on MCF-7 and Hep-2 cells viability.

The undoped WO_3 nanoplates have reduced percent cell viability of both (MCF-7 and Hep-2) type of cancer cells down to 66% and 70%, respectively. The Co doping resulted in systematic reduction in cell viability of these tested cancer cells down to 60%. There are number of mechanisms proposed for the anticancer characteristics of metal oxide nanomaterials such as

accumulation of nanoparticles inside the cells, electrostatic rupturing of cell wall and excessive oxidative stress due to production of reactive oxygen species. Hence, Co doping may result in the higher uptake of WO_3 nanoplates in the cells and higher ROS production which causes higher anticancer activity of doped WO_3 nanoplates.

CHAPTER 8

SYNTHESIS, CHARACTERIZATIONS, PHOTOCATALYTIC AND ANTICANCER ACTIVITTES OF Ni DOPED WO_3 NANOSTRUCTURES

8.1 Introduction

Environmental pollution is emerging as a serious health care problem in the developed and under developed nations. The large amounts of industrial waste including organic textile dyes and acids are released into the water. Dyes containing organic compounds are believed to be dangerous and can cause severe health problems [225]. The methyl red (MR) dye has been used vastly in textile and paper printing industries [226-231]. The regular waste treatment methods are not so efficient to purify these complex chemical structures of dyes.

8.2 Results and Discussions

8.2.1 Structural and morphology analysis

Powder X-ray diffraction analysis was done for all the undoped and Ni doped WO_3 samples. Figure 8.1 shows the characteristic XRD peaks which correspond well to the monoclinic WO_3 crystal structure (JCPDS card no.043-1035). A slight decrease was seen for lattice parameters with Ni doping [207]. This can be associated to the smaller ionic radii difference between the host W (0.62 Å) and dopant Ni (0.60 Å) ions [233]. host W (0.62 Å) and dopant Ni (0.60 Å) ions [233].

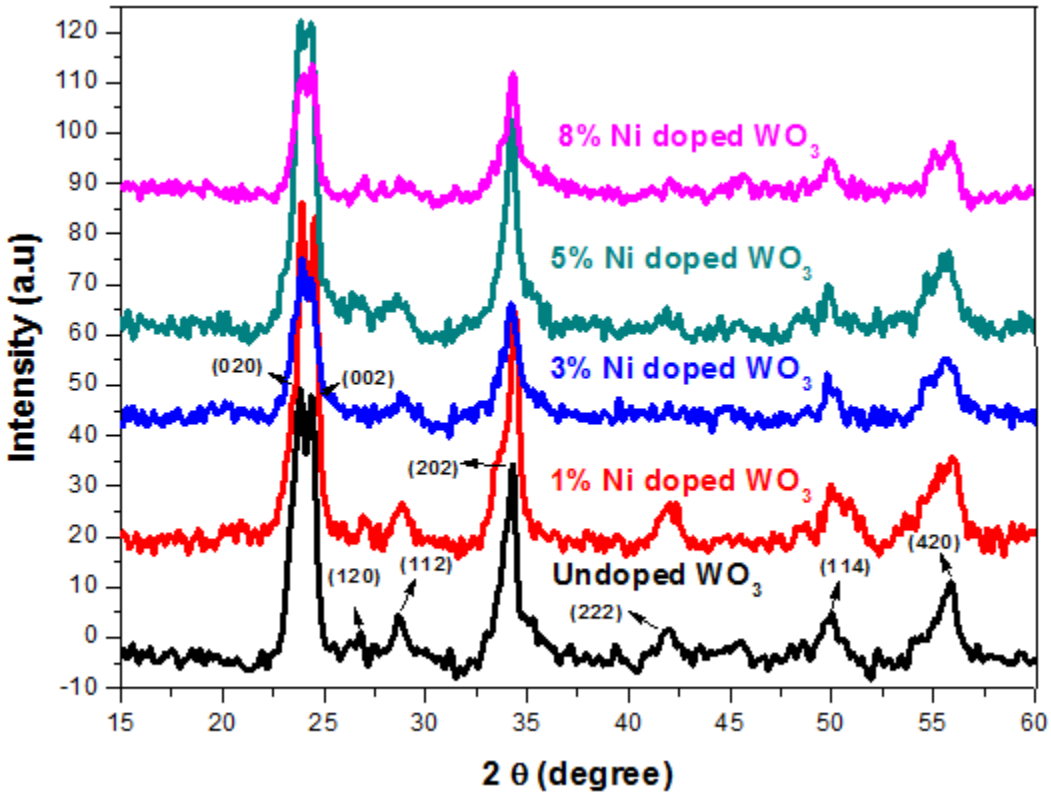

Figure 8.1 XRD patterns

The undoped WO_3 and Ni doped WO_3 samples have shown nanoplates like morphologies in figure (2a-e). The undoped nanoplates have average thickness and diameter of about 50 nm and 200 nm respectively. The particles maintain plate-like morphology with the Ni ions doping. However, there is a slight decrease in the thickness of nanoplate size (figure 8.2b-e).

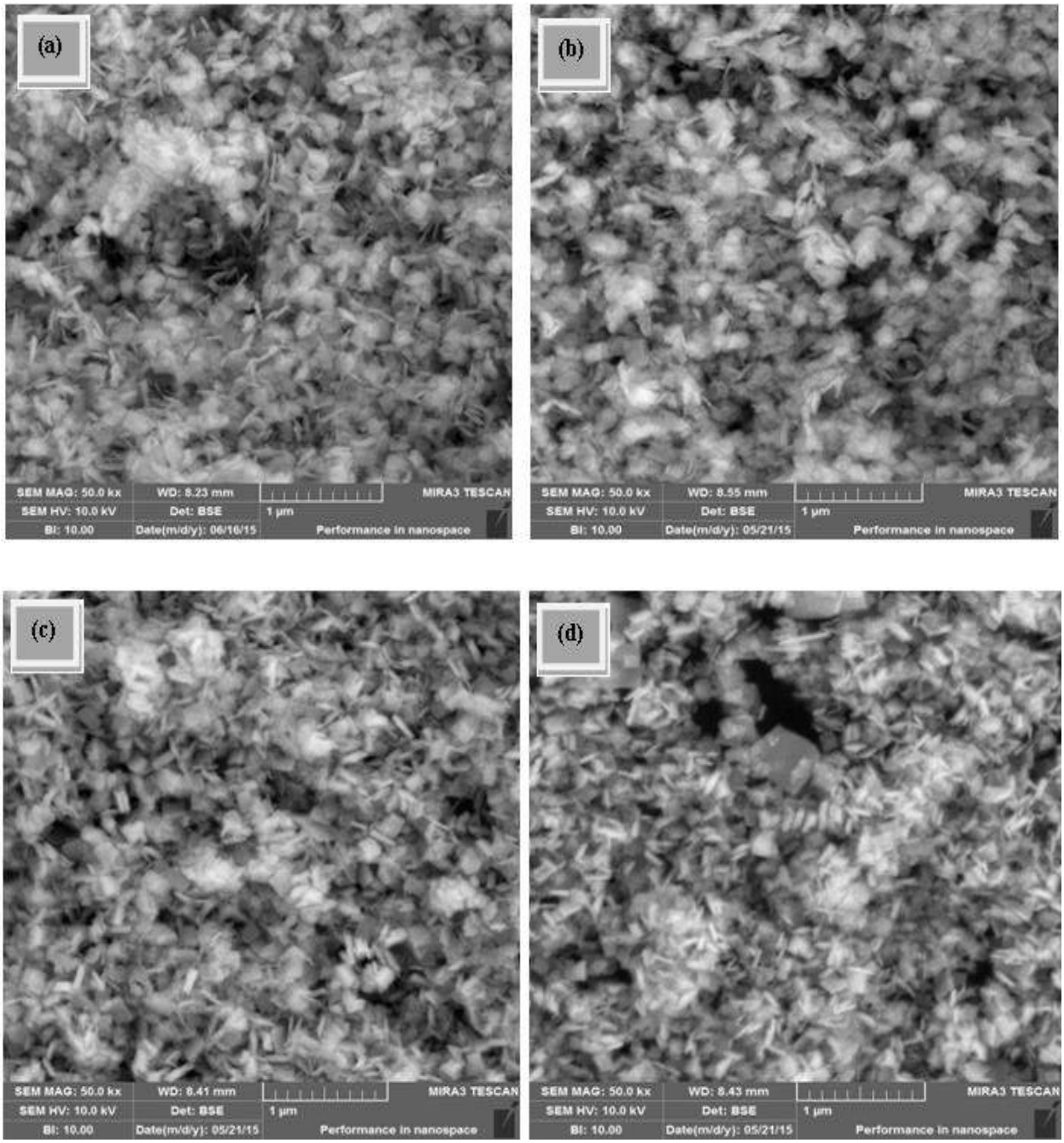
(a)
SEM MAG: 50.0 kx
WD: 8.23 mm
MIRA3 TESCAN
SEM HV: 10.0 kV
Det: BSE
1 µm
BI: 10.00
Date(m/d/y): 06/16/15
Performance in nanospace
(b)
SEM MAG: 50.0 kx
WD: 8.55 mm
MIRA3 TESCAN
SEM HV: 10.0 kV
Det: BSE
1 µm
BI: 10.00
Date(m/d/y): 05/21/15
Performance in nanospace
(c)
SEM MAG: 50.0 kx
WD: 8.41 mm
MIRA3 TESCAN
SEM HV: 10.0 kV
Det: BSE
1 µm
BI: 10.00
Date(m/d/y): 05/21/15
Performance in nanospace
(d)
SEM MAG: 50.0 kx
WD: 8.43 mm
MIRA3 TESCAN
SEM HV: 10.0 kV
Det: BSE
1 µm
BI: 10.00
Date(m/d/y): 05/21/15
Performance in nanospace

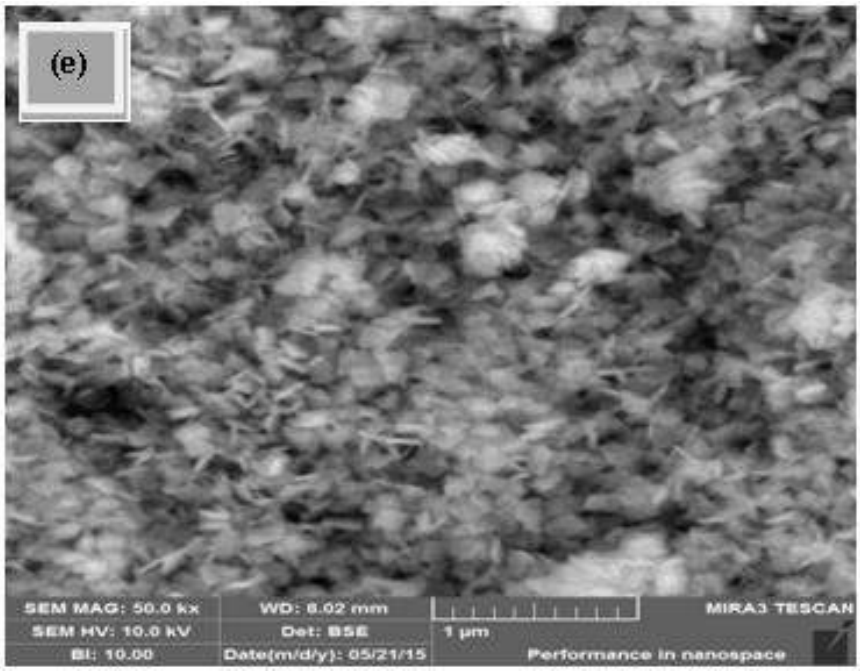

Figure 8.2 SEM images of **(a)** undoped **(b)** 1% **(c)** 3% **(d)** 5% and **(e)** 8% Ni doped WO_3 nanoplates

Figures 8.3 depict the energy dispersive X-ray spectroscopy (EDX). The presence of Ni dopant in the WO_3 host matrix is also confirmed by EDX. There are Ni peaks for the doped samples (figure 8.3b-e), while the undoped sample has no Ni peaks (figure 8.3a).

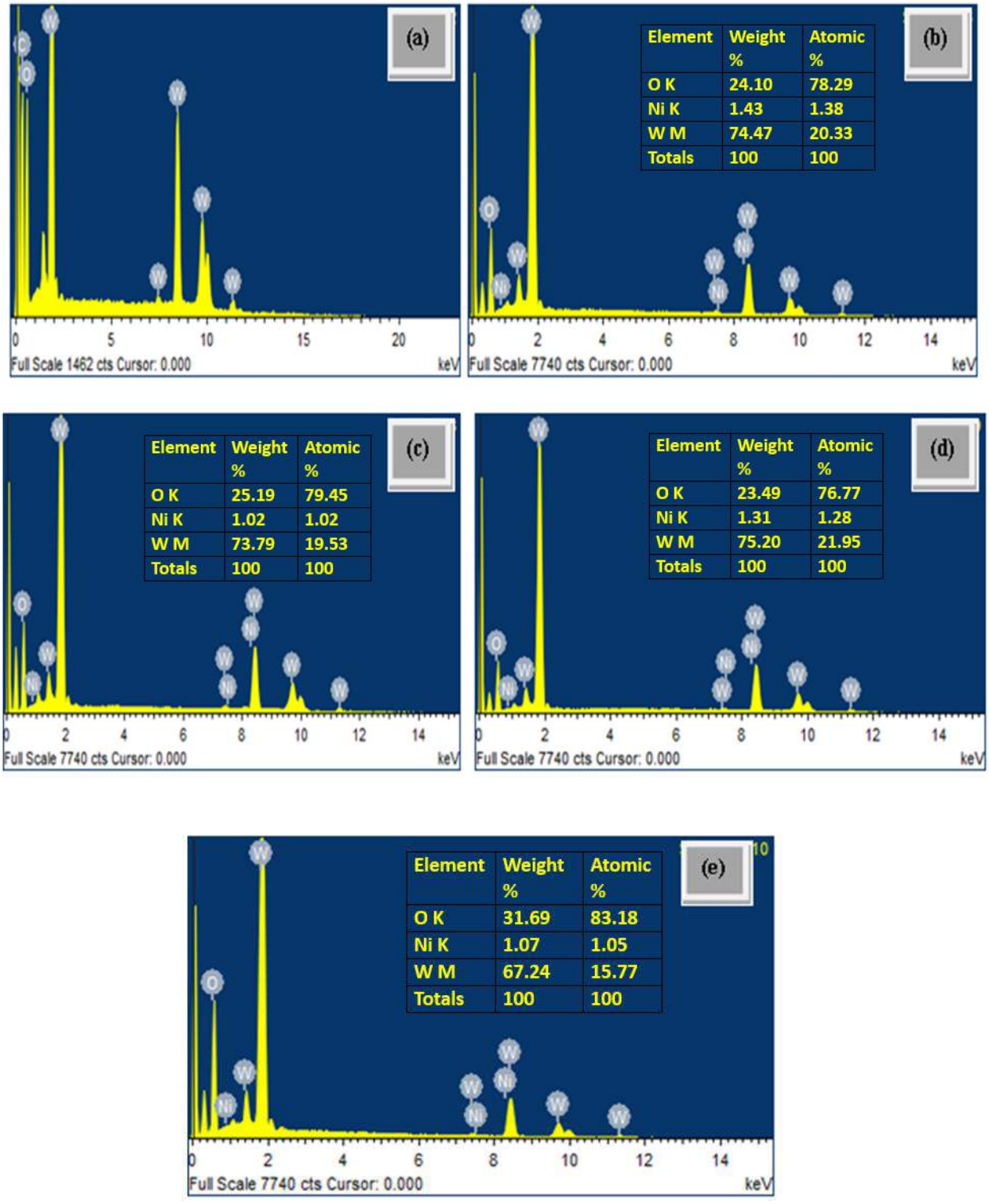

Figure 8.3 EDX spectra of **(a)** undoped **(b)** 1% **(c)** 3%, **(d)** 5% and (e) 8% Ni doped WO_3 nanoplates.

8.2.2 FTIR spectroscopic studies

In Figure 8.4, the observed FTIR bands confirm the single phase purity and monoclinic crystalline nature of the undoped and the Ni doped WO_3 nanoplates. The band found at 550-1050 cm^{-1} belongs to the stretching vibration O-W-O [66].

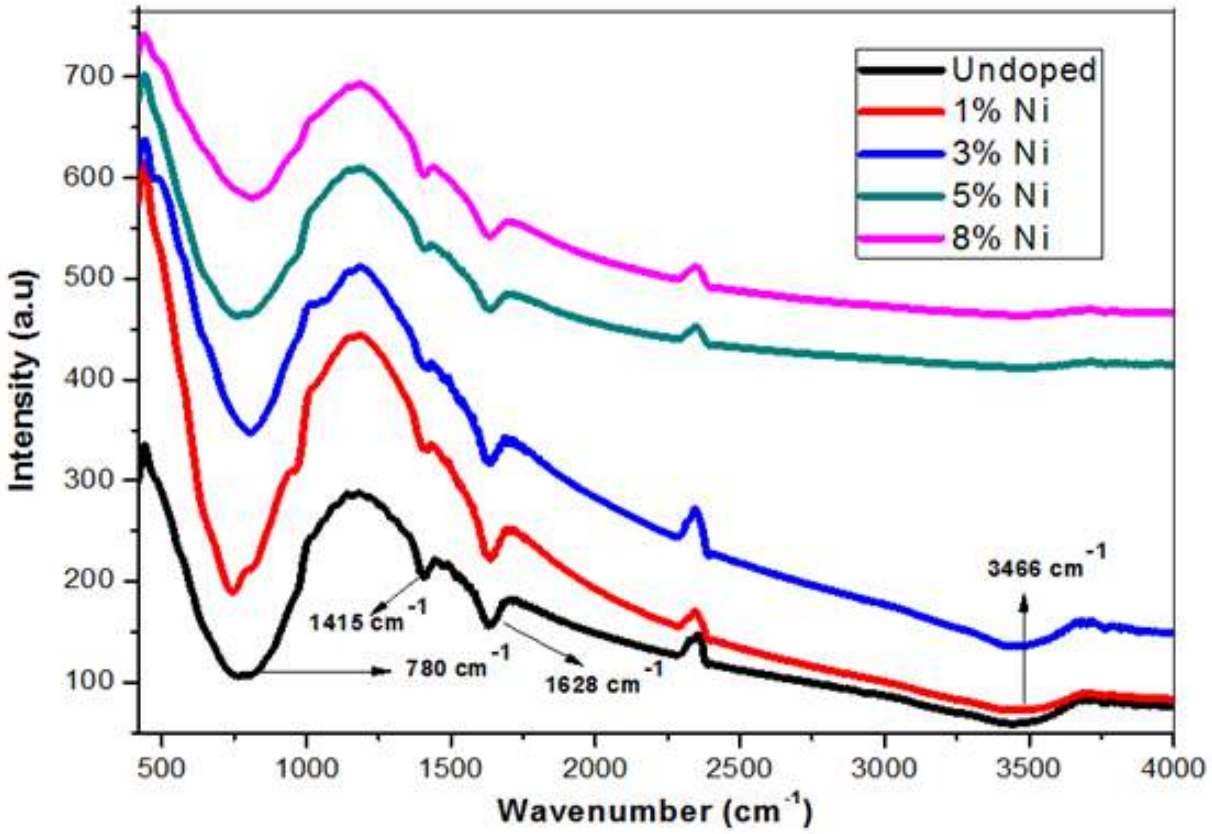

Figure 8.4 FTIR spectra of undoped and Ni doped WO_3 nanoplates.

After Ni doping, the band peaks were slightly shifted towards higher wave number may have been due to the variation in size of the doped WO_3 nanoplates [234]. The other observed vibration modes at 1415cm^{-1} and 1628 $cm^{-1}$are due to the tungsten-hydroxyl (W–OH) bond but the intensities of these absorption bands are very low which suggests a very minute hydration of

the prepared nanoplates. The stretching vibrational mode of O−H groups in H_2O is found at 3300-3600 cm^{-1} [66]. No impurity band was found in FTIR spectra.

8.2.3 Raman spectroscopic analysis

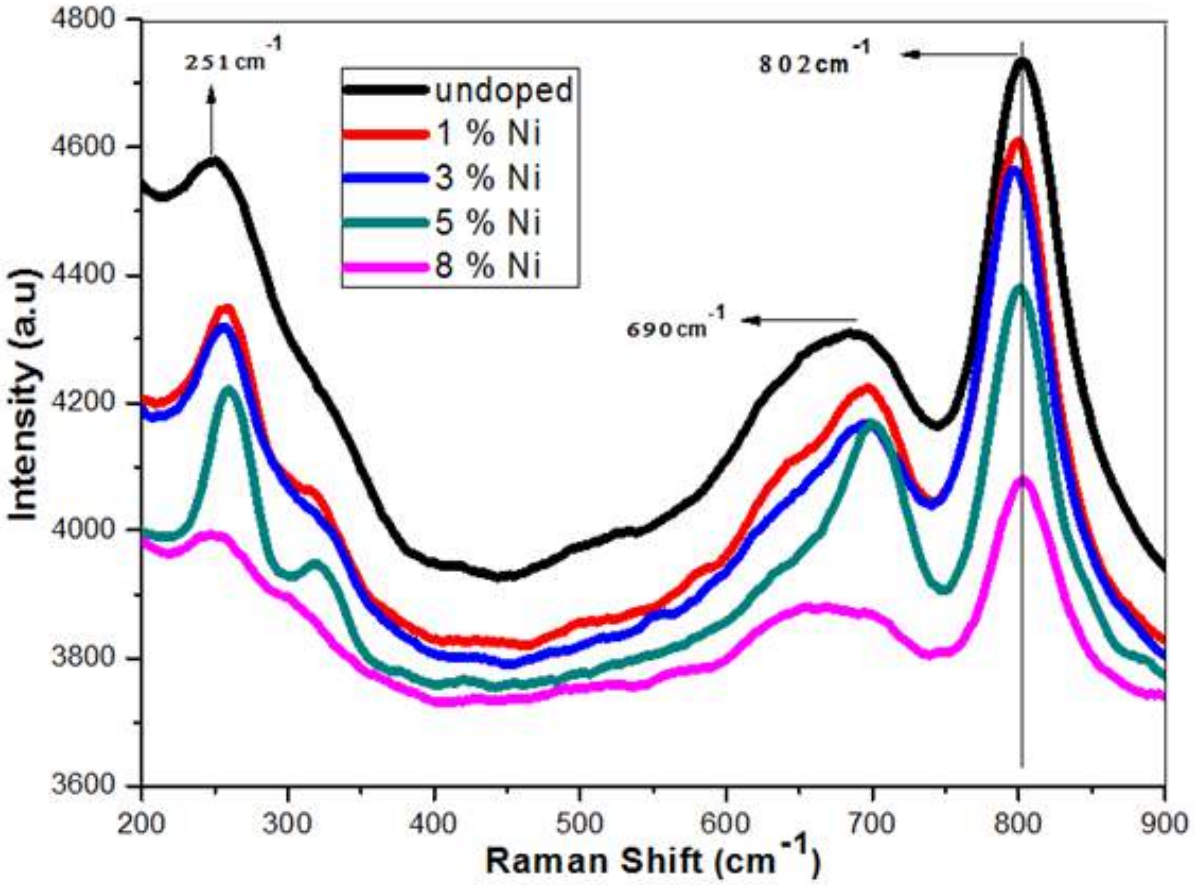

Figure 8.5 Raman spectra of undoped and Ni doped WO_3 nanoplates.

The stretching vibrational modes υ (O–W–O) are found at 690 and 802 cm^{-1} and bending vibrational modes δ(O–W–O) are observed at 251cm^{-1}. Our results are consistent with previously reported results for monoclinic WO_3 [143]. The successful Ni doping is verified due to absences of bands related to NiO or any other impurity related bands in the Raman spectra. The stretching

vibrational υ (O–W–O) peak positions were slightly shifted towards the lower wave numbers [233, 235, 236]. These observed vibration bands confirm single phase purity and monoclinic crystal nature of undoped and Ni doped WO_3 nanoplates..

8.2.4 X-ray photoelectron spectroscopy (XPS) studies

Figure 8.6 depicts the XPS spectra of undoped and 5 mol. % Ni doped WO_3 nanoplates. The XPS spectrum of undoped WO_3 nanoplates has been shown in figure 8.6(a) depicting the presence of O, W, C and N elements. Their corresponding photo electron peaks have been found to be O1s, W4p, W4d, W4f, C1s and N1s. The W4f peak is the most intense peak. The core level XPS spectrum of W4f has been shown two peaks associated to $4f_{5/2}$ and $4f_{7/2}$ in figure 8.6 (b). The presence of these peaks at corresponding energy values has demonstrated that W elements in the sample exist in the form of W^{6+} [233, 237]. The XPS spectra of 5 mol. % Ni doped WO_3 nanoplates have been shown in Figure 8.6(c). All the photo electron peaks have been found to be the same as observed for undoped WO_3 except the presence of Ni metal ions (Ni 2p) peaks [233]. Figure 8.6 (d) have been shown in the core level XPS spectrum of Ni 2p for 5 mol. % Ni doped WO_3 nanoplates. It has been observed that there are two peaks related to $Ni2p_{3/2}$ and $Ni2p_{1/2}$ which depicts Ni ions doping into WO_3 nanoplates in the form of Ni^{2+}. This demonstrates that Ni ions with valance state of +2 are successfully doped into WO_3 nanoplates [233].

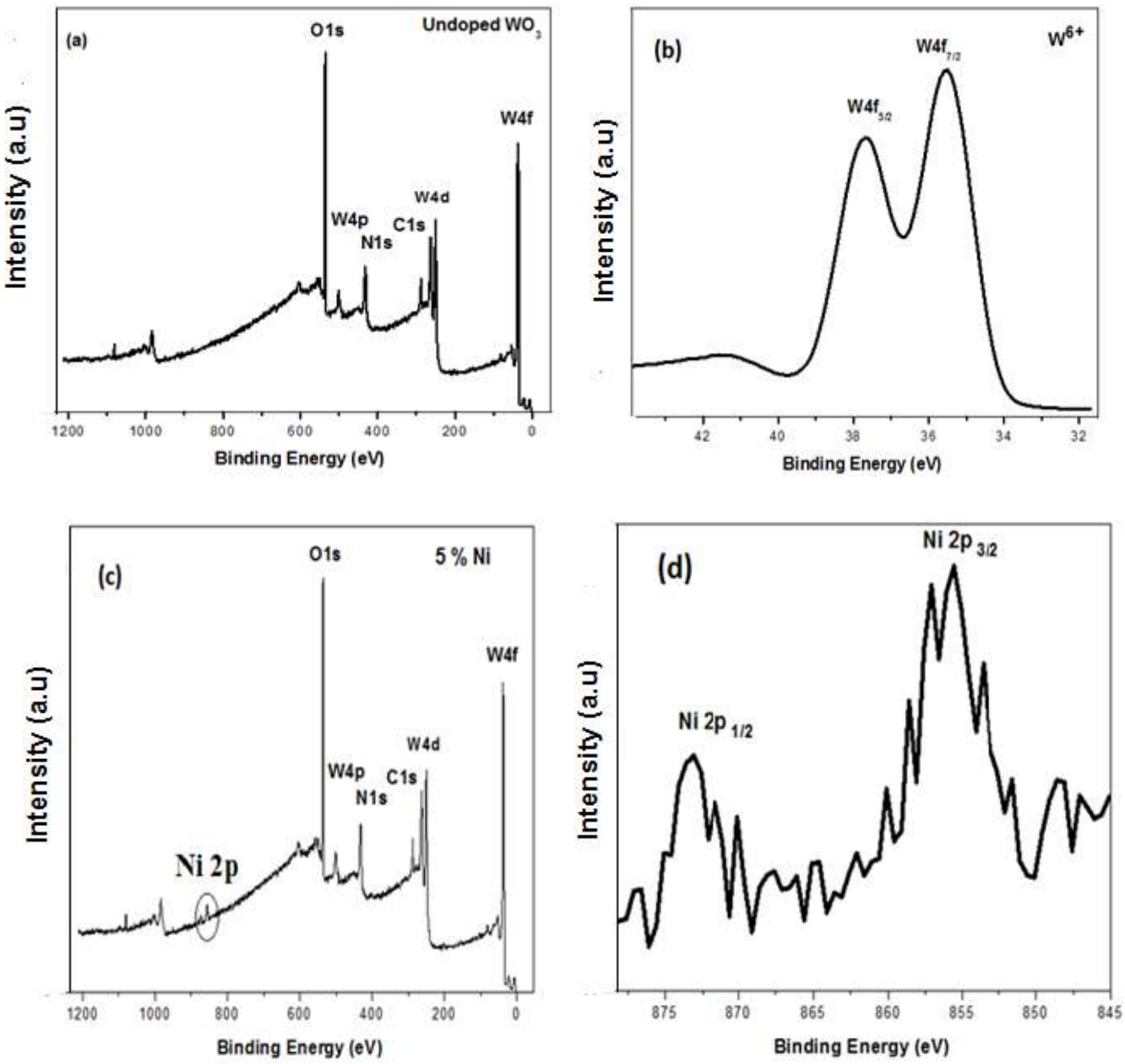

Figure 8.6 XPS spectra of **(a)** undoped WO_3 nanoplates **(b)** core level spectra of undoped WO_3 nanoplates **(c)** 5% Ni doped WO_3 nanoplates **(d)** Zoom plot of Ni 2p

8.2.5 Diffuse reflectance spectroscopic studies

Figure 8.7 depicts DRS spectra of undoped and Ni doped WO_3 nanoplates, recorded from 200 to 900 nm. Typical excitons bandgap absorption of undoped WO_3 nanoplates was found to be 495 nm. There is a red-shift compared to the bulk WO_3 (470 nm) [206]. Moreover, with the increase in Ni concentration, the band edge peak further shifts towards the higher wavelength. The band gap energies of the nanoplates were calculated using Kubelka-Munk relation [206]. The undoped WO_3 nanoplates has 2.50 eV energy band gap which is further reduced to 2.32eV with 8 % Ni doping [207].

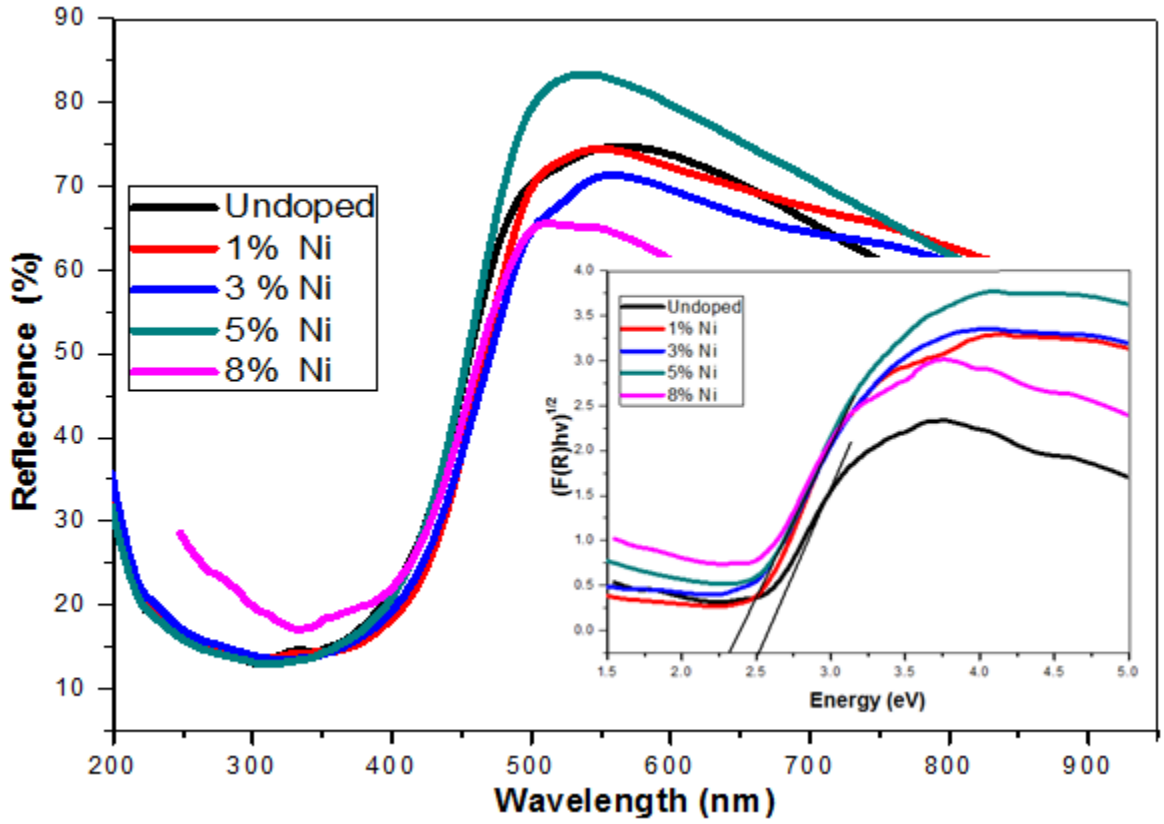

Figure 8.7 DRS spectra of undoped and Ni doped WO_3 nanoplates.

8.2.6 Photoluminescence spectra investigations

Photoluminescence (PL) spectrum is a vital technique to study the surface processes involving photogenerated electron hole pairs. The peak found at 420 nm may be allocated as NBE. The high intensity green emission peak found at 536 nm is related to defects [145, 235, 236, 238, 239].

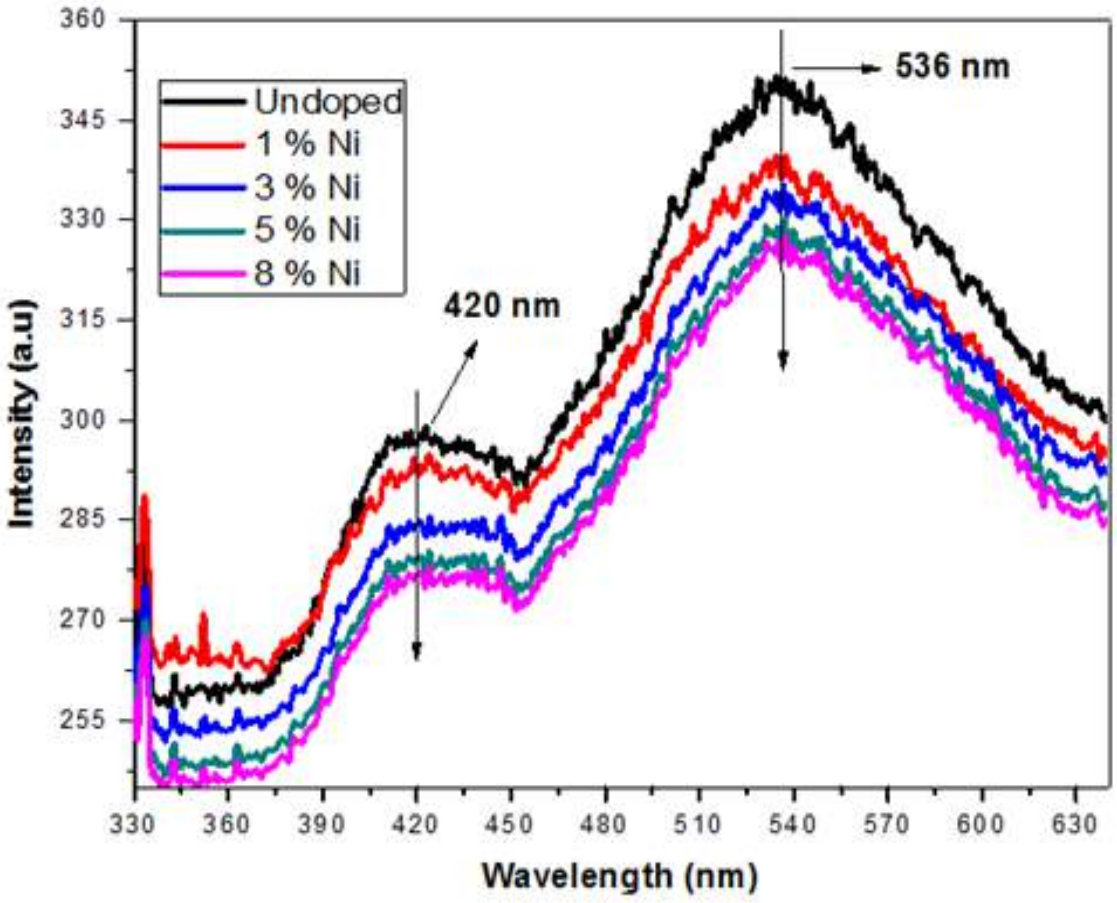

Figure 8.8 PL spectra of undoped and Ni doped WO_3 nanoplates

8.2.7 Dielectric and electrical characteristics

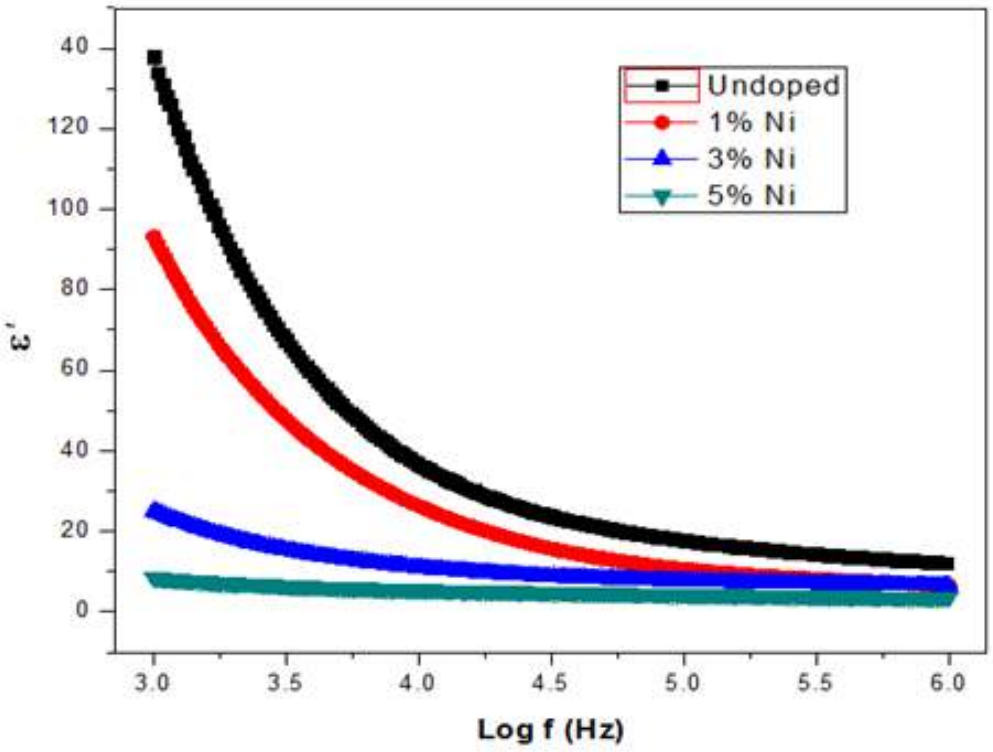

Figure 8.9 dielectric constant (ε').

The ε' decrease with Ni doping due to decrease in the polarization owing to difference in electronegativity of Ni (1.91) and W (2.36) [152]. Figure 8.10 depicts the dielectric loss (ε'') of prepared samples [152]. The prepared samples are well related to the Koop's model [156]. The value of (ε'') also significantly decreases with Ni doping because of reduced electric polarization.

Figure 8.11 depicts frequency dependent σ_{ac} of the nanoplates [152]. These findings are well in accordance with the power law [152]. Furthermore, σ_{ac} also reduces markedly with the Ni doping. This may be because of the doping induced grain boundaries defects [157].

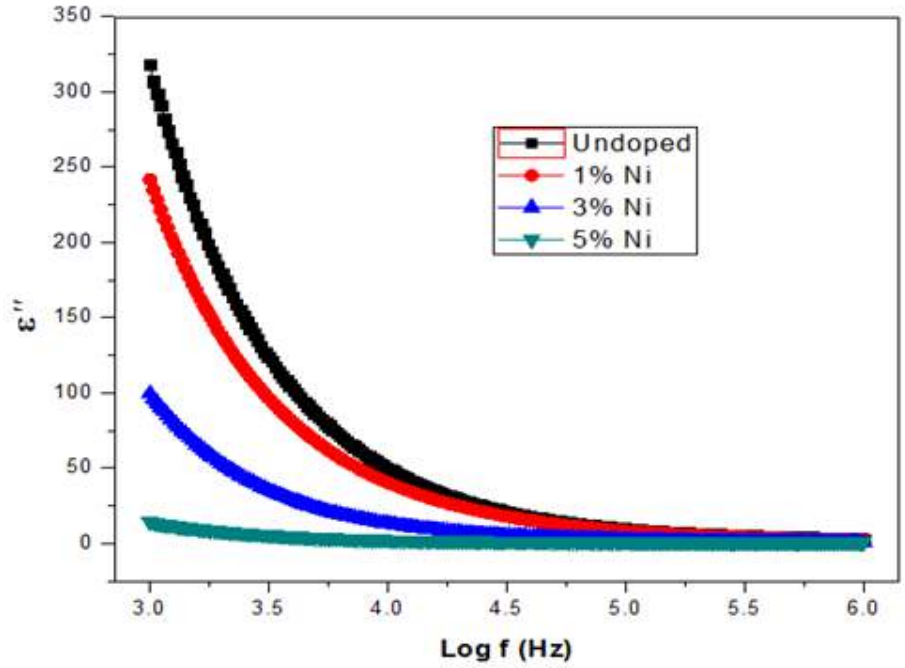

Figure 8.10 Variation of dielectric loss (ε'').

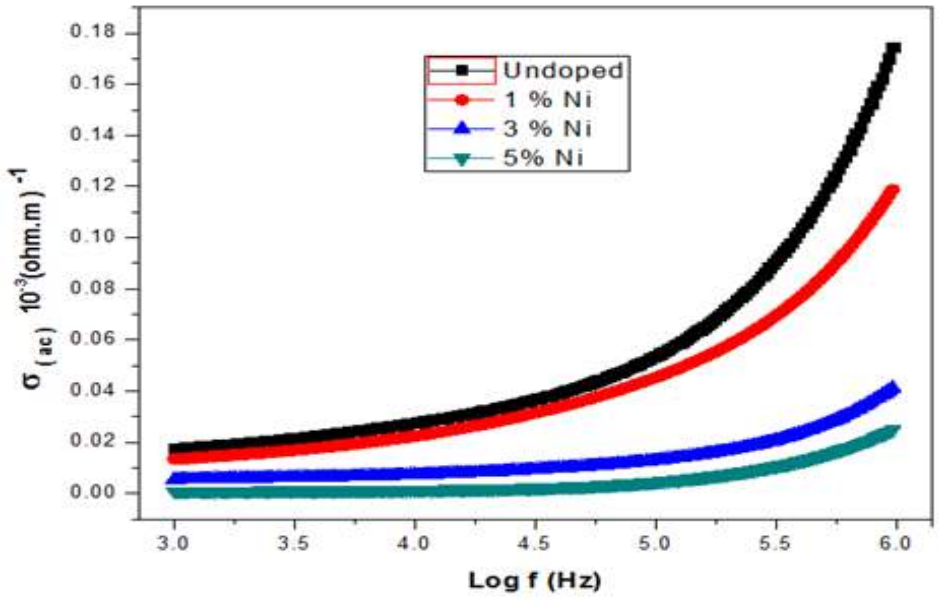

Figure 8.11 AC conductivity (σ_{ac}).

8.2.8 Visible light driven degradation of methyl red using undoped and Ni doped WO_3 nanoplates

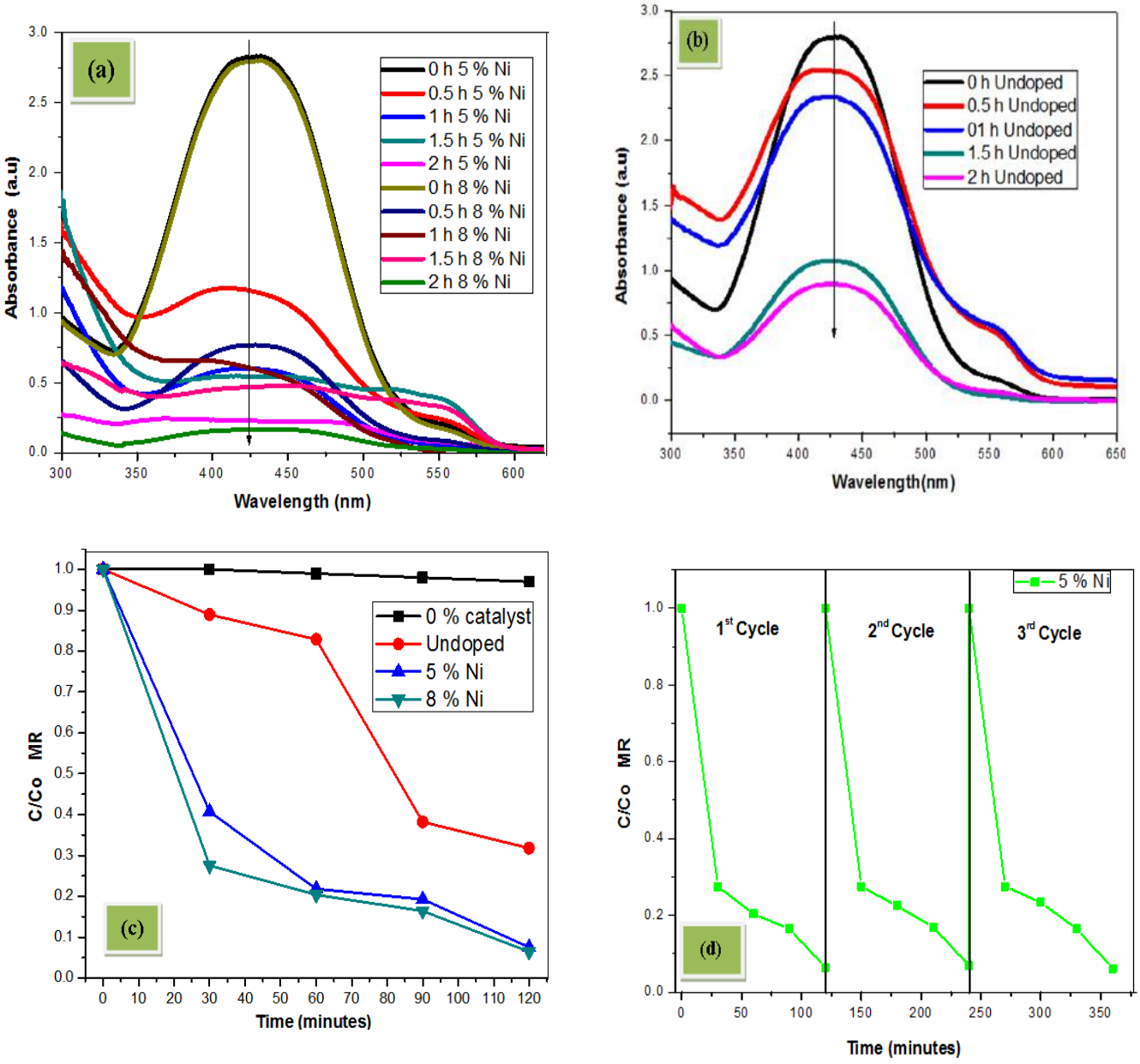

Figure 8.12 (a) Photodegradation of methyl red (MR) under visible light irradiation using Ni doped WO_3 nanoplates. **(b)** Photodegradation of MR under visible light illumination by undoped WO_3 nanoplates. **(c)** C/C_o versus time plot for the visible light driven photodegradation of MR using undoped and Ni doped WO_3 nanoplates. **(d)** The recyclability performance of 5% Ni doped WO_3 nanoplates.

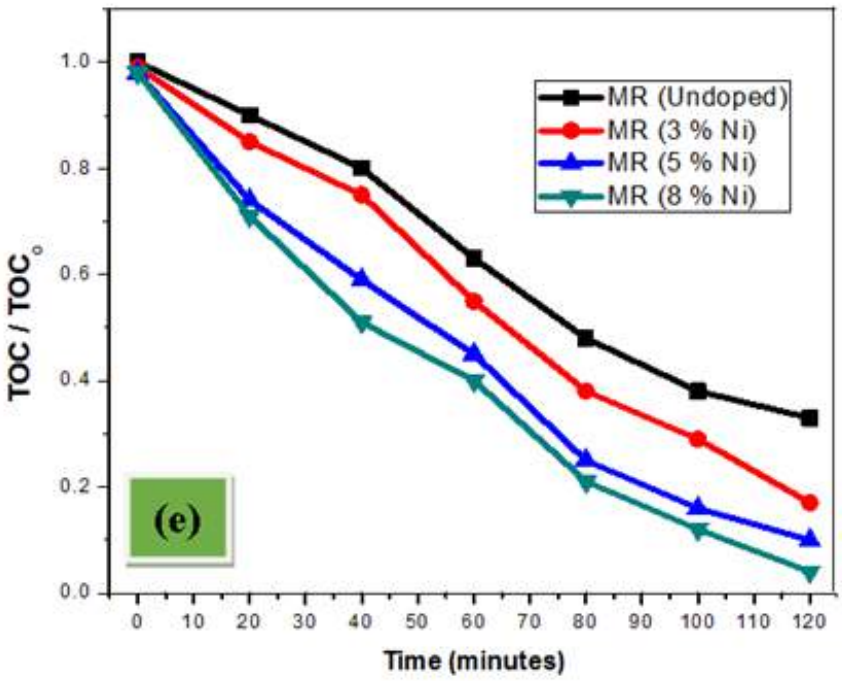

Figure 8.12 (e) Total organic carbon (TOC) removals from MR solutions during photocatalytic degradation by Ni doped WO_3 nanoplates.

The undoped WO_3 nanoplates have shown degradation of about 67 % of MR dye within 120 min. The photodegradation efficiency of methyl red further increased with nickel doping, which was evident by decrease in the characteristic MR peak intensity by 96% in 120 min when the degradation was done in the presence of Ni doped WO_3. The detailed mechanism is already explained.

In order to further demonstrate photocatalytic characteristics of the Ni doped WO_3 nanoplates, total organic carbon content (TOC) analysis has been performed. It can be seen from Figure 8.12 (e), that TOC gradually decreases with exposure time which hints the removal of organic carbon content when methyl red was treated with prepared nanoplates. The removal of TOC reached to 96% when methyl red was treated with 8% Ni doped WO_3 nanoplates after two hours [164].

8.2.9 Anticancer activities

The cytotoxicity of prepared Ni doped WO_3 nanoplates were examined against human breasts (MCF-7) and liver (Hep-2) cancer cells lines. The 20μg/ml dilutions of the synthesized Ni doped WO_3 nanoplates were applied against both cell lines for 24 hours in the presence of the visible light (LED). The detailed anticancer experimental setup was already discussed. Figure 8.13 depicts the percent cell viability of MCF-7 and Hep-2 cancers cells. The undoped WO_3 nanoplates have decreased the cells viability of MCF-7 and Hep-2 cancers cells by almost 63 % and 67% respectively. Interestingly, the cancer cells viability is further decreased using Ni doped WO_3 nanoplates. The cells viability were decreased about 30% against MCF-7 and 35% against Hep-2 cancers cells, treated with Ni doped WO_3 nanoplates. This shows Ni doped WO_3 nanomaterials may becomes a highly efficient anticancer agents and have better anti cancer cytotoxic activity than other reported metal oxides nanostructures. These doped WO_3 nanoplates have also been shown non toxic behavior towards ectocervical epithelial (HECE) healthy cells. The possible anticancer mechanism can be understood by the following arguments. The nanoparticles may attack to the redox active mitochondria which are considered to be the major site for ROS production in cells exposed to nanomaterials [28, 33, 34, 39, 40]. The increase in ROS generation with Ni doping into WO_3 nanoplates becomes a cause to reduce the percent cell viability of both cancerous cells and it may be understood on the fact that Ni doping could decrease the band gap energy of WO_3 (as shown in optical results) by leading higher visible light conversion efficiencies of the doped nanoplates. This may becomes a cause to higher electron hole pairs generations and ultimately resulting in higher ROS generation. As discussed earlier, the electron hole pair recombination rate decreases with Ni doping which also contribute to higher ROS generation. Therefore, Ni doped WO_3 nanostructures can produce ROS which may

result in apoptosis in cells via oxidative damage intercellular proteins, DNA and it leads to ultimately cell death.

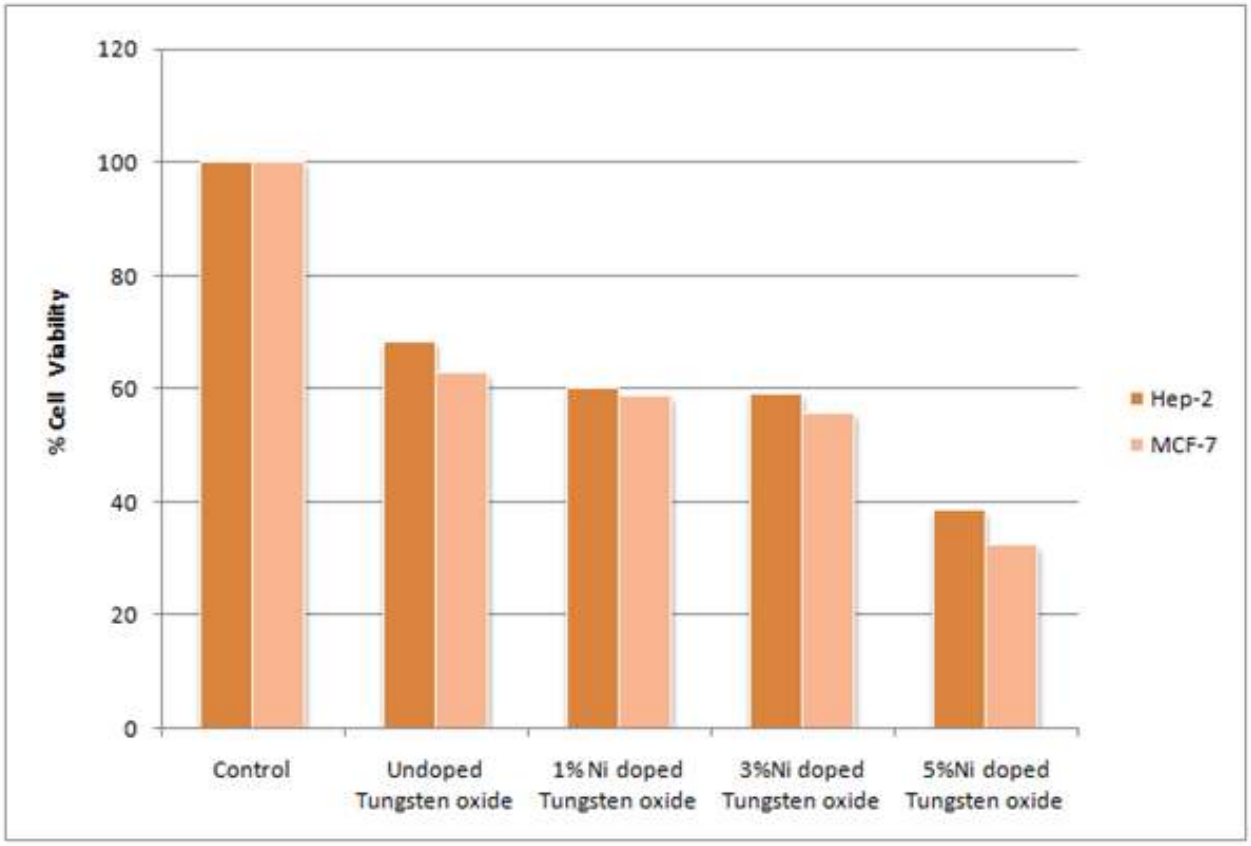

Figure 8.13 Effect of undoped and Ni doped WO_3 nanoplates on MCF-7 and Hep-2 cells viability

CHAPTER 9

CONCLUSIONS

The main objectives of this thesis were to synthesize undoped WO_3 nanostructures and then investigate the effects of various metals ions doping on the physical characteristics of WO_3 nanostructures. In order to achieve these objectives, five different dopants (Fe, Cu, Sn, Co and Ni) have been doped individually into WO_3 nanostructures by a facile wet-chemical method with controlled morphology. Their structural, morphological, compositional, vibrational, optical and electrical properties of undoped and doped WO_3 nanostructures have been analyzed through various characterization techniques.

Moreover, the undoped WO_3 nanoplates have shown strong visible light driven photodegradation activities against toxic organic industrial dye and anticancer activities in human cells. The optical (band gap), chemical (defects), electrical (dielectric), photocatalytic and biological (anticancer) properties have been tuned remarkably with selective metal ions chemical doping into WO_3 host matrix.

WO_3 nanostructures have been doped with Fe, Cu, Sn, Co and Ni metals ions. The detailed dopants induced effects have been concluded one by one as follows.

(i) Fe doping induced effects on WO_3 nanoplates

The summary of Fe doping induced effects on WO_3 nanoplates is described in Table 9.1. To conclude, Fe doped WO_3 nanoplates have been synthesized using a facile chemical co-precipitation method. Stable monoclinic phase has been verified for all samples through structural investigations indicating successful Fe doping. A shift in Raman peak positions towards lower wave number has been observed with Fe doping induced defects in WO_3.

Table 9.1 Effects Fe doping on WO_3 nanoplates

Characterizations and Applications	Undoped WO_3	1 % Fe doped WO_3	3 % Fe doped WO_3	5 % Fe doped WO_3	8 % Fe doped WO_3
XRD Phase	Monoclinic WO_3	Monoclinic WO_3 (No Fe/impurity peaks)	Monoclinic WO_3 (No Fe/impurity peaks)	Monoclinic WO_3 (No Fe peaks)	Monoclinic WO_3 (No Fe/impurity peaks)
SEM (Morphology)	Square nanoplates	Square nanoplates	Nanoplates	Nanoplates	Nanoplates
Energy Band gap (eV)	2.54 eV	2.47eV	2.39 eV	2.05 eV	2.02 eV
FTIR	Monoclinic WO_3	No Fe/impurity peaks detected	No Fe/impurity peaks detected	No Fe/impurity peaks detected	No Fe/impurity peaks detected
EDX	W and O peaks detected	Fe peaks detected	Fe peaks detected	Fe peaks detected	Fe peaks detected
XPS	Monoclinic WO_3 ($W6^{+}$) peaks detected		Fe peak detected Fe^{3+}	Fe peaks detected Fe^{3+}	
PL	Defects peak detected	Defects peak detected	Defects peak detected	Defects peak detected	Defects peak detected
Raman	Monoclinic WO_3	No Fe/impurity peaks detected	No Fe/ peaks detected	No Fe/impurity peaks detected	No Fe/impurity peaks detected
Dielectric constant	140	78	55	30	5
Dielectric loss	325	200	135	115	2
AC conductivity 10^{-3}ohm.m $^{-1}$	0.18	0.1	0.08	0.068	0.018
Photocatalytic activity	67 % (Methyl Red)	70 % (Methyl Red)	76% (Methyl Red)	90% (Methyl Red)	94% (Methyl Red)
Anti Breast cancer activity (MCF-7)	62 (Cell Viability)	58 (Cell Viability)	56(Cell Viability)	52(Cell Viability)	47 (Cell Viability)
Anti liver cancer activity (Hep-2)	67 (Cell Viability)	56 (Cell Viability)	57 (Cell Viability)	52(Cell Viability)	51 (Cell Viability)

A significant narrowing of the optical band gap of nanoplates has been found with the Fe doping which is linked to the hybridization between Fe 3d orbital and the O2p orbital. The electron hole pair recombination rates have been decreased via Fe doping. The particle size and crystal defects have been played significant role to tune the dielectric constant and electrical conductivity of doped samples. Furthermore, the visible light driven photocatalytic degradation activities of WO_3 nanoplates have been increased up to 94% with Fe doping due to the defects. Finally, the percent cell viability of MCF-7 and Hep-2 cancerous cells have also been found to decrease remarkably with Fe doping in WO_3 nanoplates.

(ii) **Sn doping induced effects on WO_3 nanoplates**

The summary of Sn doping induced effects on WO_3 nanoplates is described in Table 9.2. In conclusion, the chemical co-precipitation technique has been successfully employed to get desired Sn doped WO_3 nanoplates. The structural investigations have clearly confirmed the single phase monoclinic crystal structure of undoped and Sn doped WO3 nanostructures with plenty of defects. The average crystallite size, particle size and morphology of WO_3 nanoplates have been found to be strongly dependent on the Sn doping concentration into host matrix. The optical band gap has been tailored up to a blue shift of 0.08 eV as function of Sn doping into WO_3 nanostructures which is assigned due to the higher presence of impurity induced defects. It has been interestingly found that the particle size and crystal defects have vital part to tune the dielectric constant and electrical conductivity of doped samples. The visible light driven photocatalytic degradation activities of WO_3 nanoplates have been increased up to 83% with Sn doping. Moreover, the prepared nanoplates have been observed to be excellent candidate for anticancer applications as anticancer activity of WO_3 nanoplates is significantly enhanced with

Sn doping against MCF-7 cancerous cells. This can be probably due to a higher level of ROS production owing to the small particle size and higher defects densities of doped nanostructures.

Table 9.2 Effects Sn doping on WO_3 nanoplates

Characterizations and Applications	Undoped WO_3	1 % Sn doped WO_3	3 % Sn doped WO_3	5 % Sn doped WO_3	8 % Sn doped WO_3
XRD Phase	Monoclinic WO_3	Monoclinic WO_3 (No Sn/impurity peaks)	Monoclinic WO_3 (No Sn/impurity peaks)	Monoclinic WO_3 (No Sn peaks)	Monoclinic WO_3 (No Sn/impurity peaks)
SEM (Morphology)	Square nanoplates	Square nanoplates	Nanoplates)	Nanoparticles and Nanoplates	Nanoparticles
FTIR	Monoclinic WO_3	No Sn/impurity peaks detected	No Sn/impurity peaks detected	No Sn/impurity peaks detected	No Sn/impurity peaks detected
EDX	W and O peaks detected	Sn peaks detected	Sn peaks detected	Sn peaks detected	Sn peaks detected
PL	Defects peak detected	Defects peak detected	Defects peak detected	Defects peak detected	Defects peak detected
Raman	Monoclinic WO_3	No Sn/impurity peaks detected	No Sn/ peaks detected	No Sn/impurity peaks detected	No Sn/impurity peaks detected
Dielectric constant	140	41	30	20	18
Dielectric loss	325	275	120	75	73
AC conductivity 10^{-3}ohm.m $^{-1}$	0.18	0.12	0.05	0.02	0.02
Photocatalytic activity	67 % (Methyl Red)	70 % (Methyl Red)	78% (Methyl Red)	83% (Methyl Red)	83% (Methyl Red)
Anti Breast cancer activity (MCF-7)	73 (Cell Viability)	60 (Cell Viability)	58(Cell Viability)	57(Cell Viability)	56 (Cell Viability)

(i) **Cu doping induced effects on WO_3 nanoplates**

Table 9.3 Effects Cu doping on WO_3 nanoplates

Characterizations and Applications	Undoped WO_3	1 % Cu doped WO_3	3 % Cu doped WO_3	5 % Cu doped WO_3	8 % Cu doped WO_3
XRD Phase	Monoclinic WO_3	Monoclinic WO_3 (No Cu/impurity peaks)	Monoclinic WO_3 (No Cu/impurity peaks)	Monoclinic WO_3 (No Cu peaks)	Monoclinic WO_3 (No Cu/impurity peaks)
SEM (Morphology)	Square nanoplates	Square nanoplates	Nanoplates	Nanoplates	Nanoplates
Energy Band gap (eV)	2.54 eV	2.21 eV	2.19 eV	2.37 eV	2.15 eV
FTIR	Monoclinic WO_3	No Cu/impurity peaks detected	No Cu/impurity peaks detected	No Cu /impurity peaks detected	No Cu/impurity peaks detected
EDX	W and O peaks detected	Cu peaks detected	Cu peaks detected	Cu peaks detected	Cu peaks detected
PL	Defects peak detected	Defects peak detected	Defects peak detected	Defects peak detected	Defects peak detected
Raman	Monoclinic WO_3	No Cu/impurity peaks detected	No Cu/ peaks detected	No Cu/impurity peaks detected	No Cu/impurity peaks detected
Dielectric constant	140	78	40	35	30
Dielectric loss	325	300	200	135	50
AC conductivity 10^{-3}ohm.m $^{-1}$	0.18	0.1	0.09	0.06	0.045
Photocatalytic activity	67 % (Methyl Red)	70 % (Methyl Red)	75% (Methyl Red)	80% (Methyl Red)	80% (Methyl Red)
Anti cancer activity (MCF-7), (Hep-2) %	62 (MCF-7) 62(Hep-2)	64(MCF-7) 80(Hep-2)	63 (MCF-7) 78(Hep-2)	62(MCF-7) 70(Hep-2)	60 (MCF-7) 65(Hep-2)
Healthy cell (HECE)	Small effect	No effect	No effect	No effect	No effect

The summary of Cu doping induced effects on WO_3 nanoplates is described in Table 9.3. The Cu doped WO_3 nanoplates have been successfully synthesized by a facile chemical co-precipitation method. The monoclinic crystal structural nature has been confirmed for all prepared samples via structural investigations. The 2-D nanoplate morphology is observed for all samples. A significant energy band gap reduction is found in visible region with Cu doping. Furthermore, the defects density has been found to increase with the doping in all prepared nanoplates. The dielectric constant and electrical conductivity of doped samples has been changed with doping due to variation in particle size and crystal defects. Furthermore, the photodegradation activities of WO_3 nanoplates have been enhanced up to 80% with Cu doping. It is interestingly observed that the percent cell viability for the MCF-7 and the Hep-2 cancers cells has been decreased down to 60% and 65%, respectively without affecting the HECE human healthy cells by treating with Cu doped WO_3 nanoplates. This makes Cu doped WO_3 nanoplates a promising biocompatible anticancer agent for MCF-7 and Hep-2 cancers cells.

(i) **Co doping induced effects on WO_3 nanoplates**

The summary of Co doping induced effects on WO_3 nanoplates is described in Table 9.4. The Co doped WO_3 nanoplates have prepared via chemical route. Successful Co doping has been confirmed through structural investigations. The nanoplate like morphology has been observed for all samples. The optical bandgap experienced a red shift due to the Co doping into WO_3 nanoplates owing to the presence of large number of impurity defects. Furthermore, the recombination rate of photo induced electron hole pair has been decreased with Co doping. Dielectric properties have been significantly altered with Co doping. Photodegradation activities of methyl red have been found to increase up to 90% in 2 h with Co doped WO_3 nanoplates under visible light irradiations which is attributed to band gap narrowing and defects.

Table 9.4 Effects Co doping on WO_3 nanoplates

Characterizations and Applications	Undoped WO_3	1 % Co doped WO_3	3 % Co doped WO_3	5 % Co doped WO_3	8 % Co doped WO_3
XRD Phase	Monoclinic WO_3	Monoclinic WO_3 (No Co/impurity peaks)	Monoclinic WO_3 (No Co/impurity peaks)	Monoclinic WO_3 (No Co peaks)	Monoclinic WO_3 (Co peaks indicated)
SEM (Morphology)	Square nanoplates	Square nanoplates	Nanoplates	Nanoplates	Nanoplates
Energy Band gap(eV)	2.40 eV	2.38eV	2.26 eV	2.25 eV	2.15 eV
FTIR	Monoclinic WO_3	No Co/impurity peaks detected	No Co/impurity peaks detected	No Co/impurity peaks detected	No Co/impurity peaks detected
EDX / XPS	W and O peaks detected	Co peaks detected	Co peaks detected	Co peaks detected	Co peaks detected
PL	Defects peak detected	Defects peak detected	Defects peak detected	Defects peak detected	Defects peak detected
Raman	Monoclinic WO_3	No Co/impurity peaks detected	No Co/ peaks detected	No Co/impurity peaks detected	No Co/impurity peaks detected
Dielectric constant	140	90	79	40	38
Dielectric loss	325	320	275	142	138
AC conductivity 10^{-3}ohm.m $^{-1}$	0.18	0.1	0.082	0.076	0.074
Photocatalytic activity	67 % (Methyl Red)	70 % (Methyl Red)	78% (Methyl Red)	90% (Methyl Red)	90% (Methyl Red)
Anti Breast cancer activity (MCF-7) %	66 (Cell Viability)	64(Cell Viability)	63(Cell Viability)	61(Cell Viability)	60 (Cell Viability)
Anti liver cancer activity (Hep-2) %	70 (Cell Viability)	68 (Cell Viability)	63(Cell Viability)	62(Cell Viability)	61 (Cell Viability)

Moreover, the percent cell viability of MCF-7 and Hep-2 cancers cells, when treated with 8% Co doped WO_3 nanoplates, have been decreased up to 40%. This shows that Co doped WO_3 nanoplates can be considered as a promising visible light driven photocatalyst for rapid dye degradation as well as a promising anti cancer agent for MCF-7 and Hep-2 cancers cells.

(ii) **Ni doping induced effects on WO_3 nanoplates**

The summary of Ni doping induced effects on WO_3 nanoplates is described in Table 9.5. In Ni doped WO_3 nanoplates, the single phase monoclinic crystal structure has been confirmed through structural investigations. The optical band gap has been reduced with Ni doping due to the generation of impurity defects between valance and conduction bands. The recombination rate of photo induced electron hole pair has been decreased with Ni doping. The dielectric constant and electrical conductivity of the doped nanoplates has been modified significantly with Ni doping. Furthermore, the visible light driven photocatalytic degradation activities of WO_3 nanoplates have been enhanced up to 96% with Ni doping. Finally, the percent cell viability of MCF-7 and Hep-2 cancerous cells have also been found to decrease remarkably up to 30% and 35 % with Ni doping in WO_3 nanoplates.

Table 9.5 Effects Ni doping on WO_3 nanoplates

Characterizations and Applications	Undoped WO_3	1 % Ni doped WO_3	3 % Ni doped WO_3	5 % Ni doped WO_3	8 % Ni doped WO_3
XRD Phase	Monoclinic WO_3	Monoclinic WO_3 (No Ni / impurity peaks)	Monoclinic WO_3 (No Ni/impurity peaks)	Monoclinic WO_3 (No Ni /impurity peaks)	Monoclinic WO_3 (No Ni / impurity peaks)
SEM (Morphology)	Square nanoplates	Nanoplates	Nanoplates	Nanoplates	Nanoplates
Energy Band gap(eV)	2.54 eV	2.40 eV	2.34 eV	2.33 eV	2.32 eV
FTIR	Monoclinic WO_3	No Ni/impurity peaks detected	No Ni /impurity peaks detected	No Ni/impurity peaks detected	No Ni/impurity peaks detected
EDX	W and O peaks detected	Ni peaks detected	Ni peaks detected	Ni peaks detected	Ni peaks detected
XPS	Monoclinic WO_3 peaks detected		Ni peaks detected	Ni peaks detected	
PL	Defects peak detected	Defects peak detected	Defects peak detected	Defects peak detected	Defects peak detected
Raman	Monoclinic WO_3	No Ni/impurity peaks detected	No Ni peaks detected	No Ni/impurity peaks detected	No Ni/impurity peaks detected
Dielectric constant	140	95	26	9	8
Dielectric loss	325	245	110	18	16
AC conductivity 10^{-3}ohm.m $^{-1}$	0.18	0.12	0.04	0.017	0.016
Photocatalytic activity	67 % (Methyl Red)	79%	85%	92%	96%
Anti Breast cancer activity (MCF-7)	63 (Cell Viability)	58 (Cell Viability)	54 (Cell Viability)	30 (Cell Viability)	30 (Cell Viability)
Anti liver cancer activity (Hep-2)	67 (Cell Viability)	60 (Cell Viability)	58 (Cell Viability)	35 (Cell Viability)	35 (Cell Viability)

In final thesis conclusion, the physical, chemical, and biological properties have been tuned and enhanced with all dopants. The overall observed trends for visible light driven photodegradation activities of methyl red with transition metal dopants are achieved in the following sequence as WO_3 < Cu doped WO_3 < Sn doped WO_3 < Co doped WO_3 < Fe doped WO_3 < Ni doped WO_3. The tendencies of anticancer activities of MCF-7 cells with doping are given as follows WO_3 < Co doped WO_3 < Cu doped WO_3 < Sn doped WO_3 < Fe doped WO_3 < Ni doped WO_3 and anticancer activities of HEP-2 with doping are obtained as follows WO_3 < Co doped WO_3 < Cu doped WO_3 < Fe doped WO_3 < Ni doped WO_3.

References:

1. Singh, N.A., *Nanotechnology innovations, industrial applications and patents.* Environmental Chemistry Letters, 2017. **15**(2): p. 185-191.

2. Kennedy, D.R., M. Ritchie, and J. Mackenzie, *The photosorption of oxygen and nitric oxide on titanium dioxide.* Transactions of the Faraday Society, 1958. **54**: p. 119-129.

3. Palmisano, G., et al., *Photocatalysis: a promising route for 21st century organic chemistry.* Chemical Communications, 2007(33): p. 3425-3437.

4. Wada, Y., H. Yin, and S. Yanagida, *Environmental remediation using catalysis driven under electromagnetic irradiation.* Catalysis surveys from Japan, 2002. **5**(2): p. 127-138.

5. McNeil, S.E., *Nanotechnology for the biologist.* Journal of leukocyte biology, 2005. **78**(3): p. 585-594.

6. Nel, A., et al., *Toxic potential of materials at the nanolevel.* science, 2006. **311**(5761): p. 622-627.

7. Davids, L. and B. Kleemann, *Combating melanoma: the use of photodynamic therapy as a novel, adjuvant therapeutic tool.* Cancer treatment reviews, 2011. **37**(6): p. 465-475.

8. Murphy, G., *Sunblocks: mechanisms of action.* Photodermatology, photoimmunology & photomedicine, 1999. **15**(1): p. 34-36.

9. Hanley, C., et al., *Preferential killing of cancer cells and activated human T cells using ZnO nanoparticles.* Nanotechnology, 2008. **19**(29): p. 295103.

10. Wang, H., et al., *Fluorescent dye encapsulated ZnO particles with cell-specific toxicity for potential use in biomedical applications.* Journal of Materials Science: Materials in Medicine, 2009. **20**(1): p. 11.

11. Adhikari, S., D. Sarkar, and G. Madras, *Highly efficient WO_3 –ZnO mixed oxides for photocatalysis.* RSC Advances, 2015. **5**(16): p. 11895-11904.

12. Clark, A.J. and H.R. Petty, *WO_3/Pt nanoparticles promote light-induced lipid peroxidation and lysosomal instability within tumor cells.* Nanotechnology, 2016. **27**(7): p. 075103.

13. Patzke, G.R., F. Krumeich, and R. Nesper, *Oxidic nanotubes and nanorods—anisotropic modules for a future nanotechnology.* Angewandte Chemie International Edition, 2002. **41**(14): p. 2446-2461.

14. Patzke, G.R., et al., *Oxide nanomaterials: synthetic developments, mechanistic studies, and technological innovations.* Angewandte Chemie International Edition, 2011. **50**(4): p. 826-859.

15. Ferrari, M., *Cancer nanotechnology: opportunities and challenges.* Nature Reviews Cancer, 2005. **5**(3): p. 161-171.

16. Xia, T., et al., *Comparison of the abilities of ambient and manufactured nanoparticles to induce cellular toxicity according to an oxidative stress paradigm.* Nano letters, 2006. **6**(8): p. 1794-1807.

17. Guo, D., et al., *Synergistic cytotoxic effect of different sized ZnO nanoparticles and daunorubicin against leukemia cancer cells under UV irradiation.* Journal of Photochemistry and Photobiology B: Biology, 2008. **93**(3): p. 119-126.

18. Kubota, Y., et al., *Photokilling of T-24 human bladder cancer cells with titanium dioxide.* British journal of cancer, 1994. **70**(6): p. 1107-1111.

19. Nair, S., et al., *Role of size scale of ZnO nanoparticles and microparticles on toxicity toward bacteria and osteoblast cancer cells.* Journal of Materials Science: Materials in Medicine, 2009. **20**(1): p. 235.

20. Zhang, Y., et al., *Phototoxicity of zinc oxide nanoparticle conjugatesin human ovarian cancer NIH: OVCAR-3 cells.* Journal of Biomedical Nanotechnology, 2008. **4**(4): p. 432-438.

21. Abbas, F., et al., *Facile synthesis of ferromagnetic Ni doped CeO_2 nanoparticles with enhanced anticancer activity.* Applied Surface Science, 2015. **357**: p. 931-936.

22. Colmenares, J.C., et al., *Nanostructured photocatalysts and their applications in the photocatalytic transformation of lignocellulosic biomass: an overview.* Materials, 2009. **2**(4): p. 2228-2258.

23. Hunge, Y., et al., *Photoelectrocatalytic degradation of methyl red using sprayed WO_3 thin films under visible light irradiation.* Journal of Materials Science: Materials in Electronics, 2015. **26**(11): p. 8404-8412.

24. Zhu, W., et al., *Ag loaded WO_3 nanoplates for efficient photocatalytic degradation of sulfanilamide and their bactericidal effect under visible light irradiation.* Journal of hazardous materials, 2016. **318**: p. 407-416.

25. Fox, M.A. and M.T. Dulay, *Heterogeneous photocatalysis.* Chemical reviews, 1993. **93**(1): p. 341-357.

26. Boyle, P. and B. Levin, *World cancer report 2008*. 2008: IARC Press, International Agency for Research on Cancer.

27. Ferlay, J., et al., *Estimates of the cancer incidence and mortality in Europe in 2006.* Annals of oncology, 2007. **18**(3): p. 581-592.

28. Wahab, R., et al., *ZnO nanoparticles induced oxidative stress and apoptosis in HepG2 and MCF-7 cancer cells and their antibacterial activity.* Colloids and Surfaces B: Biointerfaces, 2014. **117**: p. 267-276.

29. Ott, M., et al., *Mitochondria, oxidative stress and cell death.* Apoptosis, 2007. **12**(5): p. 913-922.

30. Cai, R., et al., *Photokilling of malignant cells with ultrafine TiO_2 powder.* Bulletin of the Chemical Society of Japan, 1991. **64**(4): p. 1268-1273.

31. Cai, R., et al., *Induction of cytotoxicity by photoexcited TiO_2 particles.* Cancer research, 1992. **52**(8): p. 2346-2348.

32. Bakalova, R., et al., *Quantum dots as photosensitizers?* Nature biotechnology, 2004. **22**(11): p. 1360-1361.

33. Ostrovsky, S., et al., *Selective cytotoxic effect of ZnO nanoparticles on glioma cells.* Nano Research, 2009. **2**(11): p. 882-890.

34. Chang, E., et al., *Evaluation of quantum dot cytotoxicity based on intracellular uptake.* Small, 2006. **2**(12): p. 1412-1417.

35. Fang, X., et al., *Stresses exerted by ZnO, CeO_2 and anatase TiO_2 nanoparticles on the Nitrosomonas europaea.* Journal of colloid and interface science, 2010. **348**(2): p. 329-334.

36. Kim, I.-S., M. Baek, and S.-J. Choi, *Comparative cytotoxicity of Al_2O_3, CeO_2, TiO_2 and ZnO nanoparticles to human lung cells.* Journal of nanoscience and nanotechnology, 2010. **10**(5): p. 3453-3458.

37. Kuang, Y., et al., *Comparison study on the antibacterial activity of nano-or bulk-cerium oxide.* Journal of nanoscience and nanotechnology, 2011. **11**(5): p. 4103-4108.

38. Ahamed, M., et al., *Selective killing of cancer cells by iron oxide nanoparticles mediated through reactive oxygen species via p53 pathway.* Journal of nanoparticle research, 2013. **15**(1): p. 1225.

39. Xia, T., et al., *Comparison of the mechanism of toxicity of zinc oxide and cerium oxide nanoparticles based on dissolution and oxidative stress properties.* ACS nano, 2008. **2**(10): p. 2121-2134.

40. Alarifi, S., et al., *Iron oxide nanoparticles induce oxidative stress, DNA damage, and caspase activation in the human breast cancer cell line.* Biological trace element research, 2014. **159**(1-3): p. 416-424.

41. Bennett, S.W. and A.A. Keller, *Comparative photoactivity of CeO_2, γ-Fe_2O_3, TiO_2 and ZnO in various aqueous systems.* Applied Catalysis B: Environmental, 2011. **102**(3): p. 600-607.

42. Asati, A., et al., *Surface-charge-dependent cell localization and cytotoxicity of cerium oxide nanoparticles.* ACS nano, 2010. **4**(9): p. 5321-5331.

43. Mittal, S. and A.K. Pandey, *Cerium oxide nanoparticles induced toxicity in human lung cells: role of ROS mediated DNA damage and apoptosis.* BioMed research international, 2014. **2014**.

44. Deb, S.K., *Opportunities and challenges in science and technology of WO_3 for electrochromic and related applications.* Solar Energy Materials and Solar Cells, 2008. **92**(2): p. 245-258.

45. Roussel, P., P. Labbe, and D. Groult, *Symmetry and twins in the monophosphate tungsten bronze series (PO2) 4 (WO_3) 2m ($2 \leq m \leq 14$).* Acta Crystallographica Section B: Structural Science, 2000. **56**(3): p. 377-391.

46. Woodward, P., A. Sleight, and T. Vogt, *Ferroelectric tungsten trioxide.* Journal of Solid State Chemistry, 1997. **131**(1): p. 9-17.

47. Zhu, K., et al., *Crystalline WO_3 nanowires synthesized by templating method.* Chemical Physics Letters, 2003. **377**(3): p. 317-321.

48. Salje, E.K., et al., *Crystal structure and paramagnetic behaviour of.* Journal of Physics: Condensed Matter, 1997. **9**(31): p. 6563.

49. Desre, P., *A thermodynamic model for the nanocrystal to glass transition of intermetallic compounds subjected to high deformation by mechanical attrition—Application to L12 phases.* Nanostructured materials, 1997. **8**(6): p. 687-701.

50. Boulova, M. and G. Lucazeau, *Crystallite nanosize effect on the structural transitions of WO_3 studied by Raman spectroscopy.* Journal of Solid State Chemistry, 2002. **167**(2): p. 425-434.

51. Polaczek, A., M. Pekala, and Z. Obuszko, *Magnetic susceptibility and thermoelectric power of tungsten intermediary oxides.* Journal of Physics: Condensed Matter, 1994. **6**(39): p. 7909.

52. Makarov, V. and M. Trontelj, *Sintering and electrical conductivity of doped WO_3.* Journal of the European Ceramic Society, 1996. **16**(7): p. 791-794.

53. Gillet, M., et al., *The structure and electrical conductivity of vacuum-annealed WO_3 thin films.* Thin Solid Films, 2004. **467**(1): p. 239-246.

54. Gullapalli, S., R. Vemuri, and C. Ramana, *Structural transformation induced changes in the optical properties of nanocrystalline tungsten oxide thin films.* Applied Physics Letters, 2010. **96**(17): p. 171903.

55. Chang, M.T., et al., *Nitrogen-doped tungsten oxide nanowires: Low-temperature synthesis on Si, and electrical, optical, and field-emission properties.* small, 2007. **3**(4): p. 658-664.

56. Hjelm, A., C.G. Granqvist, and J.M. Wills, *Electronic structure and optical properties of WO_3, $LiWO_3$, $NaWO_3$, and HWO_3.* Physical Review B, 1996. **54**(4): p. 2436.

57. Yoffe, A.D., *Low-dimensional systems: quantum size effects and electronic properties of semiconductor microcrystallites (zero-dimensional systems) and some quasi-two-dimensional systems.* Advances in Physics, 1993. **42**(2): p. 173-262.

58. May, R.A., et al., *Optical constants of electrodeposited mixed molybdenum− tungsten oxide films determined by variable-angle spectroscopic ellipsometry*. The Journal of Physical Chemistry C, 2007. **111**(49): p. 18251-18257.

59. Ihn, T., *Semiconductor nanostructures: Quantum states and electronic transport*. 2010: Oxford University Press.

60. Aguir, K., C. Lemire, and D. Lollman, *Electrical properties of reactively sputtered WO_3 thin films as ozone gas sensor.* Sensors and Actuators B: Chemical, 2002. **84**(1): p. 1-5.

61. Vemuri, R., et al., *Effect of structure and size on the electrical properties of nanocrystalline WO_3 films.* ACS applied materials & interfaces, 2010. **2**(9): p. 2623-2628.

62. Patel, K., et al., *Growth, structural, electrical and optical properties of the thermally evaporated tungsten trioxide (WO_3) thin films.* Materials Chemistry and Physics, 2009. **114**(1): p. 475-478.

63. Rui, H., Z. Jing, and Y. Rong, *Synthesis and electrical characterization of tungsten oxide nanowires.* Chinese Physics B, 2009. **18**(7): p. 3024.

64. Bakonyi, I., et al., *Structure and properties of fine-grained electrodeposited nickel.* Nanostructured Materials, 1993. **3**(1-6): p. 155-161.

65. Ramana, C., et al., *Growth and surface characterization of V_2O_5 thin films made by pulsed-laser deposition.* Journal of Vacuum Science & Technology A: Vacuum, Surfaces, and Films, 2004. **22**(6): p. 2453-2458.

66. Delichere, P., et al., *Electrochromism in anodic WO_3 films I: preparation and physicochemical properties of films in the virgin and coloured states.* Thin Solid Films, 1988. **161**: p. 35-46.

67. Li Bassi, A., et al., *Raman spectroscopy characterization of titania nanoparticles produced by flame pyrolysis: the influence of size and stoichiometry.* Journal of Applied Physics, 2005. **98**(7): p. 074305.

68. Karunagaran, B., et al., *Structural, optical and Raman scattering studies on DC magnetron sputtered titanium dioxide thin films.* Solar energy materials and solar cells, 2005. **88**(2): p. 199-208.

69. Fujishima, A. and K. Honda, *Electrochemical photolysis of water at a semiconductor electrode.* nature, 1972. **238**(5358): p. 37-38.

70. Zhang, H., G. Chen, and D.W. Bahnemann, *Photoelectrocatalytic materials for environmental applications.* Journal of Materials Chemistry, 2009. **19**(29): p. 5089-5121.

71. Alexander, B.D., et al., *Metal oxide photoanodes for solar hydrogen production.* Journal of Materials Chemistry, 2008. **18**(20): p. 2298-2303.

72. Ashokkumar, M., *An overview on semiconductor particulate systems for photoproduction of hydrogen.* International Journal of Hydrogen Energy, 1998. **23**(6): p. 427-438.

73. Meng, Z.-D., et al., *Preparation, characterization and photocatalytic behavior of WO_3-fullerene/TiO_2 catalysts under visible light.* Nanoscale research letters, 2011. **6**(1): p. 459.

74. Qamar, M., et al., *Enhanced photoelectrochemical and photocatalytic activity of WO_3-surface modified TiO_2 thin film.* Nanoscale research letters, 2015. **10**(1): p. 54.

75. Kalanur, S.S., et al., *Facile growth of aligned WO_3 nanorods on FTO substrate for enhanced photoanodic water oxidation activity.* Journal of Materials Chemistry A, 2013. **1**(10): p. 3479-3488.

76. Balandeh, M., et al., *Quasi-1D hyperbranched WO_3 nanostructures for low-voltage photoelectrochemical water splitting.* Journal of Materials Chemistry A, 2015. **3**(11): p. 6110-6117.

77. Arai, T., et al., *Complete oxidation of acetaldehyde and toluene over a Pd/WO_3 photocatalyst under fluorescent-or visible-light irradiation.* Chemical Communications, 2008(43): p. 5565-5567.

78. Fujishima, A., T.N. Rao, and D.A. Tryk, *Titanium dioxide photocatalysis.* Journal of Photochemistry and Photobiology C: Photochemistry Reviews, 2000. **1**(1): p. 1-21.

79. Hernandez-Uresti, D.B., et al., *Characterization and photocatalytic properties of hexagonal and monoclinic WO_3 prepared via microwave-assisted hydrothermal synthesis.* Ceramics International, 2014. **40**(3): p. 4767-4775.

80. Li, J., et al., *Microwave-assisted growth of $WO_3 \cdot 0.33\ H_2O$ micro/nanostructures with enhanced visible light photocatalytic properties.* CrystEngComm, 2013. **15**(39): p. 7904-7913.

81. Gondal, M., et al., *Photocatalytic removal of hazardous dye from water using nanostructured WO_3.* International Journal of Nanoparticles, 2011. **4**(1): p. 53-63.

82. He, X., et al., *Preparation and Improved Photocatalytic Activity of $WO_3 \cdot 0.33\ H_2O$ Nanonetworks.* Catalysis letters, 2012. **142**(5): p. 637-645.

83. Miseki, Y., et al., *Cs-modified WO_3 photocatalyst showing efficient solar energy conversion for O_2 production and Fe (III) ion reduction under visible light.* The Journal of Physical Chemistry Letters, 2010. **1**(8): p. 1196-1200.

84. Hameed, A., M. Gondal, and Z. Yamani, *Effect of transition metal doping on photocatalytic activity of WO_3 for water splitting under laser illumination: role of 3d-orbitals.* Catalysis Communications, 2004. **5**(11): p. 715-719.

85. Nah, Y.-C., et al., *Nitrogen doping of nanoporous WO_3 layers by NH3 treatment for increased visible light photoresponse.* Nanotechnology, 2010. **21**(10): p. 105704.

86. Ibhadon, A.O. and P. Fitzpatrick, *Heterogeneous photocatalysis: recent advances and applications.* Catalysts, 2013. **3**(1): p. 189-218.

87. Feng, C., S. Wang, and B. Geng, *Ti (iv) doped WO_3 nanocuboids: fabrication and enhanced visible-light-driven photocatalytic performance.* Nanoscale, 2011. **3**(9): p. 3695-3699.

88. Liu, H., et al., *Preparation and photocatalytic activity of dysprosium doped tungsten trioxide nanoparticles.* Materials Chemistry and Physics, 2007. **104**(2): p. 377-383.

89. Shi, J.-W., et al., *Influence of Fe^{3+} and Ho^{3+} co-doping on the photocatalytic activity of TiO_2.* Materials Chemistry and Physics, 2007. **106**(2): p. 247-249.

90. Shi, J.-w., *Preparation of Fe (III) and Ho (III) co-doped TiO_2 films loaded on activated carbon fibers and their photocatalytic activities.* Chemical Engineering Journal, 2009. **151**(1): p. 241-246.

91. Song, X.C., et al., *Preparation and photocatalytic activity of Mo-doped WO_3 nanowires.* Journal of Nanoparticle Research, 2010. **12**(8): p. 2813-2819.

92. Mu, W., et al., *Characterizations of Nb-doped WO_3 nanomaterials and their enhanced photocatalytic performance.* Rsc Advances, 2014. **4**(68): p. 36064-36070.

93. Santato, C., M. Ulmann, and J. Augustynski, *Enhanced visible light conversion efficiency using nanocrystalline WO_3 films.* Advanced Materials, 2001. **13**(7): p. 511-514.

94. Santato, C., M. Ulmann, and J. Augustynski, *Photoelectrochemical properties of nanostructured tungsten trioxide films.* The Journal of Physical Chemistry B, 2001. **105**(5): p. 936-940.

95. Kovendhan, M., et al., *Structural transition and blue emission in textured and highly transparent spray deposited Li doped WO_3 thin films.* Applied Surface Science, 2011. **257**(18): p. 8127-8133.

96. Cao, J., et al., *Photocatalytic activity of novel AgBr/WO_3 composite photocatalyst under visible light irradiation for methyl orange degradation.* Journal of hazardous materials, 2011. **190**(1): p. 700-706.

97. Turkez, H., et al., *The risk evaluation of tungsten oxide nanoparticles in cultured rat liver cells for its safe applications in nanotechnology*. Brazilian Archives of Biology and Technology, 2014. **57**(4): p. 532-541.

98. Yassin, A.M., et al., *Tungsten oxide nanoplates; the novelty in targeting metalloproteinase-7 gene in both cervix and colon cancer cells.* Applied biochemistry and biotechnology, 2016. **180**(4): p. 623-637.

99. Sadeghi, L., F. Tanwir, and V.Y. Babadi, *In vitro toxicity of iron oxide nanoparticle: Oxidative damages on Hep G2 cells.* Experimental and Toxicologic Pathology, 2015. **67**(2): p. 197-203.

100. Wani, K.D., et al., *Synthesis, characterization and in vitro study of biocompatible cinnamaldehyde functionalized magnetite nanoparticles (CPGF Nps) for hyperthermia and drug delivery applications in breast cancer.* PloS one, 2014. **9**(9): p. e107315.

101. Wang, F., C. Di Valentin, and G. Pacchioni, *Doping of WO_3 for photocatalytic water splitting: hints from density functional theory.* The Journal of Physical Chemistry C, 2012. **116**(16): p. 8901-8909.

102. Al-Mubaddel, F.S., et al., *Engineered nanostructures: A review of their synthesis, characterization and toxic hazard considerations.* Arabian Journal of Chemistry, 2012.

103. Cao, G., *Nanostructures and nanomaterials: Synthesis, properties and applications. 2004*. Imperial College Press.

104. Supothina, S., et al., *Synthesis of tungsten oxide nanoparticles by acid precipitation method.* Ceramics International, 2007. **33**(6): p. 931-936.

105. Han, X., et al., *Controlling the morphologies of WO_3 particles and tuning the gas sensing properties.* New Journal of Chemistry, 2012. **36**(11): p. 2205-2208.

106. Ma, J., et al., *Topochemical preparation of WO3 nanoplates through precursor H_2WO_4 and their gas-sensing performances.* The Journal of Physical Chemistry C, 2011. **115**(37): p. 18157-18163.

107. Wang, J. and C.j. Liu, *Preparation of 2D WO_3 nanomaterials with enhanced catalytic activities: Current status and perspective.* ChemBioEng Reviews, 2015. **2**(5): p. 335-350.

108. Zhang, H., et al., *Template-free facile preparation of monoclinic WO_3 nanoplates and their high photocatalytic activities.* Applied Surface Science, 2014. **305**: p. 274-280.

109. Lu, G. and X.S. Zhao, *Nanoporous materials: science and engineering*. Vol. 4. 2004: World Scientific.

110. Wang, J., et al., *Synthesis, assembly, and electrochromic properties of uniform crystalline WO3 nanorods.* The Journal of Physical Chemistry C, 2008. **112**(37): p. 14306-14312.

111. Gu, Z., et al., *Large-scale synthesis of single-crystal hexagonal tungsten trioxide nanowires and electrochemical lithium intercalation into the nanocrystals.* Journal of Solid State Chemistry, 2007. **180**(1): p. 98-105.

112. Mills, A., R.H. Davies, and D. Worsley, *Water purification by semiconductor photocatalysis.* Chemical Society Reviews, 1993. **22**(6): p. 417-425.

113. Lee, S.-Y. and S.-J. Park, *TiO 2 photocatalyst for water treatment applications.* Journal of Industrial and Engineering Chemistry, 2013. **19**(6): p. 1761-1769.

114. Chong, M.N., et al., *Recent developments in photocatalytic water treatment technology: a review.* Water research, 2010. **44**(10): p. 2997-3027.

115. Park, H., et al., *Surface modification of TiO_2 photocatalyst for environmental applications.* Journal of Photochemistry and Photobiology C: Photochemistry Reviews, 2013. **15**: p. 1-20.

116. Ochiai, T. and A. Fujishima, *Photoelectrochemical properties of TiO_2 photocatalyst and its applications for environmental purification.* Journal of Photochemistry and photobiology C: Photochemistry reviews, 2012. **13**(4): p. 247-262.

117. Li, J., et al., *Ag-based semiconductor photocatalysts in environmental purification.* Applied Surface Science, 2015. **358**: p. 46-56.

118. Cao, J., et al., *Thermodecomposition synthesis of WO_3/H_2WO_4 heterostructures with enhanced visible light photocatalytic properties.* Applied Catalysis B: Environmental, 2012. **111**: p. 288-296.

119. Peng, Y., et al., *The effect of SiO 2 on a novel CeO_2–WO_3/TiO_2 catalyst for the selective catalytic reduction of NO with NH_3.* Applied Catalysis B: Environmental, 2013. **140**: p. 276-282.

120. Rey, A., et al., *WO_3–TiO_2 based catalysts for the simulated solar radiation assisted photocatalytic ozonation of emerging contaminants in a municipal wastewater treatment plant effluent.* Applied Catalysis B: Environmental, 2014. **154**: p. 274-284.

121. Cole, B., et al., *Evaluation of nitrogen doping of tungsten oxide for photoelectrochemical water splitting.* The Journal of Physical Chemistry C, 2008. **112**(13): p. 5213-5220.

122. Liu, Y., et al., *Photoelectrochemical properties and photocatalytic activity of nitrogen-doped nanoporous WO_3 photoelectrodes under visible light.* Applied Surface Science, 2012. **258**(12): p. 5038-5045.

123. Sun, Y., et al., *Photoelectrochemical and structural characterization of carbon-doped WO_3 films prepared via spray pyrolysis.* International Journal of Hydrogen Energy, 2009. **34**(20): p. 8476-8484.

124. Takeuchi, M., et al., *Preparation of the visible light responsive N_3−doped WO_3 photocatalyst by a thermal decomposition of ammonium paratungstate.* Applied Catalysis B: Environmental, 2011. **110**: p. 1-5.

125. Hwang, D.W., et al., *Mg-doped WO_3 as a novel photocatalyst for visible light-induced water splitting.* Catalysis Letters, 2002. **80**(1): p. 53-57.

126. Karuppasamy, K.M. and A. Subrahmanyam, *Results on the electrochromic and photocatalytic properties of vanadium doped tungsten oxide thin films prepared by reactive dc magnetron sputtering technique.* Journal of Physics D: Applied Physics, 2008. **41**(3): p. 035302.

127. Seddigi, Z.S., *Removal of alizarin yellow dye from water using zinc doped WO_3 catalyst.* Bulletin of environmental contamination and toxicology, 2010. **84**(5): p. 564-567.

128. Tesfamichael, T., et al., *Gas sensing characteristics of Fe-doped tungsten oxide thin films.* Sensors and Actuators B: Chemical, 2012. **168**: p. 345-353.

129. Si, P., et al., *Synthesis, structure and magnetic properties of iron-doped tungsten oxide nanorods.* Physica B: Condensed Matter, 2007. **392**(1): p. 154-158.

130. Li, Z., et al., *Effect of Fe-doped TiO_2 nanoparticle derived from modified hydrothermal process on the photocatalytic degradation performance on methylene blue.* Journal of Hazardous Materials, 2008. **155**(3): p. 590-594.

131. Tong, T., et al., *Preparation of Fe^{3+}-doped TiO_2 catalysts by controlled hydrolysis of titanium alkoxide and study on their photocatalytic activity for methyl orange degradation.* Journal of Hazardous Materials, 2008. **155**(3): p. 572-579.

132. Lou, X.W.D., L.A. Archer, and Z. Yang, *Hollow micro-/nanostructures: Synthesis and applications.* Advanced Materials, 2008. **20**(21): p. 3987-4019.

133. Liu, Y., et al., *A magnetically separable photocatalyst based on nest-like γ-Fe_2O_3/ZnO double-shelled hollow structures with enhanced photocatalytic activity.* Nanoscale, 2012. **4**(1): p. 183-187.

134. Liu, Y., et al., *Magnetic-field induced formation of 1D Fe_3O_4/C/CdS coaxial nanochains as highly efficient and reusable photocatalysts for water treatment.* Journal of Materials Chemistry, 2011. **21**(45): p. 18359-18364.

135. Lin, Y., et al., *Nanonet-based hematite heteronanostructures for efficient solar water splitting.* Journal of the American Chemical Society, 2011. **133**(8): p. 2398-2401.

136. Wang, Q., et al., *Constructing ordered sensitized heterojunctions: bottom-up electrochemical synthesis of p-type semiconductors in oriented n-TiO_2 nanotube arrays.* Nano letters, 2009. **9**(2): p. 806-813.

137. Almquist, C.B. and P. Biswas, *Role of synthesis method and particle size of nanostructured TiO_2 on its photoactivity.* Journal of Catalysis, 2002. **212**(2): p. 145-156.

138. Ma, D., et al., *Self-assembled three-dimensional hierarchical umbilicate Bi_2WO_6 microspheres from nanoplates: controlled synthesis, photocatalytic activities, and wettability.* The Journal of Physical Chemistry C, 2009. **113**(11): p. 4369-4374.

139. Maeda, K., et al., *Nanoparticulate precursor route to fine particles of TaON and ZrO_2–TaON solid solution and their photocatalytic activity for hydrogen evolution under visible light.* Applied Catalysis A: General, 2009. **357**(2): p. 206-212.

140. Farhadian, M., P. Sangpout, and G. Hosseinzadeh, *Morphology dependent photocatalytic activity of WO_3 nanostructures.* Journal of Energy Chemistry, 2015. **24**(2): p. 171-177.

141. Lu, Y.-H., et al., *A facile green antisolvent approach to Cu^{2+}-doped ZnO nanocrystals with visible-light-responsive photoactivities.* Nanoscale, 2014. **6**(15): p. 8796-8803.

142. Daniel, M., et al., *Infrared and Raman study of WO_3 tungsten trioxides and WO_3, xH_2O tungsten trioxide tydrates.* Journal of solid state chemistry, 1987. **67**(2): p. 235-247.

143. Santato, C., et al., *Crystallographically oriented mesoporous WO_3 films: synthesis, characterization, and applications.* Journal of the American Chemical Society, 2001. **123**(43): p. 10639-10649.

144. Upadhyay, S., R. Mishra, and P. Sahay, *Enhanced acetone response in co-precipitated WO_3 nanostructures upon indium doping.* Sensors and Actuators B: Chemical, 2015. **209**: p. 368-376.

145. Mukherjee, R., C. Prajapati, and P. Sahay, *Tin-incorporation induced changes in the microstructural, optical, and electrical behavior of tungsten oxide nanocrystalline thin films grown via spray pyrolysis.* Journal of thermal spray technology, 2014. **23**(8): p. 1445-1455.

146. Song, H., et al., *Synthesis of Fe-doped WO_3 nanostructures with high visible-light-driven photocatalytic activities.* Applied Catalysis B: Environmental, 2015. **166**: p. 112-120.

147. Mohite, S., V. Ganbavle, and K. Rajpure, *Solar photoelectrocatalytic activities of rhodamine-B using sprayed WO_3 photoelectrode.* Journal of Alloys and Compounds, 2016. **655**: p. 106-113.

148. Manifacier, J., et al., *Optical and electrical properties of SnO_2 thin films in relation to their stoichiometric deviation and their crystalline structure.* Thin Solid Films, 1977. **41**(2): p. 127-135.

149. Prajapati, C., A. Kushwaha, and P. Sahay, *Influence of Fe doping on the structural, optical and acetone sensing properties of sprayed ZnO thin films.* Materials Research Bulletin, 2013. **48**(7): p. 2687-2695.

150. Bai, S., et al., *Carboxyl-directed hydrothermal synthesis of WO_3 nanostructures and their morphology-dependent gas-sensing properties.* CrystEngComm, 2014. **16**(44): p. 10210-10217.

151. Zheng, F., M. Guo, and M. Zhang, *Hydrothermal preparation and optical properties of orientation-controlled WO_3 nanorod arrays on ITO substrates.* CrystEngComm, 2013. **15**(2): p. 277-284.

152. Mumtaz, M., N.A. Khan, and S. Khan, *Frequency dependent dielectric properties of Cu0. 5Tl0. 5Ba2Ca2 (Cu3-yMy) O10-δ superconductor.* Journal of Applied Physics, 2012. **111**(1): p. 013920.

153. Prodromakis, T. and C. Papavassiliou, *Engineering the Maxwell–Wagner polarization effect.* Applied Surface Science, 2009. **255**(15): p. 6989-6994.

154. Gul, I., et al., *Structural, magnetic and electrical properties of Co 1− xZnxFe₂O₄ synthesized by co-precipitation method.* Journal of magnetism and magnetic materials, 2007. **311**(2): p. 494-499.

155. Mohamed, G.A., A.A. El-Moiz, and M. Rashad, *Li-doping effects on the electrical properties of ZnO films prepared by the chemical-bath deposition method.* Physica B: Condensed Matter, 2005. **370**(1): p. 158-167.

156. Koops, C., *On the dispersion of resistivity and dielectric constant of some semiconductors at audiofrequencies.* Physical Review, 1951. **83**(1): p. 121.

157. Zamiri, R., et al., *Er doped ZnO nanoplates: Synthesis, optical and dielectric properties.* Ceramics International, 2014. **40**(1): p. 1635-1639.

158. Dinesha, M., et al., *Structural and dielectric properties of Fe doped ZnO nanoparticles.* Indian Journal of Physics, 2013. **87**(2): p. 147-153.

159. Shinde, S., et al., *Zinc oxide mediated heterogeneous photocatalytic degradation of organic species under solar radiation.* Journal of Photochemistry and Photobiology B: Biology, 2011. **104**(3): p. 425-433.

160. Yousaf, M., et al., *Visible-light-induced Fe-doped ZnO magnetic photocatalyst nanoparticles for degradation of methylene blue.* Digest Journal of Nanomaterials & Biostructures (DJNB), 2017. **12**(1).

161. Yan, N., et al., *Preparation and properties of Ce-doped TiO_2 photocatalyst.* Materials Research Bulletin, 2012. **47**(8): p. 1869-1873.

162. Arshad, A., et al., *Graphene/SiO_2 nanocomposites: The enhancement of photocatalytic and biomedical activity of SiO_2 nanoparticles by graphene.* Journal of Applied Physics, 2017. **121**(24): p. 244901.

163. Arshad, A., et al., *Solar light triggered catalytic performance of graphene-CuO nanocomposite for waste water treatment.* Ceramics International, 2017.

164. Fakhri, A. and S. Behrouz, *Photocatalytic properties of tungsten trioxide (WO_3) nanoparticles for degradation of Lidocaine under visible and sunlight irradiation.* Solar Energy, 2015. **112**: p. 163-168.

165. AshaRani, P., et al., *Cytotoxicity and genotoxicity of silver nanoparticles in human cells.* ACS nano, 2008. **3**(2): p. 279-290.

166. Sun, S., et al., *Preparation of ordered mesoporous Ag/WO_3 and its highly efficient degradation of acetaldehyde under visible-light irradiation.* Journal of hazardous materials, 2010. **178**(1): p. 427-433.

167. Abe, R., et al., *Pristine simple oxides as visible light driven photocatalysts: highly efficient decomposition of organic compounds over platinum-loaded tungsten oxide.* Journal of the American Chemical Society, 2008. **130**(25): p. 7780-7781.

168. Zhao, Z.G. and M. Miyauchi, *Nanoporous-walled tungsten oxide nanotubes as highly active visible-light-driven photocatalysts.* Angewandte Chemie, 2008. **120**(37): p. 7159-7163.

169. Yan, J., et al., *Tungsten oxide single crystal nanosheets for enhanced multichannel solar light harvesting.* Advanced Materials, 2015. **27**(9): p. 1580-1586.

170. Arfaoui, A., et al., *Investigation into the optoelectrical properties of tungsten oxide thin films annealed in an oxygen air.* Materials Research Bulletin, 2014. **60**: p. 719-729.

171. Lam, S.-M., et al., *Sunlight responsive WO_3/ZnO nanorods for photocatalytic degradation and mineralization of chlorinated phenoxyacetic acid herbicides in water.* Journal of colloid and interface science, 2015. **450**: p. 34-44.

172. Ghasempour, F., et al., *Visible light photoinactivation of bacteria by tungsten oxide nanostructures formed on a tungsten foil.* Applied Surface Science, 2015. **338**: p. 55-60.

173. Liew, S., et al., *Yb-doped WO_3 photocatalysts for water oxidation with visible light.* International Journal of Hydrogen Energy, 2014. **39**(9): p. 4291-4298.

174. Lee, W.J., et al., *Ag grid induced photocurrent enhancement in WO_3 photoanodes and their scale-up performance toward photoelectrochemical H_2 generation.* international journal of hydrogen energy, 2011. **36**(9): p. 5262-5270.

175. Memar, A., et al., *Study on photocurrent of bilayers photoanodes using different combination of WO_3 and Fe_2O_3.* Solar Energy, 2010. **84**(8): p. 1538-1544.

176. Amano, F., et al., *Correlation between surface area and photocatalytic activity for acetaldehyde decomposition over bismuth tungstate particles with a hierarchical structure.* Langmuir, 2010. **26**(10): p. 7174-7180.

177. Xiao, Q. and L. Gao, *One-step hydrothermal synthesis of C, W-codoped mesoporous TiO_2 with enhanced visible light photocatalytic activity.* Journal of Alloys and Compounds, 2013. **551**: p. 286-292.

178. Xu, M., et al., *Controlled Sn-doping in TiO_2 nanowire photoanodes with enhanced photoelectrochemical conversion.* Nano letters, 2012. **12**(3): p. 1503-1508.

179. Bera, A., T. Ghosh, and D. Basak, *Enhanced photoluminescence and photoconductivity of ZnO nanowires with sputtered Zn.* ACS applied materials & interfaces, 2010. **2**(10): p. 2898-2903.

180. Mahanti, M., T. Ghosh, and D. Basak, *Enhanced near band edge luminescence of Ti/ZnO nanorod heterostructures due to the surface diffusion of Ti.* Nanoscale, 2011. **3**(10): p. 4427-4433.

181. Mohebbi, S., S. Molaei, and A.A.R. JUDY, *Preparation and study of Sn-doped CuO nanoparticles as semiconductor.* 2013.

182. Keskenler, E.F., et al., *W doped SnO_2 growth via sol–gel routes and characterization: Nanocubes.* Optik-International Journal for Light and Electron Optics, 2013. **124**(21): p. 4827-4831.

183. Upadhyay, S., R. Mishra, and P. Sahay, *Structural and alcohol response characteristics of Sn-doped WO_3 nanosheets.* Sensors and Actuators B: Chemical, 2014. **193**: p. 19-27.

184. Ahmad, M.Z., et al., *Optical characterisation of nanostructured Au/WO_3 thin films for sensing hydrogen at low concentrations.* Sensors and Actuators B: Chemical, 2013. **179**: p. 125-130.

185. Pang, C., et al., *Inhibition of tungsten particle growth during reduction of V-doped WO_3 nanoparticles prepared by co-precipitation method.* International Journal of Refractory Metals and Hard Materials, 2010. **28**(3): p. 343-348.

186. Srinivas, A., et al., *Acute inhalation toxicity of cerium oxide nanoparticles in rats.* Toxicology letters, 2011. **205**(2): p. 105-115.

187. Nazıroğlu, M., et al., *Acetaminophen at different doses protects brain microsomal Ca^{2+}-ATPase and the antioxidant redox system in rats.* Journal of Membrane Biology, 2009. **231**(2-3): p. 57-64.

188. Chen, S., et al., *Molybdenum sulfide clusters-nitrogen-doped graphene hybrid hydrogel film as an efficient three-dimensional hydrogen evolution electrocatalyst.* Nano Energy, 2015. **11**: p. 11-18.

189. Wang, X., et al., *Building sponge-like robust architectures of CNT–graphene–Si composites with enhanced rate and cycling performance for lithium-ion batteries.* Journal of Materials Chemistry A, 2015. **3**(7): p. 3962-3967.

190. Low, J., et al., *Two-dimensional layered composite photocatalysts.* Chemical Communications, 2014. **50**(74): p. 10768-10777.

191. Xie, Y.P., et al., *Crystal facet-dependent photocatalytic oxidation and reduction reactivity of monoclinic WO_3 for solar energy conversion.* Journal of Materials Chemistry, 2012. **22**(14): p. 6746-6751.

192. Kalantar-zadeh, K., et al., *Synthesis of atomically thin WO_3 sheets from hydrated tungsten trioxide.* Chemistry of Materials, 2010. **22**(19): p. 5660-5666.

193. Sadek, A.Z., et al., *High-temperature anodized WO_3 nanoplatelet films for photosensitive devices.* Langmuir, 2009. **25**(16): p. 9545-9551.

194. Fang, X., et al., *One-step, solventless, and scalable mechanosynthesis of $WO_3 \cdot 2H_2O$ ultrathin narrow nanosheets with superior UV–Vis-light-driven photocatalytic activity.* ACS Sustainable Chemistry & Engineering, 2017. **5**(11): p. 10735-10743.

195. Can, F., et al., *Composition-dependent performance of Ce x Zr_{1-x} O_2 mixed-oxide-supported WO_3 catalysts for the NO_x storage reduction – selective catalytic reduction coupled process.* ACS Catalysis, 2013. **3**(6): p. 1120-1132.

196. Su, J., et al., *Nanostructured $WO_3/BiVO_4$ heterojunction films for efficient photoelectrochemical water splitting.* Nano letters, 2011. **11**(5): p. 1928-1933.

197. Zeng, J., et al., *NO_2 -sensing properties of porous WO_3 gas sensor based on anodized sputtered tungsten thin film.* Sensors and Actuators B: Chemical, 2012. **161**(1): p. 447-452.

198. Liang, L., et al., *High-performance flexible electrochromic device based on facile semiconductor-to-metal transition realized by $WO_3 \cdot 2H_2O$ ultrathin nanosheets.* Scientific reports, 2013. **3**.

199. Sakamoto, J.H., et al., *Enabling individualized therapy through nanotechnology.* Pharmacological Research, 2010. **62**(2): p. 57-89.

200. Phanichphant, S., A. Nakaruk, and D. Channei, *Photocatalytic activity of the binary composite CeO_2/SiO_2 for degradation of dye.* Applied Surface Science, 2016. **387**: p. 214-220.

201. Seigneuric, R., et al., *From nanotechnology to nanomedicine: applications to cancer research.* Current Molecular Medicine, 2010. **10**(7): p. 640-652.

202. Liu, Z., F. Kiessling, and J. Gätjens, *Advanced nanomaterials in multimodal imaging: design, functionalization, and biomedical applications.* Journal of Nanomaterials, 2010. **2010**: p. 51.

203. Kim, J.-E., J.-Y. Shin, and M.-H. Cho, *Magnetic nanoparticles: an update of application for drug delivery and possible toxic effects.* Archives of toxicology, 2012. **86**(5): p. 685-700.

204. Häfeli, U.O., et al., *Cell uptake and in vitro toxicity of magnetic nanoparticles suitable for drug delivery.* Molecular pharmaceutics, 2009. **6**(5): p. 1417-1428.

205. Zhou, H., et al., *Preparation of flower-like Cu-WO_3 nanostructures and their acetone gas sensing performance.* Journal of Chemistry, 2015. **2015**.

206. Li, X., et al., *Strontium adsorption on tantalum-doped hexagonal tungsten oxide.* Journal of hazardous materials, 2014. **264**: p. 386-394.

207. Chang, X., et al., *Synthesis of transition metal-doped tungsten oxide nanostructures and their optical properties.* Materials Letters, 2011. **65**(11): p. 1710-1712.

208. Kumari, M., et al., *Toxicity study of cerium oxide nanoparticles in human neuroblastoma cells.* International journal of toxicology, 2014. **33**(2): p. 86-97.

209. Leung, Y.H., et al., *Toxicity of CeO_2 nanoparticles–the effect of nanoparticle properties.* Journal of Photochemistry and Photobiology B: Biology, 2015. **145**: p. 48-59.

210. Boonstra, J. and J.A. Post, *Molecular events associated with reactive oxygen species and cell cycle progression in mammalian cells.* Gene, 2004. **337**: p. 1-13.

211. Wu, W.-S., *The signaling mechanism of ROS in tumor progression.* Cancer and Metastasis Reviews, 2006. **25**(4): p. 695-705.

212. Hsiao, C.-Y., C.-L. Lee, and D.F. Ollis, *Heterogeneous photocatalysis: degradation of dilute solutions of dichloromethane (CH_2Cl_2), chloroform ($CHCl_3$), and carbon*

tetrachloride (CCl_4) with illuminated TiO_2 photocatalyst. Journal of Catalysis, 1983. **82**(2): p. 418-423.

213. Forgacs, E., T. Cserhati, and G. Oros, *Removal of synthetic dyes from wastewaters: a review*. Environment international, 2004. **30**(7): p. 953-971.

214. Borges, M., et al., *Photocatalysis with solar energy: sunlight-responsive photocatalyst based on TiO_2 loaded on a natural material for wastewater treatment.* Solar Energy, 2016. **135**: p. 527-535.

215. Solarska, R., et al., *Tailoring the morphology of WO_3 films with substitutional cation doping: Effect on the photoelectrochemical properties.* Electrochimica Acta, 2010. **55**(26): p. 7780-7787.

216. Sun, S., X. Chang, and Z. Li, *Growth study and photocatalytic properties of Co-doped tungsten oxide mesocrystals.* Materials Characterization, 2012. **73**: p. 130-136.

217. Arul, N.S., et al., *Enhanced photocatalytic activity of cobalt-doped CeO_2 nanorods.* Journal of sol-gel science and technology, 2012. **64**(3): p. 515-523.

218. Abbas, F., et al., *Differential cytotoxicity of ferromagnetic Co doped CeO_2 nanoparticles against human neuroblastoma cancer cells.* Journal of Alloys and Compounds, 2015. **648**: p. 1060-1066.

219. Santos, L., et al., *Synthesis of WO_3 nanoparticles for biosensing applications.* Sensors and Actuators B: Chemical, 2016. **223**: p. 186-194.

220. Kalantar-zadeh, K., et al., *Two dimensional and layered transition metal oxides.* Applied Materials Today, 2016. **5**: p. 73-89.

221. Shifu, C. and C. Gengyu, *Photocatalytic degradation of organophosphorus pesticides using floating photocatalyst TiO_2· SiO_2/beads by sunlight.* Solar Energy, 2005. **79**(1): p. 1-9.

222. Sharon, M., *Photocatalytic killing of pathogenic bacterial cells using nanosize $Fe2O_3$ and carbon nanotubes.* 2007.

223. Zheng, H., et al., *Nanostructured tungsten oxide–properties, synthesis, and applications.* Advanced Functional Materials, 2011. **21**(12): p. 2175-2196.

224. Atkin, P., et al., *2D WS_2/carbon dot hybrids with enhanced photocatalytic activity.* Journal of Materials Chemistry A, 2016. **4**(35): p. 13563-13571.

225. Mittal, A., et al., *Studies on the adsorption kinetics and isotherms for the removal and recovery of Methyl Orange from wastewaters using waste materials.* Journal of Hazardous Materials, 2007. **148**(1): p. 229-240.

226. ALOthman, Z.A., et al., *Membrane filtration of Sudan orange G on a cellulose acetate membrane filter for separation–preconcentration and spectrophotometric determination in water, chili powder, chili sauce and tomato sauce samples.* Food and chemical toxicology, 2012. **50**(8): p. 2709-2713.

227. Trepel, M., *Assessing the cost-effectiveness of the water purification function of wetlands for environmental planning.* Ecological Complexity, 2010. **7**(3): p. 320-326.

228. Krishnakumar, B. and T. Imae, *Chemically modified novel PAMAM-ZnO nanocomposite: Synthesis, characterization and photocatalytic activity.* Applied Catalysis A: General, 2014. **486**: p. 170-175.

229. Krishnakumar, B., et al., *Chemically modified amino porphyrin/TiO_2 for the degradation of acid black 1 under day light illumination.* Spectrochimica Acta Part A: Molecular and Biomolecular Spectroscopy, 2017. **176**: p. 134-141.

230. Senthilraja, A., et al., *Sn loaded Au–ZnO photocatalyst for the degradation of AR 18 dye under UV-A light.* Journal of Industrial and Engineering Chemistry, 2016. **33**: p. 51-58.

231. Subash, B., et al., *Enhanced photocatalytic performance of WO_3 loaded Ag–ZnO for acid black 1 degradation by UV-A light.* Journal of Molecular Catalysis A: Chemical, 2013. **366**: p. 54-63.

232. Fujioka, Y., et al., *Structural properties of pure and nickel-modified nanocrystalline tungsten trioxide.* The Journal of Physical Chemistry C, 2012. **116**(32): p. 17029-17039.

233. Zhou, J., et al., *Electrochromic properties of vertically aligned Ni-doped WO_3 nanostructure films and their application in complementary electrochromic devices.* Journal of Materials Chemistry C, 2016. **4**(8): p. 1613-1622.

234. Abhudhahir, M.H.S. and J. Kandasamy, *Photocatalytic effect of manganese doped WO_3 and the effect of dopants on degradation of methylene blue.* Journal of Materials Science: Materials in Electronics, 2015. **26**(11): p. 8307-8314.

235. Li, J., J. Zhu, and X. Liu, *Synthesis, characterization and enhanced gas sensing performance of WO_3 nanotube bundles.* New Journal of Chemistry, 2013. **37**(12): p. 4241-4249.

236. Dhanalakshmi, J., et al., *Investigation of oxygen vacancies in Ce coupled TiO_2 nanocomposites by Raman and PL spectra.* Advances in Natural Sciences: Nanoscience and Nanotechnology, 2017. **8**(1): p. 015015.

237. Iqbal, J., et al., *Oxygen-vacancy-induced green emission and room-temperature ferromagnetism in Ni-doped ZnO nanorods.* New Journal of Physics, 2009. **11**(6): p. 063009.

238. Ding, B., et al., *Tuning oxygen vacancy photoluminescence in monoclinic Y_2WO_6 by selectively occupying yttrium sites using lanthanum.* Scientific reports, 2015. **5**.

239. Liqiang, J., et al., *Review of photoluminescence performance of nano-sized semiconductor materials and its relationships with photocatalytic activity.* Solar Energy Materials and Solar Cells, 2006. **90**(12): p. 1773-1787.